8-2018

Optimization Methods in Electric Power Systems: Global Solutions for Optimal Power Flow and Algorithms for Resilient Design under Geomagnetic Disturbances

Mowen Lu
Clemson University, mowengator@gmail.com

Optimization Methods in Electric Power Systems: Global Solutions for Optimal Power Flow and Algorithms for Resilient Design under Geomagnetic Disturbances

---

A Dissertation
Presented to
the Graduate School of
Clemson University

In Partial Fulfillment
of the Requirements for the Degree
Doctor of Philosophy
Industrial Engineering

---

by
Mowen Lu
August 2018

Accepted by:
Dr. Sandra D. Eksioglu, Committee Co-Chair
Dr. Scott J. Mason, Committee Co-Chair
Dr. Russell Bent
Dr. Burak Eksioglu

Abstract

An electric power system is a network of various components that generates and delivers power to end users. Since 1881, U.S. electric utilities have supplied power to billions of industrial, commercial, public, and residential customers continuously. Given the rapid growth of power utilities, power system optimization has evolved with developments in computing and optimization theory. In this dissertation, we focus on two optimization problems associated with power system planning: the AC optimal power flow (ACOPF) problem and the optimal transmission line switching (OTS) problem under geomagnetic disturbances (GMDs). The former problem is formulated as a nonlinear, non-convex network optimization problem, while the latter is the network design version of the ACOPF problem that allows topology reconfiguration and considers space weather-induced effects on power systems. Overall, the goal of this research includes: (1) developing computationally efficient approaches for the ACOPF problem in order to improve power dispatch efficiency and (2) identifying an optimal topology configuration to help ISO operate power systems reliably and efficiently under geomagnetic disturbances.

Chapter 1 introduces the problems we are studying and motivates the proposed research. We present the ACOPF problem and the state-of-the-art solution methods developed in recent years. Next, we introduce geomagnetic disturbances and describe how they can impact electrical power systems. In Chapter 2, we revisit the polar power-voltage formulation of the ACOPF problem and focus on convex relaxation methods to develop lower bounds on the problem objective. Based on these approaches, we propose an adaptive, multivariate partitioning algorithm with bound tightening and heuristic branching strate-

gies that progressively improves these relaxations and, given sufficient time, converges to the globally optimal solution. Computational results show that our methodology provides a computationally tractable approach to obtain tight relaxation bounds for hard ACOPF cases from the literature. In Chapter 3, we focus on the impact that extreme GMD events could potentially have on the ability of a power system to deliver power reliably. We develop a mixed-integer, nonlinear model which captures and mitigates GMD effects through line switching, generator dispatch, and load shedding. In addition, we present a heuristic algorithm that provides high-quality solutions quickly. Our work demonstrates that line switching is an effective way to mitigate GIC impacts. In Chapter 4, we extend the preliminary study presented in Chapter 3 and further consider the uncertain nature of GMD events. We propose a two-stage distributionally robust (DR) optimization model that captures geoelectric fields induced by uncertain GMDs. Additionally, we present a reformulation of a two-stage DRO that creates a decomposition framework for solving our problem. Computational results show that our DRO approach provides solutions that are robust to errors in GMD event predictions. Finally, in Chapter 5, we summarize the research contributions of our work and provide directions for future research.

Acknowledgments

This dissertation is not only a summary of my work throughout my Ph.D. program, but also a milestone for my whole journey in operations research. Since the first day I joined Clemson University, I have been given unique opportunities and benefited from them. I would like to extend thanks to the people throughout the journey, who so generously helped me and contributed to this dissertation.

First and foremost, I would like to thank my advisors Dr. Sandra D Eksioglu and Dr. Scott J Mason who have been mentoring me in every aspect of my life. The last four years have been an amazing experience and I thank them wholeheartedly, not only for the tremendous academic guidance I received, but also for guiding me to become an independent thinker and nourishing me to be a real researcher. They generously provide me assistantships financially, and also give me great academic and emotional supports throughout the years. It has been a great honour to work with them so closely.

Profound gratitude goes to Dr. Russell Bent, who has been mentoring me since the first day I went to Los Alamos National Laboratory. I am thankful for his tremendous help and continuous support being my committee member. It was a great experience in Los Alamos. I am also hugely appreciative to Dr. Burak Eksioglu for being my committee member and providing constructive guidance during my doctoral studies. Special thanks to Harsha Nagarajan, Site Wang, Shasha Wang, Sreenath Chalil Madathil, Zahra Azadi, Scott Backhaus, Emre Yamangil, and Arthur Barnes for providing great help in last four years. Finally, but by no means least, thanks go my dad, mum and my husband for all the support and love, being my source of energy and passion for my life.

Table of Contents

List of Tables

List of Figures

Chapter 1

Introduction

An electric power system is a network of various components that generates and delivers power to end users. It is operated, controlled, and monitored by an independent system operator (ISO), an organization formed by the direction of the Federal Energy Regulatory Commission (FERC). Since 1881, U.S. electric utilities have supplied power to billions of industrial, commercial, public, and residential customers continuously (Fig.1.1). Given the rapid growth in power demand, the cost-effective utilization of power utilities while providing reliable accessibility is extremely important. U.S. Energy Information Administration (EIA) data on wholesale electricity prices suggests that small increases in dispatch efficiency could save billions of dollars per year [24].

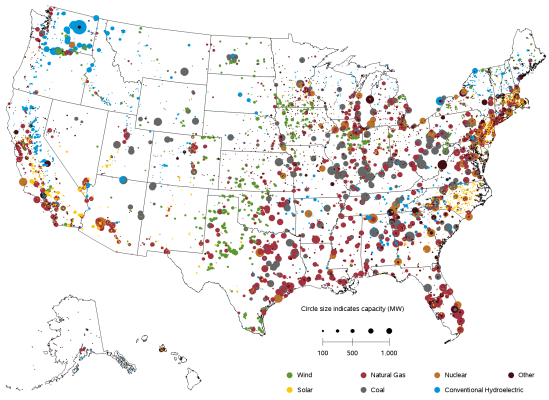

Figure 1.1: Operable utility-scale generating units as of July 2017. (Source: `https://commons.wikimedia.org/wiki/File:Power_plants_map.png`)

1.1 Optimal Power Flow

The alternating current optimal power flow (ACOPF) problem is one of the most fundamental optimization problems for analyzing the economic and reliable operations of electric power systems. It is solved every year, every day, and every 5-15 minutes to help ISOs make decisions for different types of power markets [24]. For example, power system planning can be divided into three categories: long-term planing, medium-term planning and short-term planning [62]. Long-term decisions are usually taken over a period of 5-15 years and involve plans about network expansion for meeting an anticipated future load requirements. Medium-term planning is used for maintenance schedules of the system components; these decisions are typically made annually. Short-term decisions are made daily to deal with operations contingencies and generating unit schedules. In this dissertation, we focus on short-term real-time decisions in power systems for planning generator dispatch and improving system reliability.

The ACOPF was first introduced in 1962 [26] and has been formulated in various forms over the years [104]. In the first half of the 20th century, the optimal power flow (OPF) problem usually was solved intuitively by power engineers and operators using experience, rules of thumb, and analog network analyzers [100]. Gradually, with advances in optimization theory, both Gauss-Seidel and Newton-Raphson methods were commonly used to solve OPF problems. In 1962, Carpentier [26] proposed optimality conditions for the OPF using Karush–Kuhn–Tucker (KKT) conditions in the first publication formulating the full OPF problem. Although the OPF problem has been around for 55 years, the development of efficient solution techniques has remained an active field of research. The main challenges associated with solving the ACOPF include: a) nonconvex and nonlinear models of AC physics, b) large-scale power grids with thousand buses and edges, and c) limited computation time availability in real-time dispatch applications (wherein decisions are made every 5-15 minutes). In recent years, various solution algorithms, ranging from heuristics to convex relaxations, have been studied in the literature. Without loss of gen-

erality, the ACOPF literature can be roughly categorized into three main research thrusts: a) finding locally optimal solutions quickly, b) deriving strong, convex relaxations, and c) proving global optimality.

In the local search literature, local solvers motivated by primal-dual interior point methods or sequential linearization heuristics based on a Taylor-series expansion commonly are used to find feasible solutions efficiently, but without any guarantees on solution quality [23,29]. In the relaxation literature, recent work has focused on deriving convex relaxations that produce tight lower bounds, including semidefinite programming (SDP)-based methods [68], quadratic convex (QC) relaxations [57], and second-order cone (SOC) relaxations [63]. The performance of these methods has been evaluated and tested on well established power system test cases from the literature [30,31]. Though relaxation approaches have empirically yielded good lower bounds on average, a small improvement of solution quality could result in significant savings: according to data reported by EIA [5], billions of dollars of potential cost could be saved with only a 5% improvement in power dispatch efficiency. Finally, recent efforts have focused on obtaining globally optimal solutions through SOC- and SDP-based relaxations [46, 63] using standard spatial branch-&-bound (sBB) approaches. Today, the research challenge is to find globally optimal solutions consistently and quickly, given the computational time allowed for solving the full ACOPF problem in practice [24].

It is essential to develop fast solution methodologies for the ACOPF problem in order to improve power dispatch efficiency, as this could dramatically reduce costs each year. In the first phase of this research, we focus on decreasing the best optimality gaps known to date on hard instances of the ACOPF problem by improving QC relaxations, developing new branching strategies, and leveraging high-quality, locally optimal solutions.

1.2 Resilient Electrical Grid under Geomagnetic Disturbances

An electric power system is designed for delivering large amounts of power from distant sources to demanding consumers [81]. Within these systems, the underlying high-

voltage transmission network plays a vital role in facilitating this bulk movement of electrical power. Transmission systems must be kept highly reliable to prevent blackouts and ensure robust energy markets. However, when extreme events occur in large-scale transmission systems, the ability to deliver power reliably could be significantly impacted due to physical damage to overhead transmission lines and other system components. In this context, this dissertation considers the impact caused by extreme space weather (i.e., geomagnetic disturbances) on transmission systems. We focus on improving the response (resilience) of power systems by switching on and off transmission lines. This optimal transmission switching (OTS) problem [42] is the OPF problem extended to consider network topology reconfiguration options [62].

1.2.1 Impact of Geomagnetic Disturbances on Transmission Systems

Solar flares and coronal mass ejections cause geomagnetic disturbances (GMDs) that lead to changes in the Earth's magnetic field which, in turn, create geo-electric fields (Fig.1.2). These low-frequency, geo-electric fields induce quasi-DC currents, also known as geomagnetically-induced currents (GICs), in grounded sections of power system networks [10, 11, 105]. The GICs are superimposed on the usual alternating currents (AC) and bias the AC such that maximum currents are increased. In many power system components, this bias is not a major concern; however, in transformers, it can lead to half-cycle saturation (i.e., the magnetic cores in the transformers are asymmetrically saturated since the DC magnetic flux is superimposed on the AC flux [67, 95]) and the loss of magnetic flux in regions outside of the transformer core. The energy stored in the stray flux increases the reactive power consumption of the transformer, which can affect system voltages. Stray flux also drives eddy currents that can cause excessive transformer heating, leading to reduced transformer life or, potentially, immediate damage [7] (Fig.1.3).

The ability of a power system to reliably deliver power can be severely impacted by the catastrophic damages caused by GMDs. Of all historical GMD occurrences, one of the

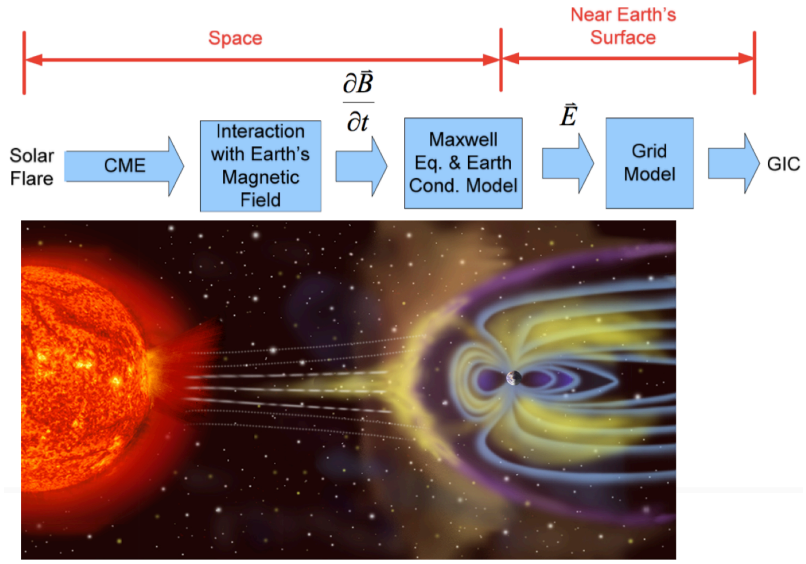

Figure 1.2: Geomagnetic Disturbances. (Source: `https://en.wikipedia.org/wiki/Geomagnetic_storm`)

(a) transformer burning (b) transformer melting

Figure 1.3: Transformer damage due to GMD effects. (Source: `http://www.americanpreppersnetworkradionet.com/2014/09/weathering-solar-storm.html`)

most severe events occurred in March 1989, which resulted in the shutdown of the Hydro-Quebec power system. As a consequence, six million people suffered a nine-hour power outage. The most recent GMDs were observed between October 19 and November 5, 2003, which are often referred to as the Halloween Solar Storms [2]. During this event, satellite-

based systems and communications were affected and power outages occured in Sweden. Although GMD events are rare, the posed threat can result in high costs involving not only the replacement of physically damaged equipment (e.g., high-voltage transformers), but also the loss of revenue from the associated systems whose performance depends on reliable power. For example, the net cost of the Quebec 1989 GMD event was $13.2 million, with damaged equipment accounting for $6.5 million [19]. Hence, it is important to study the GMD-induced impacts on power systems and enhance the performance of transmission networks to deal with such negative effects.

There are two known primary risks associated with GICs in power systems. The first is increased reactive power consumption in transformers and subsequent drops in system voltages [7] and the second is transformer damage caused by hot-spot heating. To model these risks, it is important to quantify GICs in bulk power systems. The North American Electric Reliability Corporation (NERC) presents a procedure for computing GICs in a system given the orientation and magnitude of a geo-electric field [6]. A common assumption for GIC calculation is that the geo-electric field is uniformly distributed along the northward and eastward directions [58]. This assumption is prevalent because if the geo-electric field is non-uniform, the routing twist and turns of transmission lines must be considered, which makes the necessary computations more complicated [6]. Further, solar activities, such as solar flares or coronal mass ejections (CMEs), are unpredictable. Although ground- and space-based sensors and imaging systems have been utilized by the National Aeronautics and Space Administration (NASA) to observe these activities at various depths in the solar atmosphere, accurate information about geomagnetic storms cannot be obtained until the released particles arrive on Earth and interact with the geomagnetic field [85]. In the presence of uncertain GMDs, GIC effects cannot be calculated exactly, which makes the efficient and economical operations of power systems much more difficult.

1.2.2 Optimal Transmission Switching

In recent years, transmission switching has been explored in the literature as a control method to cope with emergency conditions, such as mitigating line overloads [47] and transmission flow violations [12], preserving system security [59], and improving network resilience [81]. Changing system topology by switching on and off transmission lines adds flexibility to network configurations and can bring economic benefits in power markets [86]. Studies indicate that removing transmission lines could potentially improve the dispatch efficiency of power system [42,54]. As a result, generation cost can be significantly reduced. Transmission switching has been applied to transmission system expansion planning problems. In work by Amin and Mohammad [61], transmission switching is modeled as the subproblem to identify the best system configuration for a transmission capacity expansion problem with contingencies. Overall, transmission switching is a real-time control action for maintaining system security while providing potential economical advantages.

Optimal transmission line switching (OTS) with AC power flow is a mathematically challenging problem due to the computational complexity induced by nonlinear, nonconvex AC physics and switching (binary) variables. In the literature, the direct current (DC) power flow approximation has been widely used in nearly all OTS problem studies to date [15, 34, 42, 61, 65, 86, 99, 107]. The DCOPF approximation linearizes the AC physics of the power transmission system by neglecting reactive power consumption and line losses [104]. It assumes zero line resistance, small phase angle differences, and fixed magnitude of bus voltage (i.e., 1 per unit). With these assumptions, the DC optimal transmission switching problem (DCOTS) can be formulated as a mixed-integer, linear program (MILP) and solved by commercial MILP solvers such as CPLEX and Gurobi. Meanwhile, additional research has focused on exploring heuristic methods to efficiently obtain good solutions for large-scale networks [43, 98], as they are intractable for existing solvers. For example, Hedman *et al.* [55] incorporates DCOTS with N-1 security constraints and uses heuristics to iteratively determine switching decisions while preserving N-1 security. However, the optimal topology decision obtained by solving OTS under a DC approximation may not be feasible for the AC

power flow physics. As a result, cost savings might be over estimated and reliability issues might be overlooked [57]. In addition, our research takes into account the additional reactive power consumption induced by GICs, while the reactive power is negligible in the DCOPF approximation. Hence, to avoid feasibility issues and consider reactive power consumption, it is necessary to use AC power flow equations in the OTS formulation.

Studies of the AC optimal transmission line switching problem (ACOTS) are limited in the literature. Existing solution methodologies designed for the ACOTS heavily rely on tight convex relaxations and advanced discrete optimization techniques [42, 87]. Recently, various convex relaxations and disjunctive representations have been developed, such as second-order-conic (SOC) relaxations [64], quadratically constrained (QC) relaxations [56], and semi-definite programming (SDP) relaxations [13]. In the context of transmission expansion planning applications, QC relaxations have been shown to be effective [81, 84]. Despite these recent advances in optimization methods for OTS, global methods still cannot scale to solve systems with 500 nodes.

Chapter 2

Global Optimization Methods for Optimal Power Flow

Since the alternating current optimal power flow (ACOPF) problem was introduced in 1962, developing efficient solution algorithms for the ACOPF problem has been an active field of research. In recent years, there has been increasing interest in convex relaxation-based solution approaches that have proven effective in practice. Based on these approaches, we develop an adaptive, multivariate partitioning algorithm with bound tightening and heuristic branching strategies that progressively improves these relaxations and, given sufficient time, converges to the global optimal solution. We illustrate the strengths of our algorithm using benchmark ACOPF test cases from the literature. Computational results show that our novel algorithm reduces the best known optimality gap for some hard ACOPF test cases.

Nomenclature

Sets

$\mathcal{N}$	set of nodes (buses)
$\mathcal{G}$	set of generators
$\mathcal{G}_i$	set of generators at bus i
$\mathcal{E}$	set of *from* edges (lines)
$\mathcal{E}^R$	set of *to* edges (lines)

Parameters

$\boldsymbol{c}_0, \boldsymbol{c}_1, \boldsymbol{c}_2$	generation cost coefficients
$\boldsymbol{i}$	imaginary number constant
$\boldsymbol{Y}_{ij} = \boldsymbol{g}_{ij} + \boldsymbol{i}\boldsymbol{b}_{ij}$	admittance on line ij
$\boldsymbol{S}_i^{\boldsymbol{d}} = \boldsymbol{p}_i^{\boldsymbol{d}} + \boldsymbol{i}\boldsymbol{q}_i^{\boldsymbol{d}}$	AC power demand at bus i
$\overline{\boldsymbol{S}}_{ij}$	apparent power limit on line ij
$\underline{\boldsymbol{\theta}}_{ij}, \overline{\boldsymbol{\theta}}_{ij}$	phase angle difference limits on line ij
$\boldsymbol{\theta}_{ij}^{\boldsymbol{M}}$	max(| $\underline{\boldsymbol{\theta}}_{ij}$ |, | $\overline{\boldsymbol{\theta}}_{ij}$ |) on line ij
$\underline{\boldsymbol{v}}_i, \overline{\boldsymbol{v}}_i$	voltage magnitude limit at bus i
$\underline{\boldsymbol{S}}_i^{\boldsymbol{g}}$, $\overline{\boldsymbol{S}}_i^{\boldsymbol{g}}$	power generation limit at bus i

$\mathfrak{R}(\cdot)$	real part of a complex number
$\mathfrak{T}(\cdot)$	imaginary part of a complex number
$(\cdot)^*$	hermitian conjugate of a complex number
$\lvert\cdot\rvert, \angle\cdot$	magnitude, angle of a complex number

Continuous Variables

$V_i = v_i e^{i\theta_i}$	AC voltage at bus i
$\theta_{ij} = \angle V_i - \angle V_j$	phase angle difference on line ij
W_{ij}	AC voltage product on line ij, i.e., $V_i V_j^*$
$S_{ij} = p_{ij} + \boldsymbol{i} q_{ij}$	AC power flow on line ij
$S_i^g = p_i^g + \boldsymbol{i} q_i^g$	AC power generation at bus i
l_{ij}	current magnitude squared on line ij

2.1 Introduction

The optimal power flow problem is one of the most fundamental optimization problems for identifying the economic and reliable operations of electric power systems. The ACOPF formulation is a cost minimization problem with equality and inequality constraints setting bus voltage, line flows and generator dispatch. It was first introduced in 1962 and has been formulated in various forms over years, e.g., the polar power-voltage formulation and the rectangular power-voltage formulation [24]. Since the introduction of the ACOPF problem [26], the development of efficient solution techniques for the ACOPF has remained an active field of research. The main challenges associated with solving the ACOPF include: a) non-convex and nonlinear mathematical models of AC physics, b) large-scale power grids, and c) limited computation time available in real-time dispatch applications. A computationally efficient algorithm for obtaining high-quality and lower-cost dispatch

solutions could improve the operational performance of power systems and save billions of dollars per year [24].

Various solution algorithms, ranging from heuristic to convex relaxation, have been studied within the literature [57, 77]. Without losing generality, the ACOPF literature can be roughly categorized into three main research directions: a) finding locally optimal solutions quickly, b) deriving strong, convex relaxations, and c) proving global optimality. In the local search literature, local solvers based on primal-dual interior point methods or sequential linearization heuristics are used to find feasible solutions efficiently without any guarantees on solution quality. In the relaxation literature, recent work has focused on deriving convex relaxations that produce tight lower bounds. These relaxation techniques include semi-definite programming (SDP) relaxations [68], quadratic relaxations (QC) [57] and second-order-cone (SOC) relaxations [63]. The performances of these existing methods have been evaluated and tested on well established power system test cases (i.e., Matpower and NESTA Test Cases) [31]. Though the relaxation approaches have empirically yielded strong lower bounds, there remain examples where the lower bounds are weak (e.g., case5, nesta_case30_fsr_api, nesta_case118_ieee_api, etc.) [57]. Finally, there have been recent efforts focused on obtaining globally optimal solutions through SOC and SDP-based relaxations [46, 63] using standard spatial branch-&-bound (sBB) approaches. In this chapter, we focus on decreasing the optimality gaps on remaining hard instances by improving the QC relaxations, developing new branching strategies, and leveraging high quality locally optimal solutions.

The focus of this chapter is a novel approach for globally optimizing the ACOPF problem. Our study is built on an adaptive multivariate partitioning algorithm (AMP) proposed in [82, 83]. The approach is based on a two-stage algorithm that uses sBB-like methods tailored to OPF problems. In the first stage, we apply sequential bound-tightening techniques to the voltage and phase-angle variables and obtain tightest possible bounds by solving a sequence of convex problems [27, 32]. The second stage adaptively partitions convex envelopes of the ACOPF into piecewise convex regions around best-known local

feasible solutions. This approach exploits the observation that local solutions to standard benchmark instances are already very good. Our recent results on generic mixed-integer nonlinear programs suggest that refining variable domains adaptively around best-known feasible solutions can dramatically speed up the convergence to global optimum [82, 114].

This research makes three key contributions to solving the ACOPF problem. The first contribution develops an efficient partitioning scheme for tightening relaxations. In multilinear relaxations, many approaches build uniform, piecewise relaxations via univariate or bivariate partitioning [53]. One drawback of such approaches is that a large number of partitions may be needed to attain global optimum. Thus, these approaches are often restricted to small problems. To address inefficiencies of these approaches, we develop an adaptive tightening algorithm with non-uniform partitions, where we selectively partition convex envelopes that heuristically appear to tighten the relaxations.

Our second contribution lies in applying well-known ideas for deriving the tightest possible convex relaxations (convex-hulls) for multilinear functions as they play a crucial role for developing efficient global optimization approaches. Multilinears (up to trilinear) appear in the polar form of the ACOPF, for which there has been a recent development in developing strong convex quadratic relaxations (QC) [33, 57]. However, these relaxations employ recursive McCormick envelopes to handle the trilinear terms, which rarely capture their convex hulls. In the optimization literature, specifically for a trilinear function, Meyer and Floudas [78] (Meyer-Floudas envelopes) describe the convex hull by deriving all it's facets, and for a generic multilinear function, convex hull is typically formulated as a convex combination of the extreme points of the function [97]. Owing to the simplicity of the latter idea from the global optimization perspective, we further strengthen the QC relaxations to obtain tighter lower bounds for the OPF problem. Also, we develop tight piecewise convex relaxations of the convex-hull representation for trilinear and quadratic functions by extending the ideas of approximating univariate/bivariate functions [90, 106].

The third contribution of this research is a novel algorithm that combines iterative partitioning (using piecewise relaxations) with bound tightening to globally solve the

ACOPF (given sufficient time). This algorithm first applies "optimality-based bound tightening" by solving a sequence of min. and max. problems on voltage and phase angle difference variables [27, 32, 92]. Second, the algorithm iteratively partitions the convex envelopes to tighten the lower bound. Simultaneously, the algorithm updates locally feasible solutions to tighten the upper bound. The combination of tightening the upper and lower bound yields an algorithm akin to sBB that determines the globally optimal solution.

2.2 AC Optimal Power Flow Problem

In this chapter, constants are typeset in bold face. In the AC power flow equations, the primitives, V_i, S_{ij}, S_i^g, $\boldsymbol{S_i^d}$ and $\boldsymbol{Y}_{ij}$ are complex quantities. Given any two complex numbers (variables/constants) z_1 and z_2, $z_1 \geqslant z_2$ implies $\mathfrak{R}(z_1) \geqslant \mathfrak{R}(z_2)$ and $\mathfrak{T}(z_1) \geqslant \mathfrak{T}(z_2)$. $|\cdot|$ represents absolute value when applied on a real number. Statement $A \wedge B$ is true *iff* A and B are both true; else it is false. $\langle f(\cdot) \rangle^R$ represents the constraints corresponding to the convex relaxation of function $f(\cdot)$.

This section describes the mathematical formulation of the ACOPF problem using the *polar* formulation. A power network is represented as a graph, $(\mathcal{N}, \mathcal{E})$, where $\mathcal{N}$ and $\mathcal{E}$ are the buses and transmission lines, respectively. Generators are connected to buses where $\mathcal{G}_i$ are the generators at bus i. We assume that there is power demand (load) at every bus, some of which is zero. The optimal solution to the ACOPF problem minimizes generation costs for a specified demand and satisfies engineering constraints and power flow physics. More formally, the ACOPF problem is mathematically stated as:

$$\boldsymbol{\mathcal{P}} := \min \sum_{i \in \mathcal{G}} \boldsymbol{c}_{2i}(\mathfrak{R}(S_i^g)^2) + \boldsymbol{c}_{1i}\mathfrak{R}(S_i^g) + \boldsymbol{c}_{0i} \tag{2.1a}$$

$$s.t. \quad \sum_{k \in \mathcal{G}_i} S_k^g - \boldsymbol{S_i^d} = \sum_{(i,j) \in \mathcal{E} \cup \mathcal{E}^{\mathcal{R}}} S_{ij} \qquad \forall i \in \mathcal{N} \tag{2.1b}$$

$$S_{ij} = \boldsymbol{Y}_{ij}^* W_{ii} - \boldsymbol{Y}_{ij}^* W_{ij} \quad \forall (i,j) \in \mathcal{E} \tag{2.1c}$$

$$S_{ji} = \boldsymbol{Y}_{ij}^* W_{jj} - \boldsymbol{Y}_{ij}^* W_{ij}^* \quad \forall (i,j) \in \mathcal{E} \tag{2.1d}$$

$$W_{ii} = |V_i|^2 \quad \forall i \in \mathcal{N} \tag{2.1e}$$

$$W_{ij} = V_i V_j^* \quad \forall (i,j) \in \mathcal{E} \tag{2.1f}$$

$$\underline{\boldsymbol{\theta}}_{ij} \leqslant \angle V_i - \angle V_j \leqslant \overline{\boldsymbol{\theta}}_{ij} \quad \forall (i,j) \in \mathcal{E} \tag{2.1g}$$

$$\underline{\boldsymbol{v}}_i \leqslant |V_i| \leqslant \overline{\boldsymbol{v}}_i \quad \forall i \in \mathcal{N} \tag{2.1h}$$

$$\underline{\boldsymbol{S}}_i^{\boldsymbol{g}} \leqslant S_i^g \leqslant \overline{\boldsymbol{S}}_i^{\boldsymbol{g}} \quad \forall i \in \mathcal{G} \tag{2.1i}$$

$$|S_{ij}| \leqslant \overline{\boldsymbol{S}}_{ij} \quad \forall (i,j) \in \mathcal{E} \cup \mathcal{E}^{\mathcal{R}} \tag{2.1j}$$

In formulation (2.1), the convex quadratic objective (2.1a) minimizes total generator dispatch cost. Constraint (2.1b) corresponds to the nodal power balance at each bus, e.g. Kirchoff's current law. Constraints (2.1c) through (2.1f) model the AC power flow on each line in complex number notation. Constraint (2.1g) limits the phase angle difference on each line. Constraint (2.1h) limits the voltage magnitude at each bus. Constraint (2.1i) restricts the apparent power output of each generator. Finally, constraint (2.1j) restricts the total electric power transmitted on each line. For simplicity, we omit the details of constant bus shunt injections, transformer taps, phase shifts, and line charging, though we include them in the computational studies. The ACOPF is a hard, non-convex problem [18] where the source of *non-convexity* is in constraints (2.1e) and (2.1f), which reduce to:

$$W_{ii} = v_i^2 \tag{2.2a}$$

$$\mathfrak{R}(W_{ij}) = v_i v_j \cos(\theta_{ij}) \tag{2.2b}$$

$$\mathfrak{T}(W_{ij}) = v_i v_j \sin(\theta_{ij}) \tag{2.2c}$$

To address the non-convexities, we first summarize a state-of-the-art convex relaxation with some enhancements and then derive tighter piecewise relaxations.

2.3 Convex Quadratic Relaxation of the ACOPF

In this section, we discuss the features of the convex quadratic (QC) relaxation of the ACOPF [32, 57]. Though there are numerous other relaxations in the literature, we adopt the QC relaxations as it has been observed to be empirically tight, computationally stable, and efficient. We further tighten the sinusoidal relaxations of [32, 57] for certain conditions and introduce the tightest possible convex relaxations for trilinear functions.

Quadratic function relaxation Given a voltage variable, $v_i \in [\underline{\mathbf{v}}_i, \overline{\mathbf{v}}_i]$, the tightest convex envelop is formulated with a lifted variable, $\widehat{w}_i \in \langle v_i^2 \rangle^R$, where

$$\widehat{w}_i \geqslant v_i^2 \tag{2.3a}$$

$$\widehat{w}_i \leqslant (\underline{\boldsymbol{v}}_i + \overline{\boldsymbol{v}}_i)v_i - \underline{\boldsymbol{v}}_i\overline{\boldsymbol{v}}_i \tag{2.3b}$$

Cosine function relaxation Under the assumptions that $|\underline{\boldsymbol{\theta}}_{ij}|$ is not always equal to $|\overline{\boldsymbol{\theta}}_{ij}|$ and $\boldsymbol{\theta}_{ij}^{\boldsymbol{M}} \leqslant \pi/2$, the convex quadratic envelope of the cosine function is formulated with a lifted variable $\widehat{cs}_{ij} \in \langle \cos(\theta_{ij}) \rangle^R$ where

$$\widehat{cs}_{ij} \leqslant 1 - \frac{1 - \cos(\boldsymbol{\theta}_{ij}^{\boldsymbol{M}})}{(\boldsymbol{\theta}_{ij}^{\boldsymbol{M}})^2}(\theta_{ij}^2) \tag{2.4a}$$

$$\widehat{cs}_{ij} \geqslant \frac{\cos(\overline{\boldsymbol{\theta}}_{ij}) - \cos(\underline{\boldsymbol{\theta}}_{ij})}{\overline{\boldsymbol{\theta}}_{ij} - \underline{\boldsymbol{\theta}}_{ij}}(\theta_{ij} - \overline{\boldsymbol{\theta}}_{ij}) + \cos(\underline{\boldsymbol{\theta}}_{ij}) \tag{2.4b}$$

Sine function relaxation First, let the first-order Taylor's approximation of $\sin(\theta)$ at $\overline{\boldsymbol{\theta}}$ be

$$f^{oa}(\overline{\boldsymbol{\theta}}) = \sin(\overline{\boldsymbol{\theta}}) + \cos(\overline{\boldsymbol{\theta}})(\theta - \overline{\boldsymbol{\theta}}) \tag{2.5}$$

Second, let the secant function between $(\overline{\boldsymbol{\theta}}, \sin(\overline{\boldsymbol{\theta}}))$ and $(\underline{\boldsymbol{\theta}}, \sin(\underline{\boldsymbol{\theta}}))$ be

$$f^{sec}(\underline{\boldsymbol{\theta}}, \overline{\boldsymbol{\theta}}) = \frac{\sin(\overline{\boldsymbol{\theta}}) - \sin(\underline{\boldsymbol{\theta}})}{\overline{\boldsymbol{\theta}} - \underline{\boldsymbol{\theta}}}(\theta - \underline{\boldsymbol{\theta}}) + \sin(\underline{\boldsymbol{\theta}}) \tag{2.6}$$

Finally, given bounds $[\underline{\boldsymbol{\theta}}, \overline{\boldsymbol{\theta}}]$, we use $\boldsymbol{\theta}^{\boldsymbol{\mu}} = \frac{(\underline{\boldsymbol{\theta}} + \overline{\boldsymbol{\theta}})}{2}$ to denote the midpoint of the bounds. Since

the bounds on phase-angle differences can be non-symmetric, we derive convex relaxations of the sine function for three cases:

Case (a): When $(\underline{\boldsymbol{\theta}}_{ij} < 0) \wedge (\overline{\boldsymbol{\theta}}_{ij} > 0)$, the polyhedral relaxation, as described in [57], is characterized with lifted variable $\widehat{sn}_{ij} \in \langle \sin(\theta_{ij}) \rangle^R$ where

$$\widehat{sn}_{ij} \leqslant f^{oa}(\boldsymbol{\theta}^{\boldsymbol{M}}_{ij}/2), \quad \widehat{sn}_{ij} \geqslant f^{oa}(-\boldsymbol{\theta}^{\boldsymbol{M}}_{ij}/2) \tag{2.7}$$

Case (b): When $(\underline{\boldsymbol{\theta}}_{ij} < 0) \wedge (\overline{\boldsymbol{\theta}}_{ij} < 0)$, we derive a tighter polyhedral relaxations that exploits a lack of an inflection point in the sine function. This relaxation is defined by:

$$\widehat{sn}_{ij} \leqslant f^{sec}(\underline{\boldsymbol{\theta}}_{ij}, \overline{\boldsymbol{\theta}}_{ij}), \tag{2.8a}$$

$$\widehat{sn}_{ij} \geqslant f^{oa}(\boldsymbol{\theta}_{ij}) \quad \forall \boldsymbol{\theta}_{ij} \in \{\underline{\boldsymbol{\theta}}_{ij}, \boldsymbol{\theta}^{\boldsymbol{\mu}}_{ij}, \overline{\boldsymbol{\theta}}_{ij}\}. \tag{2.8b}$$

Case (c): Like case (b), when $(\underline{\boldsymbol{\theta}}_{ij} > 0) \wedge (\overline{\boldsymbol{\theta}}_{ij} > 0)$, a tighter polyhedral relaxation for the sine function is:

$$\widehat{sn}_{ij} \geqslant f^{sec}(\underline{\boldsymbol{\theta}}_{ij}, \overline{\boldsymbol{\theta}}_{ij}), \tag{2.9a}$$

$$\widehat{sn}_{ij} \leqslant f^{oa}(\boldsymbol{\theta}_{ij}) \quad \forall \boldsymbol{\theta}_{ij} \in \{\underline{\boldsymbol{\theta}}_{ij}, \boldsymbol{\theta}^{\boldsymbol{\mu}}_{ij}, \overline{\boldsymbol{\theta}}_{ij}\}. \tag{2.9b}$$

A geometric visualization of the relaxations of the sine function for cases (a) and (c) are shown in Figure 2.1.

Trilinear function relaxation After introducing the lifted variables, $\widehat{cs}_{ij}$ and $\widehat{sn}_{ij}$ from above, the non-convex constraints in (2.2b) and (2.2c) become trilinear functions of the form $v_i v_j \widehat{cs}_{ij}$ and $v_i v_j \widehat{sn}_{ij}$. In the literature, bilinear McCormick relaxations are applied recursively to relax these trilinear functions [57, 77], which rarely capture their convex hull. Instead, we relax the trilinear function based on the convex hull of the extreme points using techniques from [97].

Given a trilinear function $\phi(x_1, x_2, x_3) = x_1 x_2 x_3$ with respective variable bounds

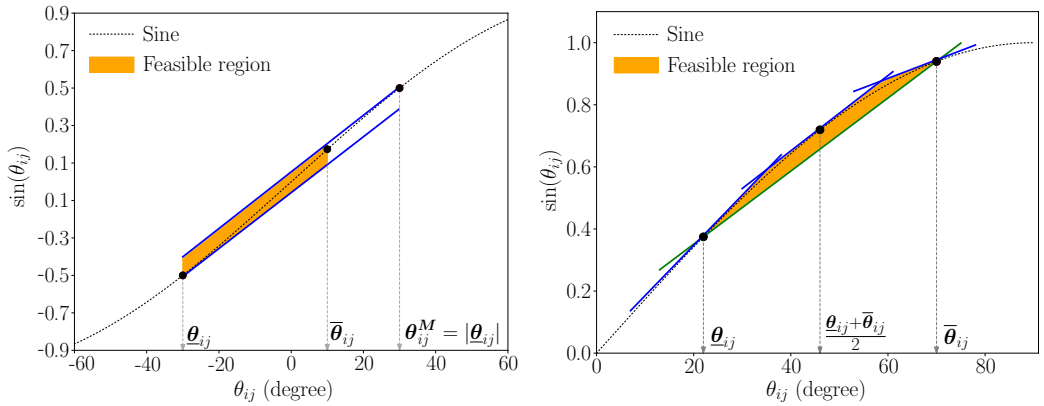

(a) Case (a) (b) Case (c)

Figure 2.1: Polyhedral relaxations for sinusoidal function

$[\underline{\boldsymbol{x}}_1, \overline{\boldsymbol{x}}_1]$, $[\underline{\boldsymbol{x}}_2, \overline{\boldsymbol{x}}_2]$, $[\underline{\boldsymbol{x}}_3, \overline{\boldsymbol{x}}_3]$, the extreme points of $\phi(\cdot)$ are given by the Cartesian product $(\underline{\boldsymbol{x}}_1, \overline{\boldsymbol{x}}_1) \times (\underline{\boldsymbol{x}}_2, \overline{\boldsymbol{x}}_2) \times (\underline{\boldsymbol{x}}_3, \overline{\boldsymbol{x}}_3) = \langle \boldsymbol{\xi}_1, \boldsymbol{\xi}_2, \ldots, \boldsymbol{\xi}_8 \rangle$. We use $\boldsymbol{\xi}^i_k$ to denote the coordinate of x_i in $\boldsymbol{\xi}_k$. The convex hull of the extreme points of $x_1 x_2 x_3$ is then given by

$$\sum_{k=1,\ldots,8} \lambda_k = 1, \quad \lambda_k \geqslant 0, \quad \forall k = 1, \ldots, 8, \tag{2.10a}$$

$$\widehat{x} = \sum_{k=1,\ldots,8} \lambda_k \phi(\boldsymbol{\xi}_k), \quad x_i = \sum_{k=1,\ldots,8} \lambda_k \boldsymbol{\xi}^i_k \tag{2.10b}$$

The notation $\langle x_1, x_2, x_3 \rangle^{\lambda}$ is used to denote the λ-based relaxation of a trilinear function as defined above. Thus, the relaxation of $x_1 x_2 x_3$ is stated as $\widehat{x} = \langle x_1, x_2, x_3 \rangle^{\lambda}$. We note that this formulation generalizes to any multilinear function and is equivalent to the standard McCormick relaxation for bilinear functions.

Current-magnitude constraints We also add the second-order conic constraints that connect apparent power flow on lines, (S_{ij}), with current magnitude squared variables, (l_{ij}) [33, 57]. The complete convex quadratic formulation with *tightest* trilinear relaxation of the ACOPF is then stated as:

$$\boldsymbol{\mathcal{P}^{QC}} := \min \sum_{i \in \mathcal{G}} \boldsymbol{c}_{2i} (\Re(S^g_i)^2) + \boldsymbol{c}_{1i} \Re(S^g_i) + \boldsymbol{c}_{0i} \tag{2.11a}$$

$$s.t. \quad (2.1b) - (2.1d), \tag{2.11b}$$

$$(2.1g) - (2.1j), \tag{2.11c}$$

$$W_{ii} = \widehat{w}_i, \ \widehat{w}_i \in \langle v_i^2 \rangle^R \quad \forall i \in \mathcal{N} \tag{2.11d}$$

$$\mathfrak{R}(W_{ij}) = \widehat{wc}_{ij}, \ \mathfrak{T}(W_{ij}) = \widehat{wsn}_{ij}, \quad \forall (i,j) \in \mathcal{E} \tag{2.11e}$$

$$\widehat{wc}_{ij} \in \langle v_i v_j \widehat{cs}_{ij} \rangle^{\lambda}, \ \widehat{wsn}_{ij} \in \langle v_i v_j \widehat{sn}_{ij} \rangle^{\lambda}, \tag{2.11f}$$

$$\widehat{cs}_{ij} \in \langle \cos(\theta_{ij}) \rangle^R, \ \widehat{sn}_{ij} \in \langle \sin(\theta_{ij}) \rangle^R, \tag{2.11g}$$

$$S_{ij} + S_{ji} = \boldsymbol{Z}_{ij} l_{ij} \quad \forall (i,j) \in \mathcal{E} \tag{2.11h}$$

$$|S_{ij}|^2 \leqslant W_{ii} l_{ij} \quad \forall (i,j) \in \mathcal{E}. \tag{2.11i}$$

2.4 Piecewise Convex Relaxations

One of the weaknesses of the convex quadratic relaxations described in section 2.3 is that the relaxation is not tight when the bounds of the variables are wide. To address this issue, recent work [27, 32] has developed approaches to tighten variable bounds, sometimes significantly. However, there are still a few OPF instances with large optimality gaps. In this section, we focus on developing tighter piecewise convex relaxations for quadratic and trilinear functions.

Piecewise trilinear functions In this section, we present a piecewise relaxation method to strengthen the convex-hull representation of the trilinear functions $v_i v_j \widehat{cs}_{ij}$ and $v_i v_j \widehat{sn}_{ij}$ described above (Eqs. (2.10)). This method is an extension of our preliminary study [73] which tightened these trilinear terms using the λ-based formulations for piecewise polyhedrons of multilinear functions [69, 90, 103, 106]. Recall that our preliminary method discretized the domain of each variable (i.e., v_i, v_j, $\widehat{cs}_{ij}$, and $\widehat{sn}_{ij}$) and introduced sufficient binary variables to control their partitions. However, this method may lose some information by partitioning on $\widehat{cs}$ and $\widehat{sn}$ independently. For example, $\widehat{cs}_{ij}$ and $\widehat{sn}_{ij}$ are functions of θ_{ij}, thus there are relationships among these variables which we can use when discretizing their domains. As a result, additional unnecessary partition (binary) variables are created,

which can significantly slow down the convergence. Instead, we partition only on θ_{ij} and apply specific partitions for $\widehat{cs}_{ij}$ and $\widehat{sn}_{ij}$. Without loss of generality and for the purpose of exposition, we illustrate piecewise polyhedral relaxations of trilinear functions with specific partitions on every variable (i.e., *two* partitions on v_i and v_j; *three* partitions on $\widehat{cs}_{ij}$ and $\widehat{sn}_{ij}$). For generalizations to multiple partitions and validity of the formulation, we refer the reader to Sundar *et al.* [103].

For notation brevity, variables v_i, v_j, $\widehat{cs}_{ij}$, $\widehat{sn}_{ij}$ and θ_{ij} are termed as x_1, x_2, x_3^c, x_3^s and θ_3 respectively. Let $\boldsymbol{x}_{i,j}$ be the j^{th} discretization point of x_i, and x_3 represents x_3^c or x_3^s. We define $z_{i,j} \in \{0,1\}$ as the binary partition variables corresponding to x_i on range j. The partitioned domains of variables x_3^c and x_3^s are graphically illustrated in Figure 2.2(a) and 2.2(b), respectively.

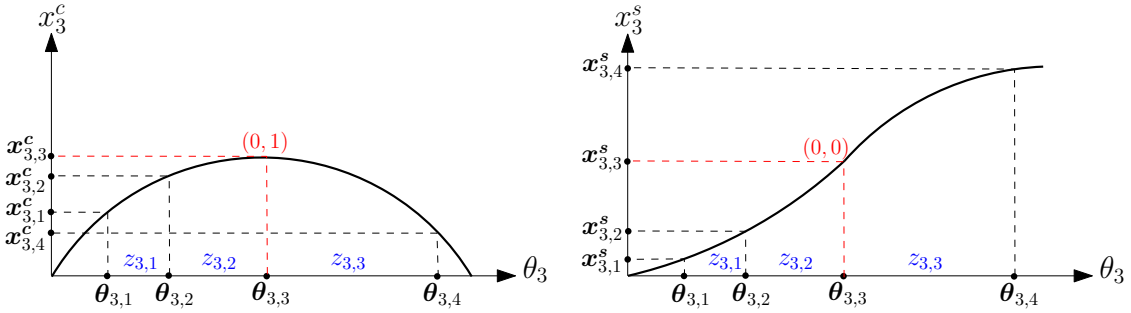

(a) $\cos(\theta_3)$ (b) $\sin(\theta_3)$

Figure 2.2: Partitioned domains for variable x_3^c and x_3^s, as a function of θ_3. Blue font indicates binary variables. Red font denotes the added points when $\underline{\theta}_3 \leqslant 0 \leqslant \overline{\theta}_3$.

These figures show that the discretization points of x_3^c and x_3^s are determined by partitions of θ_{ij}, rather than themselves. Particularly, as shown in Figure2.2, the domain of variable θ_3 is partitioned into *three* pieces by introducing *four* discretization points $\boldsymbol{\theta}_{3,k}, k \in \{1,2,3,4\}$, where $\underline{\boldsymbol{\theta}}_3 = \boldsymbol{\theta}_{3,1}$ and $\overline{\boldsymbol{\theta}}_3 = \boldsymbol{\theta}_{3,4}$. Given these points, the discretization points of x_3^c and x_3^s can be calculated as $\boldsymbol{x}_{3,j}^{\boldsymbol{c}} = \cos(\boldsymbol{\theta}_{3,j})$ and $\boldsymbol{x}_{3,j}^{\boldsymbol{s}} = \sin(\boldsymbol{\theta}_{3,j})$ for each $j \in \{1,2,3,4\}$. In this case, we present domains of x_3^c and x_3^s below:

$$x_3^c \in [\boldsymbol{x}_{3,1}^{\boldsymbol{c}}, \boldsymbol{x}_{3,2}^{\boldsymbol{c}}] \cup [\boldsymbol{x}_{3,2}^{\boldsymbol{c}}, \boldsymbol{x}_{3,3}^{\boldsymbol{c}}] \cup [\boldsymbol{x}_{3,4}^{\boldsymbol{c}}, \boldsymbol{x}_{3,3}^{\boldsymbol{c}}] \tag{2.12a}$$

$$x_3^s \in [\boldsymbol{x}_{3,1}^{\boldsymbol{s}}, \boldsymbol{x}_{3,2}^{\boldsymbol{s}}] \cup [\boldsymbol{x}_{3,2}^{\boldsymbol{s}}, \boldsymbol{x}_{3,3}^{\boldsymbol{s}}] \cup [\boldsymbol{x}_{3,3}^{\boldsymbol{s}}, \boldsymbol{x}_{3,4}^{\boldsymbol{s}}] \tag{2.12b}$$

It is important to notice that cosine function $f(\theta)$ is not monotonic if $\underline{\theta} \leqslant 0 \leqslant \overline{\theta}$ (here we assume that $|\underline{\theta}| \leqslant \frac{\pi}{2}$ and $|\overline{\theta}| \leqslant \frac{\pi}{2}$). Thus, this approach may lead to the loss of some valid domains of x_3^c. For example, if the domain of θ_3 is partitioned by *three* discretization points $\boldsymbol{\theta}_{3,1}$, $\boldsymbol{\theta}_{3,2}$, and $\boldsymbol{\theta}_{3,4}$, which generate *three* discretization points $\boldsymbol{x}_{3,1}^{\boldsymbol{c}}$, $\boldsymbol{x}_{3,2}^{\boldsymbol{c}}$, and $\boldsymbol{x}_{3,4}^{\boldsymbol{c}}$ for $\boldsymbol{x}_3^{\boldsymbol{c}}$. This implies that $\boldsymbol{x}_3^{\boldsymbol{c}} \in [\boldsymbol{x}_{3,1}^{\boldsymbol{c}}, \boldsymbol{x}_{3,2}^{\boldsymbol{c}}] \cup [\boldsymbol{x}_{3,4}^{\boldsymbol{c}}, \boldsymbol{x}_{3,2}^{\boldsymbol{c}}]$, thus a valid range $[\boldsymbol{x}_{3,2}^{\boldsymbol{c}}, \boldsymbol{x}_{3,3}^{\boldsymbol{c}}]$ is neglected. This issue can be simply addressed by adding one discretization point $\boldsymbol{\theta}_{3,k}$ such that $cos(\boldsymbol{\theta}_{3,k}) = 1$ (e.g., $\boldsymbol{\theta}_{3,3}$ in Figure2.2). As a result, when $\underline{\theta}_3 \leqslant 0 \leqslant \overline{\theta}_3$, the true upper bound of x_3^c (i.e., 1) is always included in its domain and no sub-domains are neglected.

Further, it is evident that x_3^c is monotonically increasing and decreasing with respect to the left-side domain and the right-side domain of θ_3 (i.e., $[\boldsymbol{\theta}_{3,1}, 0]$ and $[0, \boldsymbol{\theta}_{3,4}]$), respectively. This property facilitates the derivation of piecewise convex-hull representations of $v_i v_j \widehat{cs}_{ij}$ and $v_i v_j \widehat{sn}_{ij}$ with partitions on variable θ_{ij} (will discuss later). Meanwhile, although sine function $f(\theta)$ is always monotonic when $\underline{\theta}_3 \leqslant 0 \leqslant \overline{\theta}_3$, the point $\boldsymbol{x}_{3,3}^{\boldsymbol{s}} = 0$ must be added to the discretization point set of x_3^s. This is due to x_3^c and x_3^s use the same binary variables (i.e., $z_{3,1}$, $z_{3,2}$ and $z_{3,3}$ in Figure2.2) to control partitions. Finally, it is important to note that when $\underline{\theta}_3 > 0$ or $\overline{\theta}_3 < 0$, the discretization points $\boldsymbol{x}_{3,3}^{\boldsymbol{c}} = 1$ and $\boldsymbol{x}_{3,3}^{\boldsymbol{s}} = 0$ are infeasible for x_3^c and x_3^s, respectively. In this case, these two points must be excluded and should not be added to the discretization point sets of x_3^c and x_3^s.

Let $\mathcal{K} = \{1, .., 36\}$ be the set of integer values between 1 and 36. Recall that for $k \in \mathcal{K}$, $\boldsymbol{\xi}_k$ denotes the coordinates of the k^{th} extreme point of a trilinear function $\phi(\cdot)$ and $\boldsymbol{\xi}_k^i$ denotes the coordinate of x_i in $\boldsymbol{\xi}_k$. For every extreme point, $\boldsymbol{\xi}_k$, there is a nonnegative mulitiplier variable λ_k. The partitioned domains of trilinear functions are graphically illustrated in Figure2.3.

Using these notations and partitioning scheme above, we now present the SOS-II (i.e., a special order set of type II [9]) constraints that model the piecewise union of

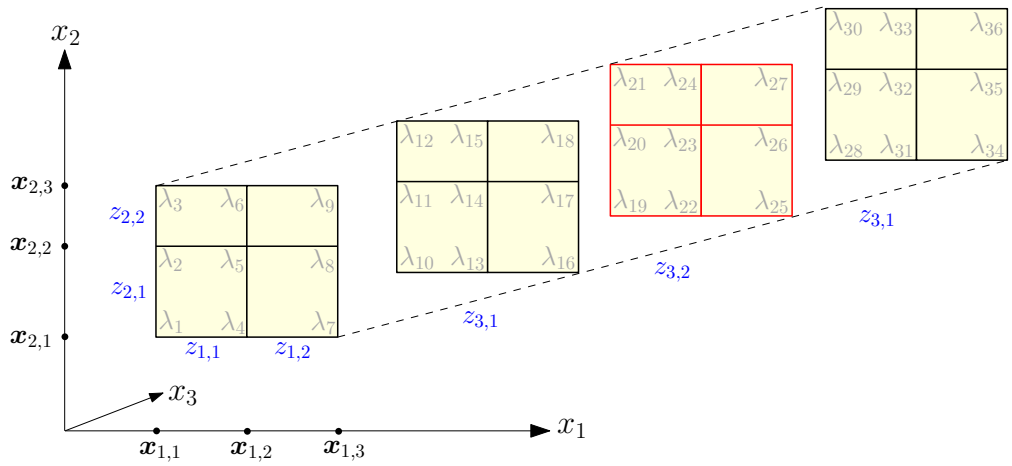

Figure 2.3: Partitioned variable domains for a trilinear function. Blue font indicates binary variables. The red slice represents the partitioned domains associated with the added points when $\underline{\theta}_3 \leqslant 0 \leqslant \overline{\theta}_3$ (i.e., If $\underline{\theta}_3 > 0$ or $\overline{\theta}_3 < 0$, this slice is not included).

polyhedrons of the trilinear function below:

$$\widehat{x} = \sum_{k \in \mathcal{K}} \lambda_k \phi(\boldsymbol{\xi}_k), \quad x_i = \sum_{k \in \mathcal{K}} \lambda_k \boldsymbol{\xi}_k^i, \tag{2.13a}$$

$$\sum_{k \in \mathcal{K}} \lambda_k = 1, \quad \lambda_k \geqslant 0, \ \forall k \in \mathcal{K}, \tag{2.13b}$$

$$z_{i,1}, z_{i,2} \in \{0,1\}, \quad z_{i,1} + z_{i,2} = 1, \ \forall i = 1, .., , 2 \tag{2.13c}$$

$$z_{3,1}, z_{3,2}, z_{3,3} \in \{0,1\}, \quad z_{3,1} + z_{3,2} + z_{3,3} = 1, \tag{2.13d}$$

$$z_{1,1} \geqslant \sum_{k \in \tilde{\mathcal{K}}} \lambda_k, \ \tilde{\mathcal{K}} = \{1,2,3,10,11,12,19,20,21,28,29,30\}, \tag{2.13e}$$

$$z_{1,2} \geqslant \sum_{k \in \tilde{\mathcal{K}}} \lambda_k, \ \tilde{\mathcal{K}} = \{7,8,9,16,17,18,25,26,27,34,35,36\}, \tag{2.13f}$$

$$z_{2,1} \geqslant \sum_{k \in \tilde{\mathcal{K}}} \lambda_k, \ \tilde{\mathcal{K}} = \{1,4,7,10,13,16,9,22,25,28,31,34\}, \tag{2.13g}$$

$$z_{2,2} \geqslant \sum_{k \in \tilde{\mathcal{K}}} \lambda_k, \ \tilde{\mathcal{K}} = \{3,6,9,12,15,18,21,24,27,30,33,36\}, \tag{2.13h}$$

$$z_{1,1} + z_{1,2} \geqslant \sum_{k \in \tilde{\mathcal{K}}} \lambda_k, \ \tilde{\mathcal{K}} = \{4,5,6,13,14,15,22,23,24,31,32,33\}, \tag{2.13i}$$

$$z_{2,1} + z_{2,2} \geqslant \sum_{k \in \tilde{\mathcal{K}}} \lambda_k, \ \tilde{\mathcal{K}} = \{2,5,8,11,14,17,20,23,26,29,32,35\}, \tag{2.13j}$$

$$z_{3,1} \geqslant \sum_{k=1}^{9} \lambda_k, \quad z_{3,1} + z_{3,2} \geqslant \sum_{k=10}^{18} \lambda_k, \quad z_{3,2} + z_{3,3} \geqslant \sum_{k=19}^{27} \lambda_k, \quad z_{3,3} \geqslant \sum_{k=28}^{36} \lambda_k. \tag{2.13k}$$

Constraints (2.13a)-(2.13d) model the convex combination of extreme points and disjunctions. They force one partition for each variable to be active. Constraints (2.13e)-(2.13k) enforce the adjacency conditions for the λ variables. These resemble SOS-II constraints. The formulation in (2.13) has many interesting polyhedral properties. For example, the projection of this polytope on to the space of $\{x_1, x_2, x_3, \widehat{x}\}$ has integral extreme points. This is one of the primary reasons this formulation can be computationally efficient For further theoretical details, we delegate the reader to [69, 106].

Piecewise quadratic functions Using the same notation, the partitioned domains of quadratic functions are graphically illustrated in Figure 2.4. The SOS-II constraints of

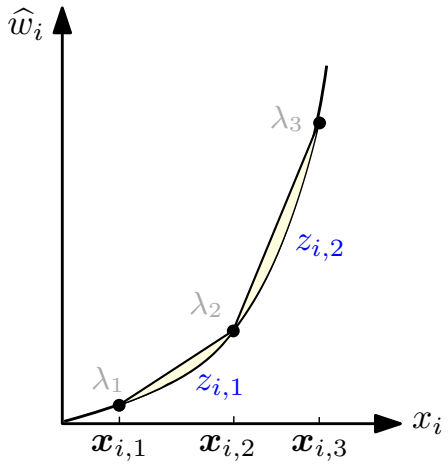

Figure 2.4: Piecewise quadratic regions. Blue font indicates binary variables.

piecewise quadratic constraints are modeled as the following, using a piecewise union of convex quadratic regions. To the best of our knowledge, this is the first time the piecewise quadratic regions of the voltage squared variables have been modeling using the λ formulation.

$$\widehat{w}_i \geqslant x_i^2, \quad \widehat{w}_i \leqslant \sum_{k=1,2,3} \lambda_k \boldsymbol{x}_{i,k}^2, \quad x_i = \sum_{k=1,2,3} \lambda_k \boldsymbol{x}_{i,k}, \tag{2.14a}$$

$$\sum_{k=1,2,3} \lambda_k = 1, \quad \lambda_k \geqslant 0, \ \forall k = 1,2,3, \tag{2.14b}$$

$$z_{i,1}, z_{i,2} \in \{0,1\}, \quad z_{i,1} + z_{i,2} = 1, \tag{2.14c}$$

$$z_{i,1} \geqslant \lambda_1, \quad z_{i,2} \geqslant \lambda_3, \quad z_{i,1} + z_{i,2} \geqslant \lambda_2. \tag{2.14d}$$

Strengthening valid inequalities Though the formulations in (2.13) and (2.14) are *necessary and sufficient* to characterize the piecewise relaxations of trilinear and quadratic functions, we observed that the inclusion of the following (simple) valid constraints improved the computational performance of λ formulations tremendously. For a given variable x_i with two partitions (i.e., $x_i \in [\boldsymbol{x}_{i,1}, \boldsymbol{x}_{i,2}] \cup [\boldsymbol{x}_{i,2}, \boldsymbol{x}_{i,3}]$), the constraint is as follows:

$$z_{i,1}\boldsymbol{x}_{i,1} + z_{i,2}\boldsymbol{x}_{i,2} \leqslant x_i \leqslant z_{i,1}\boldsymbol{x}_{i,2} + z_{i,2}\boldsymbol{x}_{i,3} \tag{2.15}$$

Finally, for a given trilinear or quadratic function with a finite number of partitions, we use $\langle\cdot\rangle^{\lambda_p}$ to denote the piecewise λ-formulation of (2.13) and (2.14), respectively. The complete piecewise convex relaxation of the ACOPF is then stated as:

$$\boldsymbol{\mathcal{P}^{QC^{\lambda}}} := \min \sum_{i \in \mathcal{G}} \boldsymbol{c}_{2i}(\mathfrak{R}(S_i^g)^2) + \boldsymbol{c}_{1i}\mathfrak{R}(S_i^g) + \boldsymbol{c}_{0i} \tag{2.16a}$$

$$s.t. \ \ (2.1b) - (2.1d), \ (2.1g) - (2.1j) \tag{2.16b}$$

$$(2.11e), \ (2.11h) - (2.11i) \tag{2.16c}$$

$$W_{ii} = \widehat{w}_i, \ \widehat{w}_i \in \langle v_i^2 \rangle^{\lambda_p} \quad \forall i \in \mathcal{N} \tag{2.16d}$$

$$\widehat{wc}_{ij} \in \langle v_i v_j \widehat{cs}_{ij} \rangle^{\lambda_p}, \ \widehat{wsn}_{ij} \in \langle v_i v_j \widehat{sn}_{ij} \rangle^{\lambda_p}. \tag{2.16e}$$

2.5 Global optimization of ACOPF

Adaptive Multivariate Partitioning To solve the ACOPF problem, we use the Adaptive Multivariate Partitioning (AMP) algorithm described in [82, 83]. The key idea of this method is that AMP leverages the observations that solutions based on relaxations to

ACOPF are often tight in practice and that locally optimal solutions are also very good [57]. AMP iteratively introduces narrow partitions around these relaxations.

A high-level pseudo-code for AMP is given in Algorithm 1. In this algorithm, we use the notation σ to denote a solution to the ACOPF, $f(\sigma)$ to denote the objective value of σ, and $\sigma(x)$ to denote the assignment of variable x in σ. In Lines 2-3, a feasible solution,

Algorithm 1 Adaptive Multivariate Partitioning (AMP)

1: **function** AMP
2: $\quad\overline{\sigma} \leftarrow$ Solve($\mathcal{P}$)
3: $\quad\underline{\sigma} \leftarrow$ Solve($\mathcal{P}^{QC}$)
4: $\quad\underline{\theta}_{ij}, \overline{\theta}_{ij}, \underline{v}_i, \overline{v}_i, \underline{\widehat{cs}}_{ij}, \overline{\widehat{cs}}_{ij}, \underline{\widehat{sn}}_{ij}, \overline{\widehat{sn}}_{ij} \leftarrow$TightenBounds($\overline{\sigma}$)
5: $\quad\mathcal{X} \leftarrow$SelectPartitionVariables($\overline{\sigma}, \underline{\sigma}$)
6: $\quad\mathcal{I} \leftarrow$InitializePartitions($\mathcal{X}, \mathcal{P}, \overline{\sigma}$)
7: $\quad\underline{\sigma} \leftarrow$ Solve($\mathcal{P}^{QC^{\lambda(\mathcal{I})}}$)
8: $\quad$**while** $\left(\frac{f(\overline{\sigma})-f(\underline{\sigma})}{f(\underline{\sigma})} \geqslant \epsilon\right)$ and (Time $\leqslant$ Timeout) **do**
9: $\quad\quad\mathcal{I} \leftarrow$TightenPartitions($x^{\mathcal{I}}, \mathcal{P}, \underline{\sigma}$)
10: $\quad\quad\underline{\sigma} \leftarrow$Solve($\mathcal{P}^{QC^{\lambda(\mathcal{I})}}$)
11: $\quad\quad\widehat{\sigma} \leftarrow$Solve($\mathcal{P}, \underline{\sigma}$)
12: $\quad\quad$**if** $f(\widehat{\sigma}) < f(\overline{\sigma})$ **then**
13: $\quad\quad\quad\overline{\sigma} \leftarrow \widehat{\sigma}$
14: $\quad\quad\quad\mathcal{X} \leftarrow$ SelectPartitionVariables($\overline{\sigma}, \underline{\sigma}$)
15: $\quad\quad$**end if**
16: $\quad$**end while**
17: $\quad$**return** $\underline{\sigma}, \overline{\sigma}$
18: **end function**

$\overline{\sigma}$, and a lower bound, $\underline{\sigma}$, are computed. Here, the lower bound is computed without partitioning any variables. In line 4, we sequentially tighten the bounds of the voltage magnitude, v_i, and phase angle differences, θ_{ij}, using optimization-based bound tightening (BT) [27, 32]. The new bounds on θ_{ij} are used to tighten $\widehat{cs}_{ij}$ and $\widehat{sn}_{ij}$ using the cases defined in equations (2.4)-(2.9). We would like to note that, though the importance of BT has been already observed for ACOPF problems, the bounds we obtain in this paper are tighter than in [27, 32] since formulation (2.11) is based on the convex-hull representation of trilinear functions.

Line 5 describes our variable selection strategy for partitioning (discussed later). This is one main point of departure (and contribution) from the AMP algorithm discussed

in [82]. Line 6 initializes the piecewise partitions of variables in $\mathcal{X}$ around those variables' assignments in $\overline{\sigma}$ (see Figure 2.5). It is important to note that, if $\theta_{ij} \in \mathcal{X}$, the calculated partitions for variables $\widehat{cs}_{ij}$ and $\widehat{sn}_{ij}$ (as described earlier) are included in $\mathcal{I}$. Line 7 then updates the lower bound using the piecewise relaxation. Line 9 updates the partition set $\mathcal{I}$ by adding new partitions associated with variables in $\mathcal{X}$ around the updated lower bound (see Figure 2.5). Again, if $\theta_{ij} \in \mathcal{X}$, the partitions for $\widehat{cs}_{ij}$ and $\widehat{sn}_{ij}$ are updated in $\mathcal{I}$ accordingly. Note that we don not remove any partitions that have been added from all preceding processes. Lines 10-13 then update the upper and lower bounds of the ACOPF. The upper bound (feasible solution) is updated by fixing the the ACOPF to the partition selected in $\underline{\sigma}$ and attempting to find a (better) feasible solution using a local solver. Line 14 redefines $\mathcal{X}$, a set of variables selected for partitioning, based on the updated lower- and upper-bound solutions from lines 10-13. The process is repeated until the objective values of the upper and lower bound converge or a time-out criteria is met (Line 8). The full details of these procedures are discussed in [82], except for line 14 which describes a heuristic for updating the selection of variables to be partitioned in next iteration. We also note that this is the first time this algorithm has been applied to ACOPF represented in the polar form.

Heuristic partition-variable selection Algorithm 2 describes in more detail about our variable selection strategy for partitioning. The original implementation of AMP selects a sufficient number of variables to ensure that all relaxed functions are partitioned and tightened. This approach ensures convergence to global optimality, but in practice, such an approach is computationally difficult to solve when the number of binary variables is large. Here, we introduce a heuristic that limits the number of variables that are partitioned. While convergence is no longer assured, this heuristic can have a considerable impact on solution quality.

Let $\mathcal{V} = \{v_i, \theta_{ij},\ \forall i \in \mathcal{N}, ij \in \mathcal{E}\}$ represent the set of candidate variables for partitioning. In Algorithm 2, Line 2 computes the difference between a variable's (x_i) assignment in an upper- and a lower-bound solution. Line 3 sorts the variables in $\mathcal{V}$ by increasing

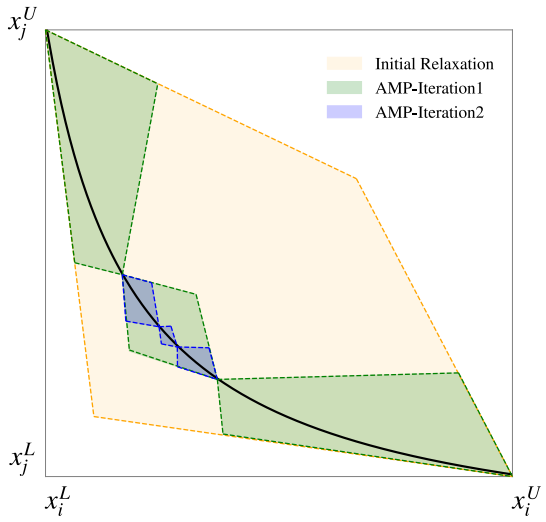

Figure 2.5: Example of variable partitioning in AMP for a bilinear function. Given an initial relaxation (tan region) and an initial feasible point (middle of the black curve), the function InitializePartitions creates a narrow partition around the feasible point (middle green region) and two wide partitions (outer green regions) around it. The size of the narrow partition is controlled by a user parameter, Δ. The relaxation is iteratively tightened by the function TightenPartitions around relaxed solutions. This figure shows the partitioning of one iteration (blue regions).

value of this difference. Line 4 returns the the first $\alpha|\mathcal{S}|$ variables, where α is a user defined parameter between 0 and 1. This heuristic relies on an expectation that variables whose assignments from the non-partitioned convex relaxation are very different from the local feasible solution are indeed the variables that require further refinement in the relaxed space. Note that when $\alpha = 100\%$ this heuristic reverts to the original AMP algorithm.

Algorithm 2 Heuristic Partition-Variable Selection

1: **function** SelectPartitionVariables($\overline{\sigma}, \underline{\sigma}$)
2: $\quad x_i^\delta \leftarrow |\overline{\sigma}(x_i) - \underline{\sigma}(x_i)|, \quad \forall i = 1, \ldots, |\mathcal{V}|$
3: $\quad \mathcal{S} \leftarrow \{x_1, x_2, \ldots, x_{|\mathcal{V}|}\} : x_i \in \mathcal{V}$ and $x_i^\delta \geqslant x_{i+1}^\delta$
4: $\quad$ **return** $\bigcup x_i : i \leqslant \alpha|\mathcal{S}|$
5: **end function**

Addtitionally, we also update set $\mathcal{X}$ based on the gap between the updated lower- and upper-bound solutions for each variable in $\mathcal{V}$. Particularly, in each iteration, $\mathcal{X}$ is either kept the same or updated by changing at least one variable, while its size is always equal to $\alpha|\mathcal{S}|$. As a result, a limited number of new partitions are created and added to

the partition set $\mathcal{I}$, which can significantly reduce computational efforts. Meanwhile, for any variable ever appeared in $\mathcal{X}$, its associated partitions are never removed from $\mathcal{I}$. For example, consider a problem with two variables x_1 and x_2 where only one variable is allowed for partitioning. Assume in the first iteration, $\mathcal{X} := \{x_1\}$ and the associated partition set is $\mathcal{I} := \{x_1 \in [\boldsymbol{x}_{1,1}, \boldsymbol{x}_{1,2}] \cup [\boldsymbol{x}_{1,2}, \boldsymbol{x}_{1,3}]\}$. In the next iteration, assume x_2 is selected to be partitioned and its partitioned domains are $x_2 \in [\boldsymbol{x}_{2,1}, \boldsymbol{x}_{2,2}] \cup [\boldsymbol{x}_{2,2}, \boldsymbol{x}_{2,3}]$. Using our heuristic method, the updated $\mathcal{X}$ and $\mathcal{I}$ will be $\mathcal{X} := \{x_2\}$ and $\mathcal{I} := \big\{x_1 \in [\boldsymbol{x}_{1,1}, \boldsymbol{x}_{1,2}] \cup [\boldsymbol{x}_{1,2}, \boldsymbol{x}_{1,3}],\ x_2 \in [\boldsymbol{x}_{2,1}, \boldsymbol{x}_{2,2}] \cup [\boldsymbol{x}_{2,2}, \boldsymbol{x}_{2,3}]\big\}$. We acknowledge that there can be numerous other branching strategies which can lead to better convergence of AMP, which we leave for the future work.

2.6 Numerical Results

In remainder of this chapter, BT refers to bound tightening using the tightened convex quadratic relaxations introduced in section 2.3. QC$^{\text{conv}}$ and BT-QC$^{\text{conv}}$ correspond to improved QC relaxation and bound-tightening applied with convex-hull trilinear formulation (2.11). BT-Lambda-θ and BT-Lambda-θ-α refer to Algorithm 1 with and without heuristic partitions, respectively (i.e., $\alpha < 100\%$ and $\alpha = 100\%$). BT-Lambda refers to the AMP algorithm with individual partitions on the $\widehat{cs}_{ij}$ and $\widehat{sn}_{ij}$ variables in trilinear products and without heuristic partitions. For more details about this algorithm, we refer the reader to our earlier work [73]. The performance of these algorithms are evaluated on the ACOPF test cases from NESTA 0.7.0 [31]. These test cases were selected because the basic QC optimality gaps were larger than 1% and hence hard for global optimization. Here, Ipopt 3.12.1 is used to find the feasible solution $\overline{\boldsymbol{\sigma}}$ in AMP. The relaxed problems are solved using Gurobi 7.0.2 with default options and presolver switched on.

In Algorithm 1, the value of ϵ and the "time-out" parameter were set to 0.01 and 18000.0 seconds, respectively. A 10800-second time-limit was imposed on the BT procedure. All the algorithms were implemented using Julia/JuMP [36]. All the computational experiments were performed using the HPC Palmetto cluster at Clemson University with

Intel Xeon E5-2670v2, 20 cores and 120GB of memory.

2.6.1 Performance Comparison of Algorithms

In Table 2.1, we summarize the computational performance of all algorithms without heuristic partitions. The first two columns present the initial local feasible solution $\overline{\boldsymbol{\sigma}}$ and the initial lower bound $\underline{\boldsymbol{\sigma}}$, respectively. Columns three and four present the optimality gaps of [33] and [63], respectively. The remaining columns show the performance of BT, BT-Lambda, and BT-Lambda-θ, respectively. The results in Table 2.1 show that, due to the convex-hull relaxation of trilinear functions, the QC^{conv} gaps (highlighted in bold font in Table 2.1) outperformed the recursive McCormick approach used in [33]. Table 2.2 tabulates a few instances in which the improvements in QC gaps were significant based on the proposed approach. Even during bound-tightening, the best QC gaps found using recursive McCormick ($\text{BT-QC}^{\text{rmc}}$) for trilinear functions were 2.7% and 11.8% for case30_fsr_api and case118_ieee_api, respectively. However, applying the convex-hull representation ($\text{BT-QC}^{\text{conv}}$) for the same instances reduced the gaps to 0.35% and 8.54%, respectively.

Meanwhile, the optimality gaps for BT-Lambda and BT-Lambda-θ are consistently smaller than QC^{conv}, SDP gaps, and the best gaps in [63]. In 25 out of 35 test instances, the globally optimal solution is found by BT-Lambda-θ (i.e., Gap $< 0.01\%$). Further, four of the sub-optimal solutions have gaps less than 0.2% and we observe that BT-Lambda-θ outperforms BT-Lambda in 10 out of 35 instances. For example, for case189_edin_api, the global optimal is found by BT-Lambda-θ within the allowable time limit, while the gap for BT-Lambda is 0.03% when the time limit is reached; for case300_ieee, BT-Lambda-θ finds the global optimal solution in 953.1 seconds, which is two times faster than BT-Lambda. It could be because partitioning θ_{ij} introduces less discrete variables and results in more efficient local bounds of trilinear terms to tighten relaxations.

Table 2.1: The performance summary of all algorithms without heuristic partitions for NESTA 0.7.0 ACOPF instances. Values under "Gap" and "T,T^{θ}" are in % and seconds, respectively. "GOpt" refers to the global optimum when Gap < 0.01%. "TO" indicates time-out. "–" indicates no solution is provided under "SDP" and "Best of [63]" columns. "–" under "BT-Lambda" and "BT-Lambda-θ" columns indicates that the BT-QC$^{\text{conv}}$ already converged to global optimum. Here, Δ^* represents the best one from {4, 6, 8, 10, 16}.

							BT-Lambda [73]		BT-Lambda–θ	
Instances	AC ($)	QC$^{\text{conv}}$ (%)	SDP (%)	Best of [63] (%)	BT$^{\text{conv}}$ (s)	BT-QC$^{\text{conv}}$ (%)	(Δ^*) Gap	T	(Δ^*) Gap	T^{θ}
case3_lmbd	5812.64	**0.97**	0.39	0.09	2.1	GOpt	(16) GOpt	–	(8) GOpt	–
case5_pjm	17551.90	14.54	5.22	0.10	0.9	6.73	(6) GOpt	303.7	(6) 0.01	TO
case30_ieee	204.97	**15.20**	GOpt	–	48.1	GOpt	(16) GOpt	–	(8) GOpt	–
case118_ieee	3718.64	**1.53**	0.06	0.09	2235.0	GOpt	(10) GOpt	–	(20) GOpt	–
case162_ieee_dtc	4230.23	3.95	1.33	1.08	6292.3	GOpt	(10) GOpt	–	(20) GOpt	–
case240_wecc	75136.10	**5.23**	–	–	10800.0	2.90	(6) 2.64	TO	(20) 2.55	TO
case300_ieee	16891.28	1.17	0.08	0.19	10800.0	0.01	(20) GOpt	2164.2	(20) GOpt	953.1
case3_lmbd_api	367.44	**1.59**	1.26	0.02	0.3	GOpt	(16) GOpt	–	(8) GOpt	–
case14_ieee_api	325.13	1.26	GOpt	0.09	11.7	0.06	(8) GOpt	0.4	(20) GOpt	0.2
case24_ieee_rts_api	6426.65	**8.79**	1.45	–	72.8	GOpt	(8) GOpt	–	(20) GOpt	–
case30_as_api	570.08	4.63	0.00	0.06	47.1	GOpt	(16) GOpt	–	(20) GOpt	–
case30_fsr_api	366.57	45.20	11.06	0.35	101.8	0.35	(6) 0.12	TO	(6) 0.12	TO
case39_epri_api	7460.37	2.97	GOpt	–	96.7	GOpt	(16) GOpt	–	(20) GOpt	–
case73_ieee_rts_api	19995.00	**9.64**	4.29	–	1528.2	0.01	(10) GOpt	61.2	(20) GOpt	27.9
case89_pegase_api	4255.44	19.83	18.11	–	3997.3	16.21	(6) 13.46	TO	(6) 13.7	TO
case118_ieee_api	10269.82	43.45	31.50	6.17	1515.6	8.54	(6) 4.19	TO	(6) 0.9	TO
case162_ieee_dtc_api	6106.86	1.25	0.85	1.03	6392.6	GOpt	(6) GOpt	–	(20) GOpt	–
case189_edin_api	1914.15	1.69	0.05	0.12	5110.9	0.04	(8) 0.03	TO	(6) GOpt	12825.1
case3_lmbd_sad	5959.33	**1.38**	2.06	0.03	0.2	GOpt	(16) GOpt	–	(20) GOpt	–
case4_gs_sad	315.84	**0.96**	0.05	–	0.3	GOpt	(10) GOpt	–	(6) GOpt	–
case24_ieee_rts_sad	76943.24	**2.77**	6.05	–	44.7	GOpt	(6) GOpt	–	(10) GOpt	–
case29_edin_sad	41258.45	16.38	28.44	0.67	222.4	GOpt	(16) GOpt	–	(16) GOpt	–
case30_as_sad	897.49	2.32	0.47	0.08	53.8	GOpt	(16) GOpt	–	(20) GOpt	–
case30_ieee_sad	204.97	**4.01**	GOpt	0.08	50.4	GOpt	(16) GOpt	–	(10) GOpt	–
case73_ieee_rts_sad	227745.73	**2.38**	4.10	–	1655.8	GOpt	(6) GOpt	–	(16) GOpt	–
case118_ieee_sad	4106.72	**4.15**	7.57	2.43	2211.4	GOpt	(8) GOpt	–	(20) GOpt	–
case162_ieee_dtc_sad	4253.51	4.27	3.65	3.76	6337.2	0.01	(10) GOpt	88.5	(20) GOpt	39.8
case240_wecc_sad	76494.70	**5.27**	–	–	10800.0	2.61	(8) 2.41	TO	(6) 2.43	TO
case300_ieee_sad	16893.92	1.09	0.13	0.10	10800.0	GOpt	(10) GOpt	–	(20) GOpt	–
case5_bgm_nco	1082.33	10.17	–	–	6.93	GOpt	(6) GOpt	–	(16) GOpt	–
case9_bgm_nco	3087.84	10.84	–	–	2.72	10.80	(16) 10.12	TO	(6) 8.44	TO
case9_na_cao_nco	-212.43	**-14.97**	–	–	2.14	-6.90	(6) -0.04	TO	(6) -0.05	TO
case9_nb_cao_nco	-247.42	-15.59	–	–	2.62	-6.93	(6) -0.09	TO	(6) -0.07	TO
case14_s_cao_nco	9670.44	3.83	–	–	16.22	2.34	(6) 0.04	TO	(8) 0.04	TO
case39_1_bgm_nco	11221.00	3.72	–	–	103.98	3.58	(8) 3.46	TO	(16) 3.39	TO

Table 2.2: QC relaxation gaps with trilinear functions relaxed using recursive McCormick (QC^{rmc}) versus convex-hull representation (QC^{conv}).

Instances	QC^{rmc} (%)	QC^{conv} (%)
case3_lmbd	1.21	0.96
case30_ieee	15.64	15.20
case3_lmbd_api	1.79	1.59
case24_ieee_rts_api	11.88	8.78
case73_ieee_rts_api	10.97	9.64
case3_lmbd_sad	1.42	1.37
case4_gs_sad	1.53	0.96
case5_pjm_sad	0.99	0.77
case24_ieee_rts_sad	2.93	2.77
case73_ieee_rts_sad	2.53	2.38
case118_ieee_sad	4.61	4.14

In Table 2.1, there are 16 instances for which BT-QC^{conv} does not converge to the global optimum. Next, we test the performance of the heuristic partitioning scheme on these instances: Table 2.3 summarizes the computational gaps and solution times for four different values of α: 20%, 40%, 60% and 80%. The results show that the performance of the heuristic partitioning algorithm heavily depends on α. For example, in case300_ieee, the global optimum is found for all values of α, but the resulting run times vary widely. Further, in case189_edin_api, "GOpt" is found when α equals 60% and 80%, while the solution does not converge to the global optimum within the allowable time limit when α equals 20% or 40%. Second, we observe that in 9 of 16 test cases (highlighted in bold under the "Instances" column), BT-Lambda-θ-α outperforms both BT-Lambda and BT-Lambda-θ for some values of α. For example, in case240_wecc, case89_pegase_api, case240_wecc_sad, case9_bgm_nco, and case39_1_bgm_nco, smaller optimality gaps are found by the heuristic. Also, in case189_edin_api, though the global optimum can be found by both BT-Lambda-θ and BT-Lambda-θ-α(60% and 80%), the required computation time is significantly reduced by the heuristic partitioning algorithm (e.g., time difference between BT-Lambda-θ and BT-Lambda-θ-α(80%) is 5329 s). The superior performance of BT-Lambda-θ-α could be

due to the fact that less discrete variables are introduced to control partitions and the number of partitioned variables selected heuristically are sufficient to tighten relaxations.

Table 2.3: The performance of heuristic partitioning scheme for NESTA 0.7.0 ACOPF instances. Values under "Gap" and "T^{α}" are in % and seconds, respectively. "GOpt" refers to the global optimum when Gap $< 0.01\%$. "TO" indicates time-out. Δ^* represents the best one from {4, 6, 8, 10, 16}.

	BT-Lambda–θ–α(20%)		BT-Lambda–θ–α(40%)		BT-Lambda–θ–α(60%)		BT-Lambda–θ–α(80%)	
Instances	(Δ^*) Gap	T^{α}	(Δ^*) Gap	T^{α}	(Δ^*) Gap	T^{α}	(Δ^*) Gap	T^{α}
case5_pjm	(16) 4.58	TO	(10) 0.36	TO	(6) 0.05	TO	(6) 0.02	TO
case240_wecc	**(6) 1.94**	TO	**(10) 1.74**	TO	(16) 2.63	TO	(20) 2.59	TO
case300_ieee	(20) GOpt	583.05	(20) GOpt	908.68	(20) GOpt	614.43	(20) GOpt	694.68
case14_ieee_api	(10) GOpt	0.17	(16) GOpt	0.17	(16) GOpt	0.17	(16) GOpt	0.05
case30_fsr_api	(10) 0.34	TO	(8) 0.31	TO	(6) 0.13	TO	(6) 0.13	TO
case73_ieee_rts_api	(16) GOpt	6.48	(8) GOpt	21.70	(20) GOpt	17.45	(8) GOpt	23.64
case89_pegase_api	**(8) 6.75**	TO	(6) 12.60	TO	**(6) 2.09**	TO	(20) 11.98	TO
case118_ieee_api	(20) 6.84	TO	(16) 4.07	TO	(16) 3.27	TO	(10) 1.13	TO
case189_edin_api	(8) 0.03	TO	(8) 0.03	TO	(6) GOpt	8254.67	(20) GOpt	7495.57
case162_ieee_dtc_sad	(20) GOpt	42.35	(20) GOpt	39.90	(20) GOpt	66.49	(20) GOpt	36.29
case240_wecc_sad	**(8) 0.45**	TO	(6) 2.44	TO	(20) 2.44	TO	(10) 2.41	TO
case9_bgm_nco	(6) 10.80	TO	(8) 10.79	TO	(10) 10.73	TO	**(6) 8.20**	TO
case9_na_cao_nco	(6) -6.87	TO	(8) -4.55	TO	(20) -0.07	TO	(8) -0.04	TO
case9_nb_cao_nco	(16) -4.87	TO	(6) -3.93	TO	(10) -0.64	TO	(8) -0.09	TO
case14_s_cao_nco	(6) 1.19	TO	(8) 0.89	TO	(16) 0.34	TO	(6) 0.05	TO
case39_1_bgm_nco	(10) 3.50	TO	**(8) 3.04**	TO	**(10) 2.79**	TO	**(8) 3.27**	TO

2.6.2 Analysis of "Hard" Instances

In Table 2.1 and 2.3, there are still five instances for which the best optimality gaps found by BT-Lambda, BT-Lambda-θ, and BT-Lambda-θ-α are larger than 1%. These problems are hard because the tightened bounds remain weak. Table 2.4 shows that there are a large number of θ_{ij} variables whose bounds allow positive and negative values (i.e., flow could be in ether direction). This is generally not the case for the other instances. We also notice that BT-Lambda-θ produces better optimality gaps than BT-Lambda-θ-α for all tested α values in 4 of 35 instances. In these cases, the heuristic incorrectly identifies variables whose partitioning is required to prove global optimality. Finally, AMP algorithm performed very well on three of six "nco" instances, which are hard for non-convex optimization. Though BT-QC$^{\text{conv}}$ exhibits large gaps, AMP finds near global optimum solutions within the prescribed time limits.

Table 2.4: Percentage of edges where $(\underline{\boldsymbol{\theta}} < 0) \wedge (\overline{\boldsymbol{\theta}} > 0)$ after BT.

Instances	% of edges
case240_wecc	77.6
case89_pegase_api	51.5
case118_ieee_api	32.4
case9_bgm_nco	44.4
case39_1_bgm_nco	45.7

2.7 Conclusions and Future Research

This chapter considers the ACOPF problem in polar form and develops efficient formulations and algorithms to solve it to global optimality. The key developments in this chapter are a) using state-of-the-art QC relaxations in combination with improved relaxations for trilinear functions based on a convex-hull representation, b) developing novel mathematical formulations for tight piecewise convex relaxations of trilinear and quadratic functions, and c) leveraging these tight formulations for global optimization using an adaptive multivariate partitioning approach in combination with bound tightening and effective heuristic branching strategies. Except for a few challenging instances, our methodologies help to close the best known gap for many hard instances. Future research will include testing our methods with other equivalent ACOPF formulations, investigating the exploitation of graph sparsitity, and exploring better branching and pruning strategies for piecewise formulations.

Chapter 3

Topology Reconfiguration for Power Systems under Geomagnetic Disturbances

In recent years, there have been increasing concerns about how geomagnetic disturbances (GMDs) impact electrical power systems. Geomagnetically-induced currents (GICs) can saturate transformers, induce hot-spot heating and increase reactive power losses. These effects can potentially cause catastrophic damage to transformers and severely impact the ability of a power system to deliver power. To address this problem, we develop a model of GIC impacts to power systems that includes 1) GIC thermal capacity of transformers as a function of normal Alternating Current (AC), and 2) reactive power losses as a function of GICs. We use this model to derive an optimization problem that protects power systems from GIC impacts through line switching, generator dispatch, and load shedding. We employ state-of-the-art convex relaxations of AC power flow equations and present a local branching algorithm that yields high-quality solutions quickly. We demonstrate the approach on a modified RTS96 system and show that line switching is an effective way to mitigate GIC impacts.

Nomenclature

Sets

$\mathcal{N}^a, \mathcal{N}^d, \mathcal{N}^o$	set of nodes in the AC and DC circuit, respectively, where $\mathcal{N}^o = \mathcal{N}^a \cap \mathcal{N}^d$
$\mathcal{N}^g \subseteq \mathcal{N}^a$	set of nodes with exactly one generator
$\mathcal{J} \subseteq \mathcal{N}^d$	set of substation neutrals
$\mathcal{E}^a, \mathcal{E}^d, \mathcal{E}$	set of edges in the AC and DC circuit, respectively, where $\mathcal{E} = \mathcal{E}^a \cup \mathcal{E}^d$
$\mathcal{E}^o \subseteq \mathcal{E}^a$	set of transmission lines
$\mathcal{E}^g \subseteq \mathcal{E}^a$	set of edges e_{ij} such that either i or $j \in N^g$
$\mathcal{E}^\tau \subseteq \mathcal{E}^a$	set of transformer edges
$\mathcal{E}^w \subseteq \mathcal{E}^d$	set of DC edges used to model transformer windings in the DC circuit
$\mathcal{E}^w_e \subseteq \mathcal{E}^d$	set of DC edges used to model the windings for transformer edges $e_{ij} \in \mathcal{E}^\tau$
$\mathcal{E}^+_i \subseteq \mathcal{E}$	set of outgoing edges connected to AC/DC node i
$\mathcal{E}^-_i \subseteq \mathcal{E}$	set of incoming edges connected to AC/DC node i
$\mathcal{E}_i$	set of all edges connected to AC/DC node i, where $\mathcal{E}_i = \mathcal{E}^+_i \cup \mathcal{E}^-_i$
$\mathcal{E}^\tau_i \subseteq \mathcal{E}^\tau$	set of AC edges used to compute d_i^{qloss} (as described later) for node i

Parameters

c_i^0, c_i^1, c_i^2	generation cost coefficients of generator $i \in N^g$

$\eta_e^0, \eta_e^1, \eta_e^2$	coefficients of the thermal limit curve of transformer line $e \in \mathcal{E}^\tau$
κ	cost of load shedding
a_m	admittance of the grounding line at bus $m \in \mathcal{I}$, 0 if bus $m \notin \mathcal{I}$
a_e	DC admittance of edge $e \in \mathcal{E}^d$
r_e, x_e	resistance and reactance of line $e \in \mathcal{E}^a$
g_e, b_e	conductance and susceptance of line $e \in \mathcal{E}^a$
g_i, b_i	shunt conductance and susceptance at bus $i \in N^a$
d_i^p, d_i^q	real and reactive power demand at bus $i \in N^a$
b_e^c	line charging susceptance of line $e \in \mathcal{E}^a$
s_e	apparent power limit on line $e \in \mathcal{E}^a$
$\overline{\theta}$	phase angle difference limit
θ^M	Big-M parameter given by $\lvert\mathcal{E}^a\rvert\overline{\theta}$
$\overline{I}_e^a$	AC current flow limit on line $e \in \mathcal{E}^a$
k_e	loss factor of transformer line $e \in \mathcal{E}^\tau$
$\underline{v}_i$, $\overline{v}_i$	AC voltage limits at bus $i \in N^a$
$\underline{gp}_i$, $\overline{gp}_i$	real power generation limits at generator $i \in G$
$\underline{gq}_i$, $\overline{gq}_i$	reactive power generation limits at generator $i \in G$
ϕ	the angle of the geo-electric field relative to east
ν_e^d	GMD induced voltage source on line $e \in \mathcal{E}^d$, 0 if $e \in \mathcal{E}^\tau$
L_N,L_E	the north and east components of the displacement of each transmission line, respectively
E_N,E_E	strength of the north and east geo-electric field, respectively

Binary Variables

z_e	1 if line $e \in \mathcal{E}^a$ is switched on; 0 otherwise

Continuous Variables

θ_i	phase angle at bus $i \in N^a$
v_i	AC voltage magnitude at bus $i \in N^a$
v_i^d	induced DC voltage magnitude at bus $i \in N^d$
l_e	AC magnitude squared on line $e \in \mathcal{E}^a$
I_e^d	GIC flow on transformer line $e \in \mathcal{E}^\tau$
$\widetilde{I}_e^a$	AC magnitude on line $e \in \mathcal{E}^a$
$\widetilde{I}_e^d$	the effective GIC on transformer line $e \in \mathcal{E}^\tau$
d_i^{qloss}	GIC-induced reactive power loss at bus $i \in N^a$
p_{ij}, q_{ij}	real and reactive power flow on line $e_{ij} \in \mathcal{E}^a$, as measured at node i
f_i^p, f_i^q	real and reactive power generated at bus $i \in N^a$
l_i^p, l_i^q	real and reactive power shed at bus $i \in N^a$

3.1 Introduction

Solar flares and coronal mass ejections drive geomagnetic disturbances (GMDs) that lead to changes in the Earth's magnetic field which, in turn, create geo-electric fields. These low-frequency geo-electric fields induce quasi-DC currents, also known as Geomagnetically-Induced Currents (GICs), in grounded sections of power system networks [10, 11, 105]. The GICs are superimposed on the usual alternating currents (AC) and bias the AC such that the maximum currents are increased. In many power system components, this bias is not a major concern; however, in transformers, this bias can lead to half-cycle saturation and

the loss of magnetic flux in regions outside of the transformer core. The energy stored in the stray flux increases the reactive power consumption of the transformer, which can affect system voltages. Stray flux also drives eddy currents that can cause excessive transformer heating, leading to reduced transformer life or, potentially, immediate damage [7].

The potential impacts of GMDs to transformers in the bulk electric power system have led the United States government to increase the understanding of and mitigate the impacts of such events [8], [40]. To mitigate the potential risks introduced by GICs to power systems, the electric power industry has actively improved GIC modeling and GIC monitoring [6, 25, 38, 58, 89, 94]. These models have been used to conduct risk analyses [88,89] that investigate the sensitivity of transformer reactive power losses due to GICs and concluded that risk and risk mitigation warrants further study.

One focus in the recent literature has been on mitigating the effect of GICs on transformer reactive power consumption and subsequent drops in system voltages and potential voltage collapse. One approach to mitigation is the installation of DC-current blocking devices to keep GICs from entering through transformer neutrals [20]; however, these devices are expensive, with costs for a single unit close to \$500K [66, 71, 123]. In an attempt to minimize the projected cost of mitigation, optimization-based methods have been developed to guide the siting of these blocking devices. Instead of performing a full power systems analysis that includes the AC, GICs and full AC power flow equations, previous study has primarily focused on minimizing induced reactive losses independent of normal AC currents. The intuition of these surrogate models is that small amounts of reactive losses imply small voltage impacts and, presumably, a secure power system. Beyond voltage effects, the literature on risk mitigation associated with transformer heating is relatively sparse. Existing studies focus on assessing transformer susceptibility to GIC effects [44] and formulating the thermal response of transformer cores to different levels of GMDs [76]. However, this approach was strictly a screening study and did not recommend methods for mitigation in practice.

While this earlier research is a very important start, it leaves a number of open

questions. First, the installation of blocking devices is very expensive and its associated cost may pose a barrier to adoption. Instead, we focus on developing a GIC-aware optimal power flow (OPF) model that uses existing controls such as generator dispatch, load shedding, and line switching to mitigate the risks of GIC impacts. Second, we incorporate the AC physics of power flow into the GIC-aware OPF because these physics play an important role in the impacts associated with GICs. For example, while minimizing reactive losses may imply small voltage problems across the whole system, these models focus on total losses and can miss relatively large voltage problems in a small part of a system. More importantly, models of hot-spot thermal heating inherently depend on both GICs and AC.

The setting considered in this chapter is very challenging. It combines transformer reactive losses, transformer heating, and full AC power flow into an optimization-based operational mitigation setting with line switching. By itself, optimal transmission line switching (OTS) with AC power flow physics is a mathematically challenging problem that includes nonlinearities, non-convexities and discrete variables. Existing solution methodologies designed for OTS heavily rely on tight convex relaxations and advanced discrete optimization techniques. Recently, various convex relaxations and disjunctive representations have been developed, such as second-order-conic (SOC) relaxations [64], quadratically constrained (QC) relaxations [56] and Semi-definite programming relaxations [13]. In the context of transmission expansion planning applications, the QC relaxations have been shown to be effective [81, 84]. Despite these recent advances in optimization methods for OTS, global methods still cannot scale to solve systems with 500 nodes.

The main contributions of this chapter are the formulation and initial algorithmic solution approaches to an operational decision support tool that incorporates:

1. A model of transformer heating as a response to AC and GIC-induced DC,

2. A realistic, coupled model of convex, relaxed AC power flows with GIC effects for different transformer types and a heuristic method that obtains high-quality solutions quickly, and

3. An optimization problem that protects the system from reactive losses and thermal heating induced by GICs.

3.2 GIC modeling and ACOTS formulation

3.2.1 GIC Modeling

ν_e^d calculation The computation of transformer hot-spot heating and GIC-induced reactive power losses depends on the induced voltage sources (ν_e^d) on each power line $e \in \mathcal{E}^d$ in the network, which itself depends on the strength and direction of the geo-electric field (i.e., the electric field at the surface of the earth) associated with the GMD. These relationships are modeled in Eq.(3.1).

$$\nu_e^d = \oint \vec{E}_e \cdot d\vec{l}_e \qquad \forall e \in \mathcal{E}^d, \tag{3.1}$$

where, $\vec{E}_e$ is the geo-electric field at the location of transmission line $e \in \mathcal{E}^d$, and $d\vec{l}_e$ is the incremental line segment length, including direction [6]. In practice, the actual geo-electric field varies with time and geographical locations. Using a common assumption that the geo-electric field is uniformly distributed in the geographical area of a transmission grid [6, 58, 123] (i.e., $\vec{E}_e = \vec{E},\ \forall e \in \mathcal{E}^d$), ν_e^d can be reformulated in the following form:

$$\nu_e^d = \vec{E} \cdot \vec{L}_e = E_N L_e^N + E_E L_e^E = |\vec{E}|\Big(\sin(\phi)L_N + \cos(\phi)L_E\Big) \qquad \forall e \in \mathcal{E}^d, \tag{3.2}$$

where $\vec{L}_e$ denotes the length of line e with direction. L_N, L_E, E_N, E_E and ϕ are as described in the nomenclature (see Appendix I of [6]). Given that transformer edges (windings) are sufficient short, thus the induced voltage sources for transformers are negligible, i.e., $\nu_e^d = 0 \quad e \in \mathcal{E}^w$.

Transformer Modeling The two most common transformers in electrical transmission systems subject to GICs are network transformers and generator step-up (GSU) transformers. Network transformers are generally located relatively far from generators and transform voltage between different sections of the transmission system. In contrast, GSUs connect

the output terminals of generators to the transmission network. Many IEEE transmission reliability test networks explicitly model network transformers, but generally do not model GSUs. However, GSUs and the neutral leg ground points they provide are critical when modeling GICs and methods to mitigate the impact of GICs.

In this chapter, we modify the IEEE RTS test network by adding a GSU transformer between each generator and its injection bus (see Figure 3.1(a)). Consistent with common engineering practice, we assume that each GSU is grounded on its high voltage side that connects to the transmission network. We also model the switching of the circuit breaker between the high side of the GSU and the transmission network using a binary variable that allows the GSU to be isolated from the network and the quasi-DC GICs to protect the GSU. This switching is performed if the generator output is zero. Although the IEEE test networks include network transformers, transformer type and grounding data are typically not provided. We consider two types of network transformers: (1) Gwye-Gwye transformers and (2) auto-transformers. For a Gwye-Gwye transformer, we assume that its high-voltage (HV) and low-voltage (LV) sides are both connected to the neutral ground, while each auto-transformer has a single neutral node that is located on the common side.

Figure 3.1 includes examples of both GSU and network transformer modeling. Figure 3.1(a) shows a five-bus section of the transmission system with one auto-transformer ($\mathcal{T}_{jk}$), one Gwye-Gwye transformer ($\mathcal{T}_{ks}$), and two GSU transformers ($\mathcal{T}_i^b$, $\mathcal{T}_i^c$) independently connecting two generators (G_i^b, G_i^c) to the same injection bus i. Figure 3.1(b) presents a simplified AC equivalent network of this five-bus example. In the figure, bus b and c model output terminals of generation G_i^b and G_i^c, respectively. Each GSU transformer $\mathcal{T}_i^b$ ($\mathcal{T}_i^c$) is reduced to a (single) series impedance ib (ic) with a circuit breaker. Similarly, each network transformer $\mathcal{T}_{jk}$ ($\mathcal{T}_{ks}$) is reduced to a (single) series impedance jk (ks) with a circuit breaker. Under this transformation, the number of buses and lines in the AC network grow to $|\mathcal{N}^o| + |\mathcal{N}^g|$ and $|\mathcal{E}^o| + |\mathcal{N}^g|$, respectively, where $|\mathcal{N}^o|$ and $|\mathcal{E}^o|$ represent the original set of buses and edges in the network. Figure 3.1(c) shows an equivalent single-phase DC circuit of the example system in nodal form. In this figure, n^A, n^B and n^C model the neutral points

of substation A, B, and C, respectively. Parameters a_m^A, a_m^B and a_m^C denote the grounding admittance of substation A, B, and C, respectively. For GSU transformer $\mathcal{T}_i^b$ ($\mathcal{T}_i^c$), the HV bus and HV primary winding are modeled by node i and edge (i, n^A), respectively, where a_{ib} (a_{ic}) represents the admittance of the HV winding. For auto-transformer $\mathcal{T}_{jk}$, the HV and LV buses are modeled as nodes j and k, respectively. Edges (j, k) and (k, n^B) model its series and common windings whose admittance are a_{jk} and a_{kn}, respectively. Similarly, buses k and s represent the HV and LV buses of Gwye-Gwye transformer $\mathcal{T}_{ks}$, respectively. The HV and LV windings of $\mathcal{T}_{ks}$ are modeled by edge (k, n^C) and (c, n^C) with admittance a_{kn} and a_{ns}, respectively. Meanwhile, each edge in the DC circuit can be linked to one and only one edge in the AC circuit (one-to-one). For example, transmission line (i, j) in the DC circuit is associated with the single line (i, j) in the AC circuit. Further, DC edges (j, k) and (k, n^B) are associated with the same transformer edge (j, k) in the AC circuit (many-to-one).

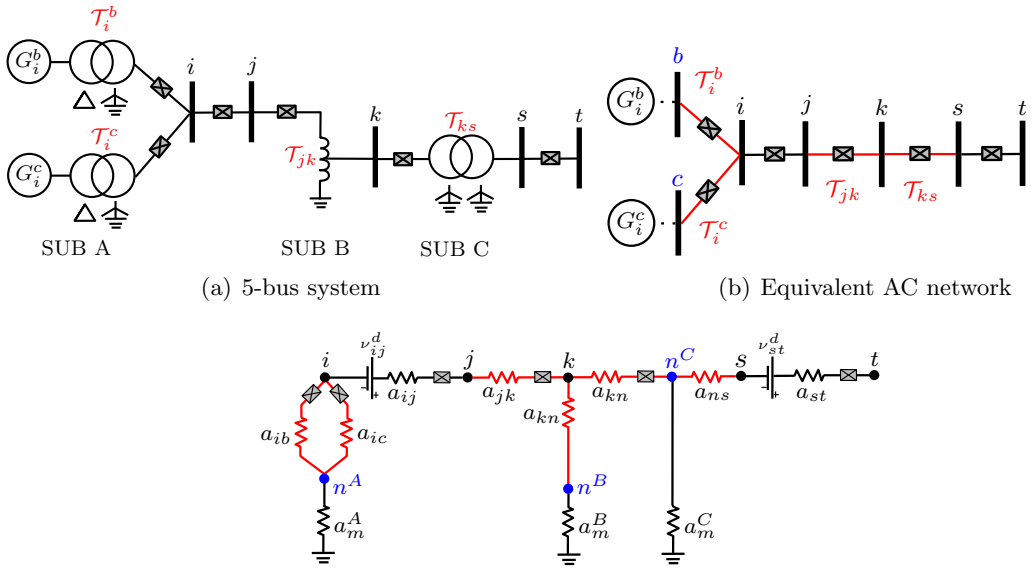

(a) 5-bus system

(b) Equivalent AC network

(c) Equivalent DC network

Figure 3.1: Schematic of GSU and network transformer modeling. In Figure 3.1(b), red font represents transformer lines in the AC circuit, i.e., $\mathcal{E}^\tau \subseteq \mathcal{E}^a$. In Figure 3.1(c), blue font denotes neutral buses of substations (i.e., $i \in \mathcal{I}$) and red font represents transformer windings in the DC circuit (i.e., $\mathcal{E}^w \subseteq \mathcal{E}^d$), respectively.

Since GICs in the transformer HV and LV windings are different, it is important

to calculate the effective GICs for each transformer type to measure transformer hot-spot heating and GIC-induced reactive power consumption. To illustrate our effective GIC formulation, we extract the DC representation of each transformer type in Figure 3.2. For notation brevity, we define subscripts h and l as the HV and LV sides of the GSU/Gwye-Gwye transformer, respectively, while subscripts s and c denote the series and common sides of the auto-transformer, respectively. Let N_x and I_x^d then represent the number of turns and GICs in the transformer winding x, respectively, and let $\Theta(\cdot)$ denote a linear function of I_x^d. For the grounded GSU transformer, its DC-equivalent circuit is shown in Figure 3.2(a). The effective GICs (denoted as $\widetilde{I}^d$) only depend on GICs in the HV primary winding, i.e.,

$$\widetilde{I}^d = \left|\Theta(I_h^d)\right| = \left|I_h^d\right| \tag{3.3}$$

For an auto-transformer, as shown in Figure 3.2(b), the effective GICs are determined by GIC flows in the series and common windings, such that:

$$\widetilde{I}^d = \left|\Theta(I_s^d) + \Theta(I_c^d)\right| = \left|\frac{(\alpha-1)I_s^d + I_c^d}{\alpha}\right| \tag{3.4}$$

where turns ratio $\alpha = \frac{N_s+N_c}{N_c}$. Similarly, the effective GICs for a Gwye-Gwye transformer (Figure 3.2(c)) captures GICs in the both HV and LV sides, i.e.,

$$\widetilde{I}^d = \left|\Theta(I_h^d) + \Theta(I_l^d)\right| = \left|\frac{\alpha I_h^d + I_l^d}{\alpha}\right| \tag{3.5}$$

where transformer turns ratio $\alpha = \frac{N_h}{N_l}$. Further, for three-winding transformers: delta-delta, delta-wye, wye-delta, and wye-wye, we assume their windings are ungrounded. Hence, their associated effective GICs are zero due to the fact that such ungrounded transformers do not provide a path for GIC flow [6].

GIC-Effects During GMDs, the quasi-DC GICs may flow through transformers with grounded neutral legs. This quasi-DC current combines with the normal operating AC current creating half-cycle saturation and loss of magnetic flux from the transformer core,

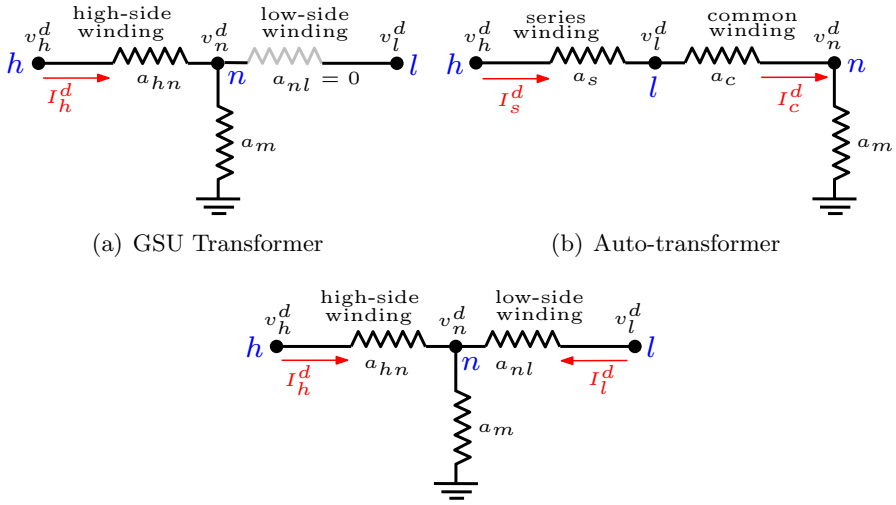

(a) GSU Transformer

(b) Auto-transformer

(c) Gwye-Gwye Transformer

Figure 3.2: DC equivalent circuits for different types of transformers. h, l, and n (blue font) represent high-side bus, low-side bus, and neutral bus, respectively.

which lead to several undesirable effects. The two effects that we consider are (1) eddy current-driven transformer heating and (2) excess reactive power consumption caused by the excess magnetic energy stored in the stray magnetic flux. Both of these effects are challenging to model from first principles, and even if such models existed, they would be too complex to include in the OTS formulation. Instead, we use a combination of manufacturer test, specification data, and simplified models to calculate GIC effects.

For eddy current-driven transformer heating, we use GIC capability curves (see Fig. 3.3) that may be based on either manufacturer acceptance test data or on electromagnetic and thermal modeling of the transformer design. These curves provide an upper bound on a feasible operating range in the space of AC loading and GICs. This upper bound is also a function of the duration of the combined AC and GIC loading (typically given for 30 minute and 2 minute durations). The sampled points (blue) in Fig. 3.3 are sampled from a transformer manufacturer's 2-minute duration curve [1]. Over a reasonable operating range, these points are well represented by the best-fit quadratic (red) curve with the feasible operating region lying below and to the left of the curve.

Excess reactive power losses due to GICs has been studied in the literature [71,88,89,

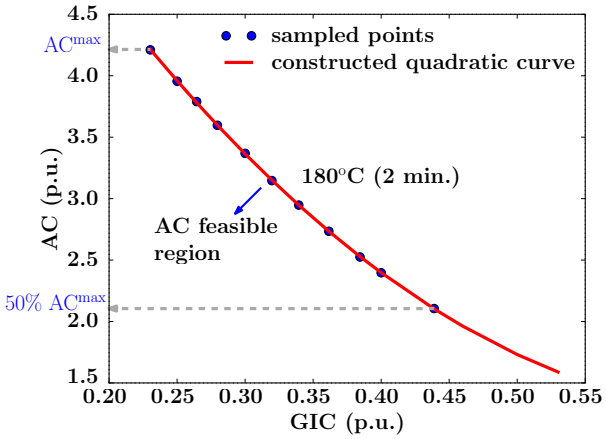

Figure 3.3: Fitted curve for thermal GIC capability of a transformer. Here, we used 180° as the maximum allowed temperature of transformers for short-term (2 minutes) peak GIC pulses and assumed that a transformer cannot be loaded to greater than 100% of its MVA limit. The figure shows the coefficients of the constructed quadratic function (curve), η_e^0, η_e^1 and η_e^2, fitted to the collected 11 (blue) points of the GIC thermal capacity measurements. The feasible region of the transformer load current is the area under the curve and is expressed as constraint (3.6x).

123]. We adopt the simplified model in [88] which is shown in Eq.(5). These reactive losses create voltage sags that can adversely impact system operation. The previous work has focused on minimizing these losses to improve system safety. In this chapter, we explicitly model the AC power equations (voltage magnitudes) so that we can enforce voltage limits directly.

3.2.2 ACOTS with GIC constraints

A complete ACOTS model with topology reconfiguration that accounts for GIC-induced transformer thermal heating and transformer reactive power heating is formulated below.

$$\mathcal{P}^o := \min \sum_{i\in\mathcal{N}^g, e\in\mathcal{E}_i} c_i^2 (f_i^p)^2 + c_i^1 f_i^p + z_e(c_i^0) + \sum_{i\in\mathcal{N}^a} \kappa(l_i^p + l_i^q) \tag{3.6a}$$

s.t. **AC power flow equations**

$$\sum_{e_{ij}\in\mathcal{E}_i^+} p_{ij} + \sum_{e_{ji}\in\mathcal{E}_i^-} p_{ij} = f_i^p + l_i^p - d_i^p - v_i^2 g_i \quad \forall i \in \mathcal{N}^a \tag{3.6b}$$

$$\sum_{e_{ij}\in\mathcal{E}_i^+} q_{ij} + \sum_{e_{ji}\in\mathcal{E}_i^-} q_{ij} = f_i^q + l_i^q - d_i^q + v_i^2 b_i - d_i^{qloss} \quad \forall i \in N^a \tag{3.6c}$$

$$p_{ij} = z_e\big(g_e v_i^2 - v_i v_j g_e \cos(\theta_i - \theta_j) - v_i v_j b_e \sin(\theta_i - \theta_j)\big) \quad \forall e_{ij} \in \mathcal{E}^a \backslash \mathcal{E}^g \tag{3.6d}$$

$$q_{ij} = z_e\big(-(b_e + \frac{b_e^c}{2})v_i^2 + v_i v_j b_e \cos(\theta_i - \theta_j) - v_i v_j g_e \sin(\theta_i - \theta_j)\big) \quad \forall e_{ij} \in \mathcal{E}^a \backslash \mathcal{E}^g \tag{3.6e}$$

$$p_{ji} = z_e\big(g_e v_j^2 - v_i v_j g_e \cos(\theta_j - \theta_i) - v_i v_j b_e \sin(\theta_j - \theta_i)\big) \quad \forall e_{ij} \in \mathcal{E}^a \backslash \mathcal{E}^g \tag{3.6f}$$

$$q_{ji} = z_e\big(-(b_e + \frac{b_e^c}{2})v_j^2 + v_i v_j b_e \cos(\theta_j - \theta_i) - v_i v_j g_e \sin(\theta_j - \theta_i)\big) \quad \forall e_{ij} \in \mathcal{E}^a \backslash \mathcal{E}^g \tag{3.6g}$$

$$p_{ij} + p_{ji} = z_e r_e\big(l_e + b_e^c q_{ij} + (\frac{b_e^c}{2})^2 v_i^2\big) \quad \forall e_{ij} \in \mathcal{E}^a \backslash \mathcal{E}^g \tag{3.6h}$$

$$q_{ij} + q_{ji} = z_e\big(x_e(l_e + b_e^c q_{ij} + (\frac{b_e^c}{2})^2 v_i^2) - \frac{b_e^c}{2}(v_i^2 + v_j^2)\big) \quad \forall e_{ij} \in \mathcal{E}^a \backslash \mathcal{E}^g \tag{3.6i}$$

$$p_{ij} + p_{ji} = 0,\ q_{ij} + q_{ji} = 0 \quad \forall e_{ij} \in \mathcal{E}^g \tag{3.6j}$$

$$p_{ij}^2 + q_{ij}^2 = l_e v_i^2 \quad \forall e_{ij} \in \mathcal{E}^a \tag{3.6k}$$

$$l_e = (\widetilde{I}_e^a)^2 \quad \forall e \in \mathcal{E}^a \tag{3.6l}$$

Operational limit constraints

$$p_{ij}^2 + q_{ij}^2 \leqslant z_e s_e^2, \quad p_{ji}^2 + q_{ji}^2 \leqslant z_e s_e^2 \quad \forall e_{ij} \in \mathcal{E}^a \tag{3.6m}$$

$$0 \leqslant \widetilde{I}_e^a \leqslant z_e \overline{I}_e^a \quad \forall e \in \mathcal{E}^a \tag{3.6n}$$

$$\underline{v}_i \leqslant v_i \leqslant \overline{v}_i \quad \forall i \in \mathcal{N}^a \tag{3.6o}$$

$$|\theta_i - \theta_j| \leqslant z_e \overline{\theta} + (1 - z_e)\theta^M \quad \forall e_{ij} \in \mathcal{E}^a \backslash \mathcal{E}^g \tag{3.6p}$$

$$z_e \underline{gp}_i \leqslant f_i^p \leqslant z_e \overline{gp}_i \quad \forall i \in \mathcal{N}^g,\ e \in \mathcal{E}_i \tag{3.6q}$$

$$z_e \underline{gq}_i \leqslant f_i^q \leqslant z_e \overline{gq}_i \quad \forall i \in \mathcal{N}^g,\ e \in \mathcal{E}_i \tag{3.6r}$$

GIC effects on transformers

$$\sum_{e_{nm} \in \mathcal{E}_m^-} z_{\overrightarrow{e}} a_e (v_n^d + \nu_e^d - v_m^d) - \sum_{e_{mn} \in \mathcal{E}_m^+} z_{\overrightarrow{e}} a_e (v_m^d + \nu_e^d - v_n^d) = a_m V_m^d \quad \forall m \in \mathcal{N}^d \tag{3.6s}$$

$$I_e^d = z_{\overrightarrow{e}} a_e (v_m^d - v_n^d) \quad \forall e_{mn} \in \mathcal{E}^w \tag{3.6t}$$

$$\widetilde{I}_e^d \geqslant \sum_{\hat{e}_{ij} \in \mathcal{E}_e^w} \Theta(I_{\hat{e}}^d), \quad \widetilde{I}_e^d \geqslant -\sum_{\hat{e}_{ij} \in \mathcal{E}_e^w} \Theta(I_{\hat{e}}^d) \quad \forall e \in \mathcal{E}^\tau \tag{3.6u}$$

$$0 \leqslant \widetilde{I}_e^d \leqslant \max_{\forall \hat{e} \in \mathcal{E}^a} 2\overline{I}_{\hat{e}}^a \quad \forall e \in \mathcal{E}^\tau \tag{3.6v}$$

$$d_i^{qloss} = \sum_{e \in \mathcal{E}_i^\tau} k_e v_i \widetilde{I}_e^d \quad \forall i \in \mathcal{N}^a \tag{3.6w}$$

$$\widetilde{I}_e^a \leqslant \eta_e^0 + \eta_e^1 \widetilde{I}_e^d + \eta_e^2 (\widetilde{I}_e^d)^2 \quad \forall e \in \mathcal{E}^\tau \tag{3.6x}$$

$$z_e \in \{0, 1\} \quad \forall e \in \mathcal{E}^a \tag{3.6y}$$

The objective function (3.6a) minimizes total generator dispatch costs and load

shedding costs. Constraints (3.6b) – (3.6r) describe system constraints for the buses and branches in the AC circuit. Constraints (3.6b) and (3.6c) represent the nodal real and reactive power balance, including the increased reactive power losses (demand) due to GICs. Constraints (3.6d) through (3.6g) model the AC power flow on each transmission line with on-off variables z_e. The flow on any line is forced to zero if the line is switched off. Constraints (3.6h) through (3.6j) represent power loss equations associated with AC power flow. In constraint (3.6j), *fictitious* lines between output terminals of generators and their injection buses are modeled as transportation edges (i.e., $|p_{ij}| = |-p_{ji}| = f_i^p, |q_{ij}| = |-q_{ji}| = f_i^q \ \ \forall e_{ij} \in \mathcal{E}^g$). Non-convex constraint (3.6k) evaluates current magnitude l_{ij}, an auxiliary variable introduced to bound the squared AC current flow magnitude in constraint (3.6l). Constraints (3.6m) through (3.6r) describe the operational limits of the grid; constraint (3.6m) models operational thermal limits of lines in both directions. Constraint (3.6o) limits the voltage magnitude at buses. Constraint (3.6p) applies appropriate bounds on phase angle difference between two buses when the line exists. Constraints (3.6q) and (3.6r) model the availability and capacity of power generation. A generator is offline if its line is switched off.

The DC circuit and the effects associated with the GMD are formulated in constraints (3.6s)-(3.6x). Recall that we link an edge, $e \in \mathcal{E}^d$ in the DC circuit to an edge in the AC circuit with $\overrightarrow{e}$. The HV primary side of GSU transformer $e_{ij} \in \mathcal{E}^\tau$ is modeled by introducing a node and an edge in the DC circuit (e.g., node n^A and edge (i, n^A) in Fig. 3.1(c)). Similarly, the common side of auto-transformer $e_{ij} \in \mathcal{E}^\tau$ is modeled in the DC circuit by introducing additional nodes and edges (e.g., node n^B and edge (k, n^B) in Fig. 3.1(c)). For Gwye-Gwye network transformer $e_{ij} \in \mathcal{E}^\tau$, the HV and LV sides are modeled by two new edges that are introduced by adding one neutral node between bus i and j in the DC circuit (e.g., node n^C and two edges (k, n^c), (s, n^c) in Fig. 3.1(c)). By using these notations, constraints (3.6s) and (3.6t) calculate the GIC flow on each DC line by applying Kirchhoff's current law. The GIC on a line is determined by the induced voltage source and the quasi-DC voltage difference between two buses [6]. GIC flow is forced to 0 by $z_{\overrightarrow{e}}$

when line $\overrightarrow{e}$ is switched off. Since for each $e \in \mathcal{E}^d$ the value of I_e^d can be negative, decision variables $\widetilde{I}_e^d$ for each transformer $e \in \mathcal{E}^\tau$ are introduced to model the effective values of GICs. Instead of introducing additional discrete variables, constraint set (3.6u) is used to model and relax the absolute value of $\sum_{\widehat{e}_{ij} \in \mathcal{E}_e^w} \Theta(I_{\widehat{e}}^d)$ where $\Theta(\cdot)$ is a linear function of GICs in transformer windings defined in the form of (3.3)–(3.5). Constraint (3.6v) denotes the maximum allowed value of the effective GICs in transformers. We assume this limit is twice the upper bound of AC flows in the network. Constraint (3.6w) computes the reactive power load due to transformer saturation [11, 89, 122, 123] by using the effective GICs for each transformer type. Constraint (3.6x) guarantees that the hot-spot temperature of transformers due to the combination of AC and GICs is below the thermal limits for peak GIC. The couplings between AC power flows and GICs occur in constraints (3.6c), (3.6x), and (3.6w).

3.2.3 Convex Relaxations

The ACOTS with GIC constraints is a mixed-integer, non-convex optimization problem that is generally computationally difficult to solve. We adopt the convex relaxations developed by [56]. We now discuss the key features of the relaxations extended to the problem with GICs.

Handling bilinear terms Given any two variables x_i, $x_j \in \mathbb{R}$, the McCormick relaxation is used to linearize the bilinear product $x_i x_j$ by introducing a new variable $\widehat{x}_{ij} \in \langle x_i, x_j \rangle^{MC}$. The feasible region of $\widehat{x}_{ij}$ is defined by inequalities (3.7). Note that the MC relaxation is exact if one variable is binary.

$$\widehat{x}_{ij} \geqslant \underline{x}_i x_j + \underline{x}_j x_i - \underline{x}_i \, \underline{x}_j \tag{3.7a}$$

$$\widehat{x}_{ij} \geqslant \overline{x}_i x_j + \overline{x}_j x_i - \overline{x}_i \, \overline{x}_j \tag{3.7b}$$

$$\widehat{x}_{ij} \leqslant \underline{x}_i x_j + \overline{x}_j x_i - \underline{x}_i \, \overline{x}_j \tag{3.7c}$$

$$\widehat{x}_{ij} \leqslant \overline{x}_i x_j + \underline{x}_j x_i - \overline{x}_i \, \underline{x}_j \tag{3.7d}$$

$$\underline{x}_i \leqslant x_i \leqslant \overline{x}_i, \ \underline{x}_j \leqslant x_j \leqslant \overline{x}_j \tag{3.7e}$$

Quadratic terms Given a variable $x_i \in \mathbb{R}$, a second-order conic relaxation can be applied to convexify the quadratic term x_i^2 by introducing a new variable $\widehat{x}_i \in \langle x_i \rangle^{MC-q}$, as defined in equation (3.8).

$$\widehat{x}_i \geqslant x_i^2 \tag{3.8a}$$

$$\widehat{x}_i \leqslant (\overline{x}_i + \underline{x}_i)x_i - \overline{x}_i\underline{x}_i \tag{3.8b}$$

$$\underline{x}_i \leqslant x_i \leqslant \overline{x}_i \tag{3.8c}$$

On-off trigonometric terms In constraints (3.6d), (3.6e), (3.6f) and (3.6g), if the line e_{ij} is switched off, Hijaz *et al.* [56] suggests the following procedure to deactivate the associated trigonometric terms: Given the phase angle difference variable $\theta_{ij} = \theta_i - \theta_j$ and on-off variable $z_e \in \{0, 1\}$, a disjunctive quadratic relaxation is used to convexify the nonlinear function $z_e \cos(\theta_{ij})$ by introducing a new variable $\widehat{cs}_{ij} \in \langle z_e cos(\theta_{ij}) \rangle^R$, as formulated in (3.9).

$$\widehat{cs}_{ij} \leqslant z_e - \frac{1 - \cos(\overline{\theta})}{(\overline{\theta})^2}(\theta_{ij}^2 + (z_e - 1)(\theta^u)^2) \tag{3.9a}$$

$$z_e \cos(\overline{\theta}) \leqslant \widehat{cs}_{ij} \leqslant z_e \tag{3.9b}$$

Similarly, for $z_e sin(\theta_{ij})$, a disjunctive polyhedral relaxation is applied by introducing a new variable $\widehat{s}_{ij} \in \langle z_e sin(\theta_{ij}) \rangle^R$, as described in equation (3.10).

$$\widehat{s}_{ij} \leqslant \cos(\bar{\theta}/2)\theta_{ij} + z_e(\sin(\bar{\theta}/2) - \bar{\theta}/2\cos(\bar{\theta}/2)) + (1 - z_e)(\cos(\bar{\theta}/2)\theta^M + 1) \tag{3.10a}$$

$$\widehat{s}_{ij} \geqslant \cos(\bar{\theta}/2)\theta_{ij} - z_e(\sin(\bar{\theta}/2) - \bar{\theta}/2\cos(\bar{\theta}/2)) - (1 - z_e)(\cos(\bar{\theta}/2)\theta^M + 1) \tag{3.10b}$$

$$z_e \sin(-\overline{\theta}) \leqslant \widehat{s}_{ij} \leqslant z_e \sin(\overline{\theta}) \tag{3.10c}$$

Based on the above relaxations, we replace the non-convex constraints in (3.6b)–(3.6i) with

equations (3.11):

$$\sum_{e_{ij}\in\mathcal{E}_i^+} p_{ij} + \sum_{e_{ji}\in\mathcal{E}_i^-} p_{ij} = f_i^p + l_i^p - d_i^p - \widehat{v}_i g_i \qquad \forall i \in \mathcal{N}^a \qquad (3.11a)$$

$$\sum_{e_{ij}\in\mathcal{E}_i^+} q_{ij} + \sum_{e_{ji}\in\mathcal{E}_i^-} q_{ij} = f_i^q + l_i^q - d_i^q + \widehat{v}_i^2 b_i - d_i^{qloss} \qquad \forall i \in N^a \qquad (3.11b)$$

$$p_{ij} = g_e\widehat{zv}_{ij} - g_e\widehat{wc}_{ij} - b_e\widehat{ws}_{ij} \qquad \forall e_{ij} \in \mathcal{E}^a\backslash\mathcal{E}^g \qquad (3.11c)$$

$$q_{ij} = -(b_e + \frac{b_e^c}{2})\widehat{zv}_{ij} + b_e\widehat{wc}_{ij} - g_{ij}\widehat{ws}_{ij} \qquad \forall e_{ij} \in \mathcal{E}^a\backslash\mathcal{E}^g \qquad (3.11d)$$

$$p_{ji} = g_e\widehat{zv}_{ji} - g_e\widehat{wc}_{ij} + b_e\widehat{ws}_{ij} \qquad \forall e_{ij} \in \mathcal{E}^a\backslash\mathcal{E}^g \qquad (3.11e)$$

$$q_{ji} = (-(b_e + \frac{b_e^c}{2})\widehat{zv}_{ji} + b_e\widehat{wc}_{ij} + g_e\widehat{ws}_{ij} \qquad \forall e_{ij} \in \mathcal{E}^a\backslash\mathcal{E}^g \qquad (3.11f)$$

$$p_{ij} + p_{ji} = r_e\big(l_e + b_e^c q_{ij} + (\frac{b_e^c}{2})^2\widehat{zv}_{ij}\big) \qquad \forall e_{ij} \in \mathcal{E}^a\backslash\mathcal{E}^g \qquad (3.11g)$$

$$q_{ij} + q_{ji} = x_e(l_e + b_e^c q_{ij} + (\frac{b_e^c}{2})^2\widehat{zv}_{ij}) - \frac{b_e^c}{2}(\widehat{zv}_{ij} + \widehat{zv}_{ji}) \qquad \forall e_{ij} \in \mathcal{E}^a\backslash\mathcal{E}^g \qquad (3.11h)$$

where, the new variables $\widehat{zv}_{ij}$, $\widehat{wc}_{ij}$ and $\widehat{ws}_{ij}$, admit feasible regions as follows:

$$\widehat{cs}_{ij} \in \langle z_e cos(\theta_{ij})\rangle^R, \quad \widehat{s}_{ij} \in \langle z_e sin(\theta_{ij})\rangle^R, \qquad (3.12a)$$

$$\widehat{v}_i \in \langle v_i\rangle^{MC-q}, \quad \widehat{zv}_{ij} \in \langle z_{ij}, \widehat{v}_i\rangle^{MC}, \quad \widehat{zv}_{ji} \in \langle z_{ij}, \widehat{v}_j\rangle^{MC}, \qquad (3.12b)$$

$$\widehat{w}_{ij} \in \langle v_i, v_j\rangle^{MC}, \qquad (3.12c)$$

$$\widehat{wc}_{ij} \in \langle \widehat{w}_{ij}, \widehat{cs}_{ij}\rangle^{MC}, \quad \widehat{ws}_{ij} \in \langle \widehat{w}_{ij}, \widehat{s}_{ij}\rangle^{MC} \qquad (3.12d)$$

Other non-convex constraints Further, non-convex constraints (3.6k) and (3.6l) are relaxed to a convex, rotated second-order conic constraint by using the introduced lifted variable $\widehat{v}_i$ (for (3.6k)) as follows:

$$p_{ij}^2 + q_{ij}^2 \leqslant l_e\widehat{v}_i \qquad \forall e_{ij} \in \mathcal{E}^a, \qquad (3.13a)$$

$$l_e \geqslant (\widetilde{I}_e^a)^2, \; l_e \leqslant (\overline{I}_e^a)\widetilde{I}_e^a \qquad \forall e \in \mathcal{E}^a \qquad (3.13b)$$

Convex relaxations of the reformulated thermal heating limit constraint (3.6x) and excess

reactive power losses equation (3.6w) are stated here in equations (3.14):

$$\widetilde{I}_e^a \leqslant \eta_e^0 + \eta_e^1 \widetilde{I}_e^d + \eta_e^2 \widehat{I}_e^d \qquad \forall e \in \mathcal{E}^\tau \tag{3.14a}$$

$$d_i^{qloss} = \sum_{e \in \mathcal{E}_i^\tau} k_e \widehat{u}_{ie}^d \qquad \forall i \in N^a \tag{3.14b}$$

$$\widehat{I}_e^d \in \langle \widetilde{I}_e^d \rangle^{MC-q} \qquad \forall e \in \mathcal{E}^\tau \tag{3.14c}$$

$$\widehat{u}_{ie}^d \in \langle v_i, \widetilde{I}_e^d \rangle^{MC} \qquad \forall i \in \mathcal{E}^a, \quad \forall e \in \mathcal{E}_i^\tau \tag{3.14d}$$

Convex relaxations of the GIC injection constraints (3.6s) and (3.6t) are described in equation (3.15).

$$\sum_{e \in \mathcal{E}_m^+} z_{\overrightarrow{e}} a_e \nu_e^d - \sum_{e \in \mathcal{E}_m^-} z_{\overrightarrow{e}} a_e \nu_e^d = -a_m v_m^d - \sum_{e \in \mathcal{E}_m^+} a_e \widehat{zv}_e^d + \sum_{e \in \mathcal{E}_m^-} a_e \widehat{zv}_e^d \qquad \forall m \in N^d \tag{3.15a}$$

$$I_e^d = a_e \widehat{zv}_e^d \qquad \forall e \in \mathcal{E}^w \tag{3.15b}$$

$$\widehat{zv}_e^d \in \langle z_{\overrightarrow{e}}, (v_m^d - v_n^d) \rangle^{MC} \qquad \forall e_{mn} \in \mathcal{E}^d \tag{3.15c}$$

In summary, the convexified problem is formulated as:

$$\mathcal{P}^{\mathcal{C}} := \left\{ \min (3.6a) : (3.11) - (3.15); (3.6j) - (3.6m); (3.6u) - (3.6v); \boldsymbol{z} \in \{0,1\}^{|\mathcal{E}^a|} \right\} \tag{3.16}$$

3.3 A Local Branching Search Algorithm

In the literature, heuristics have been widely applied to the OTS problem to efficiently select which line(s) to remove from the network by line ranking [43, 115] or by imposing a constraint on the number of lines that may be off in a solution [42]. For example, Soroush and Fuller [102] propose a new heuristic to rank lines for removal based on solutions from the economic dispatch problem and its corresponding optimal dual variables. The switching solutions found by these heuristics have shown that significant reductions in required computing times is possible.

We now present a heuristic that exploits a local branching strategy [41] in con-

junction with the above convex relaxations to quickly find high-quality solutions to our problem. First, given a feasible topology decision $\boldsymbol{z}^0$, we define $\mathbb{I}$ and $\mathbb{O}$ as sets of edges e_{ij}: $\mathbb{I} := \{e_{ij} \in \mathcal{E}^a : z_e^0 = 1\}$ and $\mathbb{O} := \{e_{ij} \in \mathcal{E}^a : z_e^0 = 0\}$. Using this notation, the local branching constraint is formulated as

$$\Delta(\boldsymbol{z}, \boldsymbol{z}^0) := \sum_{e \in \mathbb{I}} (1 - z_e) + \sum_{e \in \mathbb{O}} (z_e) \leqslant n \tag{3.17}$$

where n is a positive constant. The left-hand side $\Delta(\boldsymbol{z}, \boldsymbol{z}^0) := \sum_{e \in \mathbb{I}} (1 - z_e) + \sum_{e \in \mathbb{O}} (z_e)$ captures the number of variables z_e flipping their values from 0 to 1 or from 0 to 1 with respect to the given solution z_e^0. Hence, the local branching constraint (3.17) can be used to limit the exploration of the solution space by restricting the maximum allowed differences (n) between $\boldsymbol{z}$ and $\boldsymbol{z}^0$ [96]. As a consequence, if n is sufficiently small, the problem can be solved efficiently in the sub-region defined by $\Delta(\boldsymbol{z}, \boldsymbol{z}^0) \leqslant n$. In this chapter, we use $n = 3$.

By incorporating the local branching constraint in formulation $\mathcal{P}^{\mathcal{C}}$, we create a local search algorithm that starts from a reference topology decision and iteratively improves solution quality by locally searching around the best known solution (Algorithm 3). In this algorithm, we use f^u and f^l to denote the best known solution and the current feasible solution of formulation $\mathcal{P}^{\mathcal{C}}$, respectively. Lines 3-5 describe the process for obtaining an initial feasible topology decision $\boldsymbol{z}^0$. In line 3, a relaxed (fractional) topology solution, $\widehat{\boldsymbol{z}}$, is computed by solving formulation $\mathcal{P}^{\mathcal{R}}$ that arises by removing the integrality constraints of variable $\boldsymbol{z}$, i.e., $\mathcal{P}^{\mathcal{R}} := \left\{\mathcal{P}^{\mathcal{C}} : 0 \leqslant z_e \leqslant 1 \;\; \forall e_{ij} \in \mathcal{E}^a\right\}$. Here, the optimal objective value, $f(\widehat{\boldsymbol{z}})$, yields a valid lower bound to problem $\mathcal{P}^{\mathcal{C}}$. Line 4 then rounds fractional $\widehat{\boldsymbol{z}}$ to their nearest integer values (i.e., 0 or 1) and assigns the rounded values to variable $\boldsymbol{z}$. Hence, an initial feasible solution $\boldsymbol{z}^0$ is obtained (i.e., $\boldsymbol{z}^0 = \mathit{Round}(\widehat{\boldsymbol{z}})$) and the optimal objective associated with $\boldsymbol{z}^0$, $f(\boldsymbol{z}^0)$, is evaluated by solving formulation $\mathcal{P}^0$ in line 5. Line 6 initializes the best known solution f^l and the current feasible solution f^u with $f(\widehat{\boldsymbol{z}})$ and $f(\boldsymbol{z}^0)$, respectively. Lines 7-11 are the main body of our local search algorithm. At the beginning of iteration k, line 8 defines the neighbourhood of the incumbent solution $\boldsymbol{z}^{\mathfrak{K}}$ by adding local branching

constraint 3.17 to formulation $\mathcal{P}^{\mathcal{C}}$. Lines 9-10 then evaluate the optimal topology decision in the neighbourhood and update the incumbent solution to this new solution. The process then continues to search from this new topology solution until a (locally) optimal solution is found.

Algorithm 3 A Local Branching Search Algorithm

1: **function** LBR
2: Set $\mathfrak{K} \leftarrow 0$, $f^l \leftarrow -\infty$, $f^u \leftarrow +\infty$
3: $\widehat{\boldsymbol{z}} \leftarrow \textsc{Solve}(\mathcal{P}^{\mathcal{R}})$
4: $\mathcal{P}^{\mathfrak{K}} \leftarrow \left\{\mathcal{P}^{\mathcal{C}} : \boldsymbol{z} = \textsc{Round}(\widehat{\boldsymbol{z}})\right\}$
5: $\boldsymbol{z}^{\mathfrak{K}} \leftarrow \textsc{Solve}(\mathcal{P}^{\mathfrak{K}})$
6: Set $f^l \leftarrow f(\widehat{\boldsymbol{z}})$, $f^u \leftarrow f(\boldsymbol{z}^{\mathfrak{K}})$
7: **while** $\left(\frac{f^u - f^l}{f^l} \leqslant \epsilon\right)$ **do**
8: $\mathcal{P}^{\mathfrak{K}+1} \leftarrow \left\{\mathcal{P}^{\mathcal{C}} : \Delta(\boldsymbol{z}, \boldsymbol{z}^{\mathfrak{K}}) \leqslant n\right\}$
9: $\boldsymbol{z}^{\mathfrak{K}+1} \leftarrow \textsc{Solve}(\mathcal{P}^{\mathfrak{K}+1})$
10: Set $f^l \leftarrow f^u$, $f^l \leftarrow f(\boldsymbol{z}^{\mathfrak{K}+1})$, $\mathfrak{K} \leftarrow \mathfrak{K} + 1$
11: **end while**
12: **return** $\boldsymbol{z}^{\mathfrak{K}+1}$
13: **end function**

3.4 Case Study

In this section, we analyze the performance and sensitivity of a power system when exposed to varying strengths of geo-electric fields induced by GMDs. We use a modified version of the single area IEEE RTS-96 system [112]. Its size is comparable to previous work [123] that considered minimization of the quasi-static GICs and not a full ACOPF with topology control. The derived and modified parameters of IEEE RTS-96 are presented in Table 3.1–3.2. We arbitrarily place the system in western Pennsylvania to give the model a geographic orientation. We assume the cost of shedding load is twice the cost of the most expensive generator. We performed computational experiments using the HPC Palmetto cluster at Clemson University with Intel Xeon E5-2665, 24 cores and 120GB of memory. All implementations are completed using Julia/JuMP [36]. All cases were solved using Gurobi 7.0.2 with default options and its presolver switched on.

Table 3.1: Transformer and transmission line data. The nominal line length parameters of the single area of RTS96 [112] are used to perform an approximate geospatial layout of the power system nodes. (a) The transformer winding resistance (R_{W1}, R_{W2}) and k are estimated based on the test cases provided in [6,58]. (b) The line length is calculated based on the geographic latitudes of substations displayed in Table 3.2.

(a) Transformer data

Name	Type	R_{W1} (Ohm)	Bus No.	R_{W2} (Ohm)	Bus No.	Line No.	k (p.u.)
A 1	Gwye-Gwye	0.12	3	0.18	24	7	1.8
A 2	Auto	0.12	9	0.18	11	14	1.8
A 3	Auto	0.12	9	0.18	12	15	1.8
A 4	Auto	0.12	10	0.18	11	16	1.8
A 5	Auto	0.12	10	0.18	12	17	1.8
G 1	GSU	0.3	1	N/A	25	44	1.8
G 2	GSU	0.3	1	N/A	26	45	1.8
G 3	GSU	0.3	1	N/A	27	46	1.8
G 4	GSU	0.3	1	N/A	28	47	1.8
G 5	GSU	0.3	2	N/A	29	48	1.8
G 6	GSU	0.3	2	N/A	30	49	1.8
G 7	GSU	0.3	2	N/A	31	50	1.8
G 8	GSU	0.3	2	N/A	32	51	1.8
G 9	GSU	0.3	7	N/A	33	52	1.8
G 10	GSU	0.3	7	N/A	34	53	1.8
G 11	GSU	0.3	7	N/A	35	54	1.8
G 12	GSU	0.3	13	N/A	36	55	1.8
G 13	GSU	0.3	13	N/A	37	56	1.8
G 14	GSU	0.3	13	N/A	38	57	1.8
G 15	GSU	0.3	14	N/A	39	58	1.8
G 16	GSU	0.3	15	N/A	40	59	1.8
G 17	GSU	0.3	15	N/A	41	60	1.8
G 18	GSU	0.3	15	N/A	42	61	1.8
G 19	GSU	0.3	15	N/A	43	62	1.8
G 20	GSU	0.3	15	N/A	44	63	1.8
G 21	GSU	0.3	15	N/A	45	64	1.8
G 22	GSU	0.3	16	N/A	46	65	1.8
G 23	GSU	0.3	18	N/A	47	66	1.8
G 24	GSU	0.3	21	N/A	48	67	1.8
G 25	GSU	0.3	22	N/A	49	68	1.8
G 26	GSU	0.3	22	N/A	50	69	1.8
G 27	GSU	0.3	22	N/A	51	70	1.8
G 28	GSU	0.3	22	N/A	52	71	1.8
G 29	GSU	0.3	22	N/A	53	72	1.8
G 30	GSU	0.3	22	N/A	54	73	1.8
G 31	GSU	0.3	23	N/A	55	74	1.8
G 32	GSU	0.3	23	N/A	56	75	1.8
G 33	GSU	0.3	23	N/A	57	76	1.8

(b) Transmission line data

Name	From Bus	To Bus	Length (km)
1	1	2	6.4
2	1	3	85.5
3	1	5	36.7
4	2	4	53.4
5	2	6	71.6
6	3	9	54.0
7	3	24	0.00
8	4	9	43.0
9	5	10	37.6
10	6	10	32.1
11	7	8	25.8
12	8	9	70.0
13	8	10	70.0
14	9	11	0.00
15	9	12	0.00
16	10	11	0.00
17	10	12	0.00
18	11	13	57.8
19	11	14	54.7
20	12	13	57.8
21	12	23	113.4
22	13	23	92.3
23	14	16	44.0
24	15	16	19.6
25	15	21	57.0
26	15	21	57.0
27	15	24	61.8
28	16	17	30.2
29	16	19	29.9
30	17	18	17.3
31	17	22	117.2
32	18	21	28.9
33	18	21	28.9
34	19	20	48.2
35	19	20	48.2
36	20	23	25.1
37	20	23	25.1
38	21	22	83.4

For reference, the peak geo-electric field during the HydroQuebec event of 1989 was 2 V/km [21, 108]. References [4, 91] suggest that 100-year GMDs could cause 5 V/km and 13V/km, respectively, at some high-latitude locations. In our case studies, we consider middle ground, but still extreme, geo-electric fields of 7.5 V/km and 8.7 V/km. We also

Table 3.2: Substation data and other parameters. (a) The substation grounding resistance GR is estimated from typical values of grounding resistance of substations provided in [80]. (b) The original line parameters r_e^o, x_e^o, g_e^o, b_e^o, and b_e^c are scaled by ratio $\beta_e = \frac{L_e}{L_e^o}$ where L_e^o is the original line length of e provided in [112], and L_e represents the calculated line length based on geographic coordinates of substations.

(a) Substation data

Name	Latitude	Longitude	GR(Ohm)
SUB 1	40.44	-78.80	0.1
SUB 2	40.44	-78.73	0.1
SUB 3	40.90	-79.61	0.1
SUB 4	40.70	-79.26	0.1
SUB 5	40.70	-79.07	0.1
SUB 6	41.08	-78.61	0.1
SUB 7	40.50	-78.20	0.1
SUB 8	40.53	-78.50	0.1
SUB 9	41.03	-78.99	0.1
SUB 10	41.22	-78.35	0.1
SUB 11	41.48	-79.26	0.1
SUB 12	41.45	-79.71	0.1
SUB 13	41.63	-79.75	0.1
SUB 14	41.86	-79.94	0.1
SUB 15	42.01	-79.86	0.1
SUB 16	41.77	-79.45	0.1
SUB 17	42.01	-78.95	0.1
SUB 18	41.95	-79.52	0.1
SUB 19	42.41	-78.73	0.1
SUB 20	42.02	-78.65	0.1

(b) Other parameters

Parameter	Value
κ	\$ 1000 /MW (or MVar)
$\overline{I}_e^a$	$T_e / \min\{\underline{V}_i, \underline{V}_j\}$
r_e	$(\beta_e) r_e^o$
x_e	$(\beta_e) x_e^o$
g_e	$(\frac{1}{\beta_e}) g_e^o$
b_e	$(\frac{1}{\beta_e}) b_e^o$
b_e^c	$(\frac{1}{\beta_e}) b_e^c$
$\overline{\theta}$	30°

study the directionality of the event by considering field directions between 0° and 180° spaced by 5°.

To analyze the benefits of GIC mitigation by topology control, generator dispatch, and load shedding, we studied three cases. To describe these cases, we define $\mathbf{z}_x^*$ and $\mathfrak{C}_x^*$ to be the optimal topology (line on-off) decisions and objective (minimum total costs), respectively, for case x. The solutions of $\mathbf{z}_x^*$ and $\mathfrak{C}_x^*$ are obtained from model M_x that are formulated below. The cases we consider are:

1. C1: The ACOTS model neglecting GIC effects ($\mathfrak{C}_o^*$, $\mathbf{z}_o^*$):

   $M_o := \big\{ \min (3.6a) : (3.11) - (3.13); (3.6j) - (3.6m); \boldsymbol{z} \in \{0,1\}^{|\mathcal{E}^a|}; \boldsymbol{d}^{qloss} = \mathbf{0} \big\}$

2. C2: The ACOTS with GIC effects ($\mathfrak{C}_{gmd}^*$, $\mathbf{z}_{gmd}^*$)[1]:

[1] $\mathfrak{C}_{gmd}^*$, $\mathbf{z}_{gmd}^*$ are locally optimal solutions to model M_{gmd} obtained by the LBR method. We show that they are also global optima for the RTS96 test system in Section 3.4.

$$M_{gmd} := \left\{ \min (3.6a) : (3.11) - (3.15); (3.6j) - (3.6m); (3.6u) - (3.6v); \boldsymbol{z} \in \{0,1\}^{|\mathcal{E}^a|} \right\}$$

3. C3: The ACOPF (fixed $\mathbf{z} = \mathbf{z}_o^*$) with GIC effects ($\mathfrak{C}_f^*$, $\mathbf{z}_o^*$):

   $$M_f := \left\{ \min (3.6a) : (3.11) - (3.15); (3.6j) - (3.6m); (3.6u) - (3.6v); \boldsymbol{z} = \boldsymbol{z}_o^* \right\}$$

4. C4: The ACOPF (fixed $\mathbf{z} = 1$) with GIC effects ($\mathfrak{C}_{\mathbf{1}}^*$, $\mathbf{1}$):

   $$M_{\mathbf{1}} := \left\{ \min (3.6a) : (3.11) - (3.15); (3.6j) - (3.6m); (3.6u) - (3.6v); \boldsymbol{z} = \mathbf{1} \right\}$$

Case C1 defines the topology $\mathbf{z}_o^*$ and evaluates the objective $\mathfrak{C}_o^*$ that results from neglecting the effects of GICs. Case C2 considers the GIC mitigation using both generation dispatch and topology control. Case C3 evaluates cost $\mathfrak{C}_f^*$ that results from mitigating GIC effects with generation dispatch on the topology of C1. Case C4 is similar to Case C3, but line switching is not allowed.

3.4.1 Case C1: Potential Damage by GICs

Under normal circumstances without GMDs, line switching decisions are determined by economic dispatch. More specifically, the optimal system topology is obtained by solving an ACOTS model without the GIC-effects constraints (Case C1). Figure 3.4(a) shows the optimal normal topology, $\mathbf{z}_o^*$, where some generators are not injecting real or reactive power[2]. For example, generators 16 through 20 are shut down at node 15, and their GSU transformers are disconnected from the network using the circuit breakers. Referring to Fig. 3.1(a), we note that this action does not significantly affect the topology of the AC network, which is only affected by switching transmission lines. This action removes GSU transformer ground points from the DC network topology over which the GICs flow.

Case C1 assumes that generation and system topology are optimized for cost while neglecting the impact of GICs. This impact is calculated using constraints (3.6s) through (3.6u) to evaluate the feasibility of thermal limit constraint (3.6x). Figure 3.4(b) shows how many GSU and network transformers would be overheated under C1 depending on

[2]There are multiple generators located at buses 1, 2 and 15. Generators 1 and 2 at bus 1 have the same cost and capacity, as do generators 5 and 6 at bus 2 and generators 16 through 20 at bus 15. Thus, there are equivalent dispatch solutions.

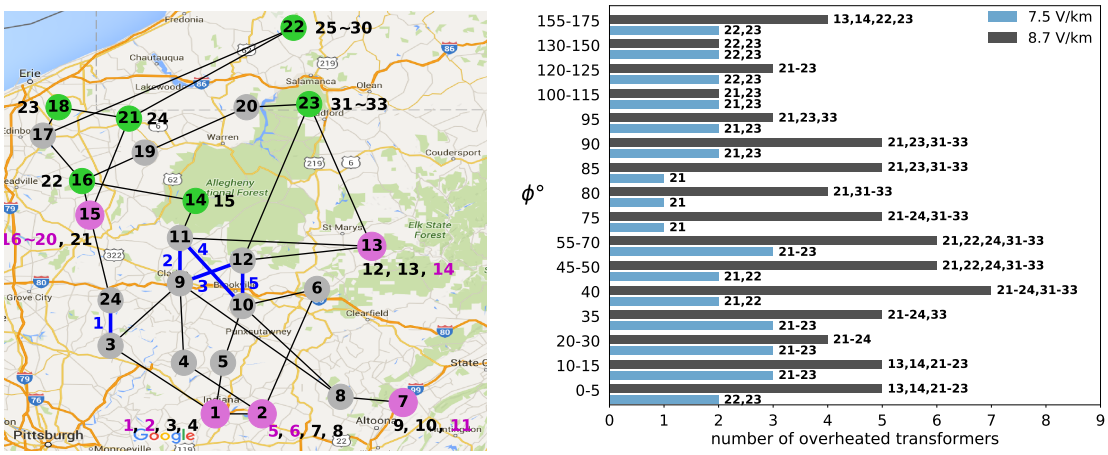

(a) Optimal topology $\mathbf{z}_o^*$ in Case C1

(b) Potential damage of transformers by GICs

Figure 3.4: Evaluation of the power system in Table 3.1–3.2 for Case C1. (a) The grey nodes are loads. The blue lines indicate network transformers (Gwye-Gwye and auto- transformers). The green and magenta nodes indicate GSU transformers. Transformer IDs are listed next to the node. Generation nodes with disconnected GSU transformers are magenta and their (network or GSU) transformer IDs are marked as magenta as well. (b) The Case C1 solution is tested by applying geo-electric fields of strength 7.5 V/km and 8.7 V/km for all directions. The label above each bar indicates IDs of overheated transformers.

the direction and strength of the GMD. For example, when the electric field is 7.5 V/km, GSU transformers 22 (at node 16) and 23 (at node 18) are overheated when the event is oriented between 90° and 175°. When the strength is increased to 8.7 V/km, one or more transformers are overheated at almost all orientations of the GMD. For example, when the event is oriented at 40°, seven GSU transformers (21-24, 31-33) are overheated. These results provide a baseline to evaluate alternative operating paradigms that ensure system security.

3.4.2 Case C2: GIC Mitigation via ACOTS

Using Case C2, the cost benefits of simultaneous controlling generation dispatch and network topology to mitigate GIC effects are evaluated.

Cost Analysis For geo-electric field strengths of 7.5 V/km and 8.7 V/km, Case C2 is solved for orientations of the field from 0 to 180°, which results in a total cost $\mathfrak{C}^*_{gmd}$ (see Fig. 3.5) and topology $\boldsymbol{z}^*_{gmd}$ (discussed later). The results in Fig. 3.5 show that the directions

of the geo-electric field are not all equivalent because the cost of mitigation, $\mathfrak{C}^*_{gmd}$, varies with direction. The most costly GMDs occur when the event is oriented between 20° and 110°. The increase in cost between 7.5 V/km and 8.7 V/km is primarily due to changes in generator dispatch and is not significant. For example, the difference in cost between the 7.5 V and 8.7 V per kilometer case is 1.25% when the GMD is oriented at 60°. Moreover, the dispatch cost is smaller when GIC effects are neglected (Case C1). However, the transformer thermal limit constraints are violated when GIC effects are applied to the network (as seen in Fig. 3.4(b)). Thus, there is an implicit higher cost associated with replacing the damaged equipment and unexpected load shed when the transformer fails.

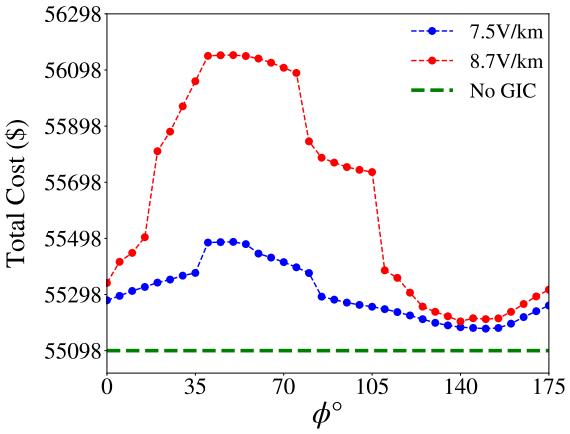

Figure 3.5: The total cost c^*_{gmd} for Case C2 for different geo-electric field orientations and strengths.

Topology Control Analysis In Figure 3.5, the network topology varies with the strength and direction of the GMD. In the remainder of this section, we focus on GMD events oriented at 40°, 80°, 110°, and 140° because total costs $\mathfrak{C}^*_{gmd}$ fluctuate widely in these directions. Figures 3.6 and 3.7 display the network topology for geo-electric field strengths of 7.5 V/km and 8.7 V/km, respectively. In Figure 3.6, for the 40° geo-electric field case, two transmission lines, (1,5) and (15,16), are switched off. In the 80° geo-electric field case, only one transmission lines (1,5), which is nearly perpendicular to the geo-electric field, is switched off. This topology control is likely being used to reroute power flow away from more susceptible transmission lines (e.g., line (1,5)). When event orientations are at 110° and 140°, all transmission lines are switched on and the corresponding total costs are

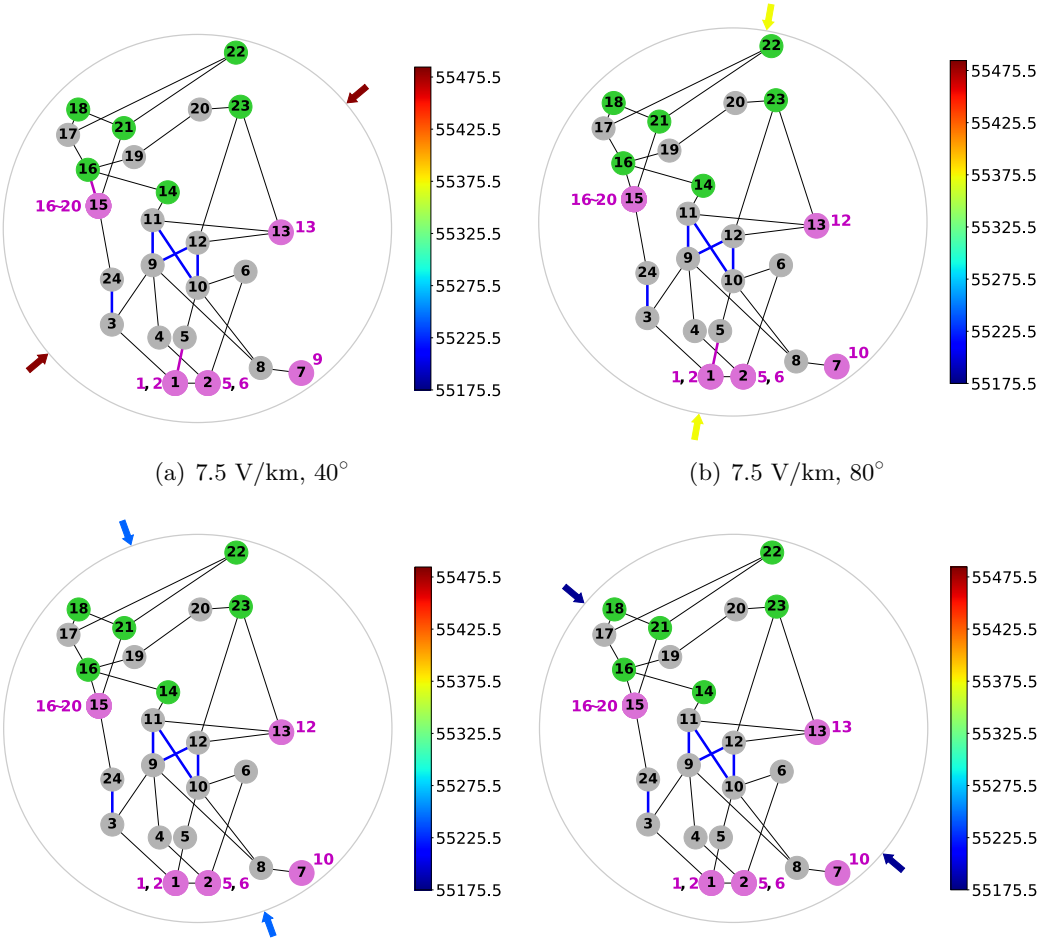

(a) 7.5 V/km, 40°

(b) 7.5 V/km, 80°

(c) 7.5 V/km, 110°

(d) 7.5 V/km, 140°

Figure 3.6: Topology solutions for Case C2 at 7.5 V/km strength and orientations from 40°, 80°, 110°, and 140°. Switched off lines are colored magenta and the IDs of unused generators are labeled beside their connected substations.

significantly reduced. Our experimental results indicate that more transmission lines are switched off when orientation directions are more sensitive to GMDs (e.g., 40° and 80°), resulting in higher total costs.

The results in Figure 3.7 for different geo-electric field orientations suggest similar conclusions. At a fixed 8.7 V/km in Figure 3.7, the optimal topology solutions switch off several transmission lines, while some transmission lines still display significant sensitivity to orientation (e.g., line (1,5)). Comparing Figure 3.7 (8.7 V/km) with Figure 3.6 (7.5 V/km) suggests that some topology solutions at low field strength persist to higher field strength;

however, more GSU transformers are disconnected from the network to avoid large GIC in their connected transformers. The sensitivity of the topology solution to the details of the orientation and the difficulty in making accurate predictions of geo-electric field direction suggest that the ACOTS solution should be extended to a stochastic or robust formulation over field strength. Finally, we note that while the solution adjusts the topology, it does not create islands–a mitigation strategy that is sometimes suggested. However, islands could form in larger, more complex networks.

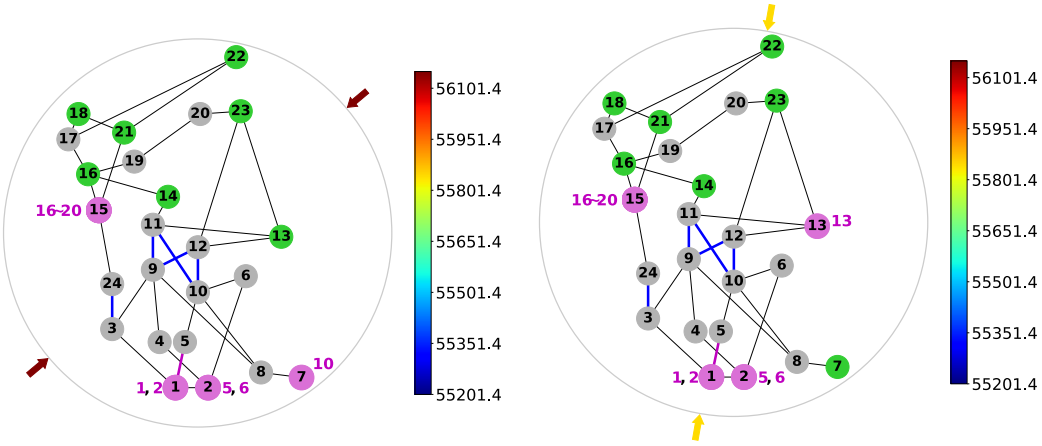

(a) 8.7 V/km, 40°

(b) 8.7 V/km, 80°

(c) 8.7 V/km, 110°

(d) 8.7 V/km, 140°

Figure 3.7: Same as Fig 3.6 but for a geo-electric field strength of 8.7 V/km.

3.4.3 Case C2 versus Case C3: Cost Benefits of Topology Optimization

The inclusion of topology control into the ACOTS formulation increases the complexity of the problem, but it also provides significant cost savings over a less complex ACOPF. The cost savings are evaluated by comparing Case C2 (where topology control is allowed) with Case C3 (where the topology is fixed to that found in Case C1). Figure 3.8 displays the percentage cost savings of C2 (ACOTS) over C3 (ACOPF) for 7.5 V/km and 8.7 V/km field strengths with directions between 0°–180°. Under the most severe GMD conditions explored, the benefit of topology control is as much as 45%.

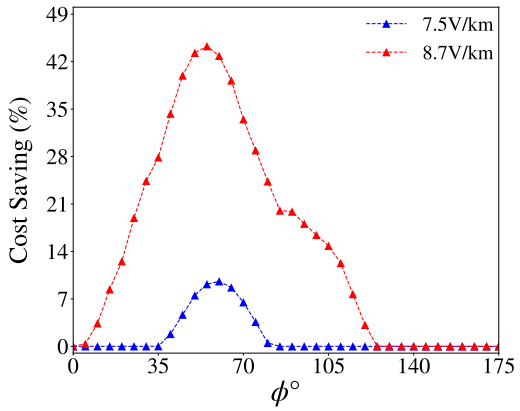

Figure 3.8: Combined savings from generator dispatch and load shedding costs enabled by the optimal topology $\mathbf{z}^*_{gmd}$ found by ACOTS relative to the dispatch and load shedding cost incurred by the ACOPF of Case C3 with the topology fixed to $\mathbf{z}^*_0$.

Table 3.3 further breaks down the cost savings of Case C2 over Case C3 into generator dispatch costs and load shedding costs. For the 8.7 V/km field strength case, the topology control in Case C2 enables all of the load to be served. In contrast, the fixed topology in C3 results in load shedding costs of 9.3% on average and 28.0% in the worst case.

3.4.4 Case C3 versus Case C4: Performance of Network Reconfiguration

The results displayed in Figure 3.9 compare the topology of Case C3 (where topology is fixed to case C1) with Case C4 (where all lines and generators). Similar to the results

Table 3.3: Percentage of the total cost in cases C2 and C3 due to generator dispatch and load shedding. For 7.5 V/km and 8.7 V/km strengths, the average, minimum and maximum percentage of total cost is computed over the geo-electric field orientation from 0°–180°.

		Dispatch Cost(%)			Load shedding Cost(%)		
Strength	Case	Avg.	Min.	Max.	Avg.	Min.	Max.
7.5 V/km	C2	100.0	100.0	100.0	0.0	0.0	0.0
	C3	97.8	96.0	100.0	0.4	0.0	4.0
8.7 V/km	C2	100.0	100.0	100.0	0.0	0.0	0.0
	C3	92.7	72.0	100.0	9.3	0.0	28.0

in Fig. 3.9(a), the total cost, $\mathfrak{C}_1^*$, varies with event direction. Ignoring GIC effects also induces a lower operating cost (Fig. 3.9(b)). However, like the results of Fig. 3.4(b), we also observed that the transformer thermal limit constraints (3.6x) are violated when GIC effects are neglected. For example, if the field strength is 8.7 V/km and has an orientation of 100°, GSU transformers 21 and 23 overheat. Comparing Fig. 3.9(a) (Case C3) with Fig. 3.9(b) (Case C4) shows that the optimal topology control found in Case C1 induces a higher cost than Case C4 for orientations through 20° to 105° under the field of 8.7 V/km. This is due to forced disconnect of generators in Case C1 (e.g., generator 14 at bus 13) which could be dispatched more effectively, when no line can be switched off, to mitigate GIC effects.

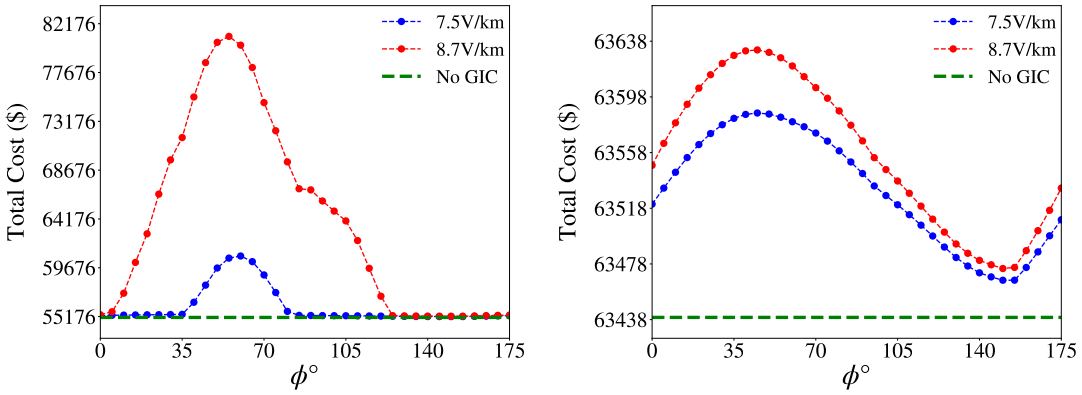

(a) The total cost c_f^* in Case C3.

(b) The total cost c_1^* in Case C4.

Figure 3.9: Cost comparison of Case C3 and C4 for different geo-electric field orientations and strengths.

3.4.5 Computational Analysis

To evaluate the computational performance of the proposed LBR method, we compare LBR with the branch-and-cut (B&C) algorithm performed by the Gurobi MIP optimizer with default options and its presolver switched on. In this section, we only consider Case C2 where the corresponding solutions are obtained by LBR. Note that Gurobi solves the formulation M_{gmd} (Case C2) to optimality, while LBR aims to find a near-optimal solution which could be a local optimum.

Solution Quality We compare the solution quality of LBR with Gurobi by testing the following null hypothesis: there is no difference between the objective values from the two methods (i.e., the solutions are statistically indistinguishable). Paired t-test results are included in Table 3.4.

Table 3.4: Paired t-tests for comparison of the optimal objective and computational times obtained from Gurobi and the LBR method. Δ Total Cost (Wall time) represents the objective (computational time) difference between Gurobi and LBR. N, $\overline{X}_d$ and S_d denote the sample size, mean and standard deviation, respectively.

		Δ Total Cost ($)				Δ Wall Time (sec)			
Strength (V/km)	N	$\overline{X}_d$	S_d	t-score	p-value	$\overline{X}_d$	S_d	t-score	p-value
7.5	36	-0.1	0.5	-0.74	0.46	844.0	858.0	5.90	9.4e-6
8.7	36	0.0	0.3	-0.43	0.67	4389.4	5389.1	4.89	2.1e-6

The values under column "Δ Total Cost" show that the p-values associated with this hypothesis test are 0.46 and 0.67 for 7.5 V/km and 8.7 V/km, respectively. Since both 0.46 and 0.67 are greater than 0.05, we cannot reject the null hypothesis at a 95% significance level. In addition, the full range of solution differences between LBR and Gurobi is displayed in Figure 3.10(a). The plot suggests that the LBR solution is always within ± 0.2 ($) of the optimal total cost found by Gurobi, which is less than 0.0004% based on the scale of objective values presented in Figure 3.5. Hence, we conclude that for the RTS96 test case, solutions obtained by LBR are not statistically different with the optimal solutions from Gurobi.

Computational Speed Table 3.5 summarizes the computational time properties of solv-

ing formulation M_{gmd} (Case C2) with these two methods. We observe that the LBR algorithm offers a significant improvement in computation time as compared to Gurobi, especially at larger geo-electric field strengths. Indeed, when strength is 8.7 V/km, Gurobi takes 25264 seconds (≈7 hours) in the worst case to respond to the event. In contrast, LBR can find the optimal solution for any direction between 0°-180° within 1403 seconds (≈23 minutes), which is 18-19 times faster than Gurobi. The distributional characteristics of the computational difference are shown in Figure 3.10(b) which indicates that computations from Gurobi are much more time-intensive than LBR. Similarly, we also conduct a paired t-test with the following null hypothesis on computation time: there is no difference between the computational times of the two methods. The t-test results are summarized in column "Δ Wall Time" in Table 3.4. For 7.5 V/km and 8.7 V/km strengths, the p-values associated with this hypothesis are almost 0.0, which are less than 0.05. Therefore, there is strong evidence to reject the null hypothesis and conclude that LBR does lead to a significant improvement in computational speed. These results suggest that our proposed LBR method can be a practical algorithm for obtaining high-quality solutions to larger power flow systems on the time scale required for GMD mitigation efforts.

Table 3.5: Computational time comparisons of the single-area RTS96 system. The average, minimum, maximum and standard deviation of solving time are presented over the geo-electric field orientation from 0°–180°. Under "Method" column, "Gurobi(B&C)" represents the B&C method performed by the Gurobi MIP solver, and "LBR" denotes the proposed local search algorithm in section 3.3.

		Wall Time (sec)			
Strength (V/km)	Method	Avg.	Min.	Max.	Std.
7.5	LBR	664.0	420.5	1249.6	172.8
	Gurobi(B&C)	1508.0	646.0	3914.6	934.3
8.7	LBR	802.7	401.0	1403.1	235.4
	Gurobi(B&C)	5192.1	610.7	25263.6	5492.2

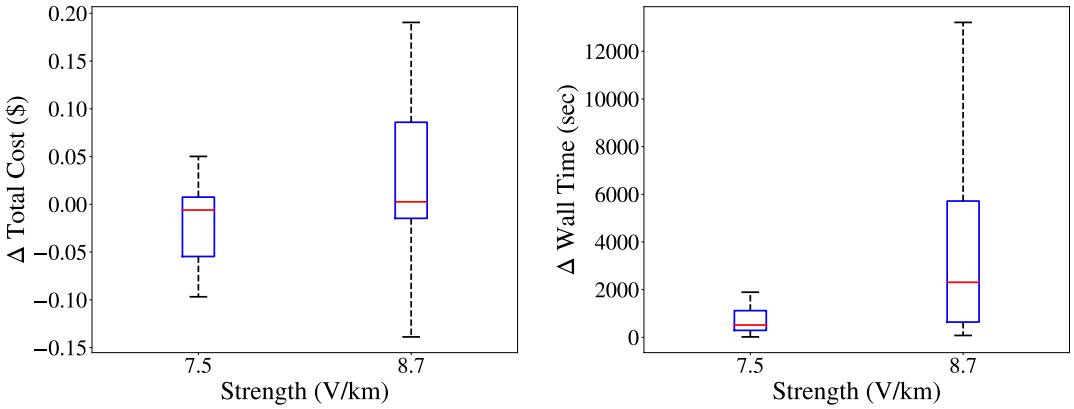

(a) The total cost difference

(b) The computational time difference

Figure 3.10: Performance comparison between the GRB and LBR method.

3.5 Conclusions and Future Research

We formulate a detailed topology control optimization model to mitigate the impacts of GMDs on electrical transmission systems. Our mathematical formulation minimizes total generation dispatch and load shedding, subject to non-convex AC power flow physics, the effects of geomagnetically-induced currents on transformer heating, and transformer reactive power consumption. We leverage recently developed convex relaxation approaches to handle the nonlinearites due to AC transmission switching and GIC constraints. Further, we propose a heuristic to find high-quality feasible solutions within the time scales required for GMD mitigation efforts. Further research will include developing exact algorithms to solve larger problems, modeling time-extended variations in the geo-electric field, and considering N-1 security constraints.

Chapter 4

Distributionally Robust Optimization for Resilient Transmission Grids under Geomagnetic Disturbances

In recent years, there have been increasing concerns about the impacts of geomagnetic disturbances (GMDs) on electrical power systems. Unpredictable GMDs, that are caused by uncontrollable solar storms, can significantly increase the risk of transformer failure. In this research, we propose a two-stage distributionally robust (DR) optimization model that captures uncertain GMDs and mitigates the effects of GICs on power systems through existing system controls. This model assumes an ambiguity set of probability distributions of the induced geo-electric field to capture the uncertain magnitude and orientation of a GMD event. We employ state-of-the-art linear relaxation methods and reformulate the proposed two-stage DR model that creates a decomposition framework for solving our problem. We demonstrate the approach on the modified Epri21 system and show that the DR optimization method effectively handles prediction errors of GMD events.

Nomenclature

Sets

$\mathcal{N}^a, \mathcal{N}^d$	set of nodes in the AC and DC circuit, respectively
$\mathcal{N}^g \subseteq \mathcal{N}^a$	set of nodes with exactly one generator
$\mathcal{E}^a, \mathcal{E}^d, \mathcal{E}$	set of edges in the AC and DC circuit, respectively, where $\mathcal{E} = \mathcal{E}^a \cup \mathcal{E}^d$
$\mathcal{E}^\tau \subseteq \mathcal{E}^a$	set of transformer edges
$\mathcal{E}^w \subseteq \mathcal{E}^d$	set of DC edges used to model transformer windings in the DC circuit
$\mathcal{E}^w_e \subseteq \mathcal{E}^d$	set of DC edges used to model the windings for transformer edges $e_{ij} \in \mathcal{E}^\tau$
$\mathcal{E}^+_i \subseteq \mathcal{E}$	set of outgoing edges connected to AC/DC node i
$\mathcal{E}^-_i \subseteq \mathcal{E}$	set of incoming edges connected to AC/DC node i
$\mathcal{E}_i$	set of all edges connected to AC/DC node i, where $\mathcal{E}_i = \mathcal{E}^+_i \cup \mathcal{E}^-_i$
$\mathcal{E}^\tau_i \subseteq \mathcal{E}^\tau$	set of AC edges used to compute d_i^{qloss} (as described later) for node i
$\mathcal{E}^g \subseteq \mathcal{E}^a$	set of edges e_{ij} such that either i or $j \in \mathcal{N}^g$

Parameters

c_i^0	fixed cost for generator $i \in \mathcal{N}^g$
c_i^1, c_i^2	fuel cost coefficients of electricity generation ρ_i from generator $i \in \mathcal{N}^g$

c_i^{R1}, c_i^{R2}	fuel cost coefficients of additional electricity generation Δ_i from generator $i \in \mathcal{N}^g$
$\mathcal{F}_i(\cdot)$	fuel cost function of electricity generation from generator $i \in \mathcal{N}^g$
κ_i^+, κ_i^-	penalty of load shedding and over-generation at bus $i \in \mathcal{N}^a$, respectively
a_m	admittance of the grounding line at bus $m \in \mathcal{I}$, 0 if bus $m \notin \mathcal{I}$
a_e	DC admittance of edge $e \in \mathcal{E}^d$
r_e, x_e	resistance and reactance of line $e \in \mathcal{E}^a$
g_e, b_e	conductance and susceptance of line $e \in \mathcal{E}^a$
g_i, b_i	shunt conductance and susceptance at bus $i \in \mathcal{N}^a$
d_i^p, d_i^q	real and reactive power demand at bus $i \in \mathcal{N}^a$
b_e^c	line charging susceptance of line $e \in \mathcal{E}^a$
s_e	apparent power limit on line $e \in \mathcal{E}^a$
$\overline{\theta}$	phase angle difference limit
k_e	loss factor of transformer line $e \in \mathcal{E}^\tau$
$\underline{v}_i$, $\overline{v}_i$	AC voltage limits at bus $i \in \mathcal{N}^a$
$\underline{gp}_i$, $\overline{gp}_i$	real power generation limits at generator $i \in \mathcal{N}^g$
$\underline{gq}_i$, $\overline{gq}_i$	reactive power generation limits at generator $i \in \mathcal{N}^g$
$-\overline{u}_i^R, \overline{u}_i^R$	ramp-down and ramp-up limits for generator i, respectively
$\vec{E}$	the geo-electric field at the area of a transmission system
L_e^N,L_e^E	the northward and eastward components of the displacement of each transmission line $e \in \mathcal{E}^a$, respectively

First-Stage Variables

z_e 1 if line $e \in \mathcal{E}^a$ is switched on; 0 otherwise

ρ_i reserved real-power output of generator $i \in \mathcal{N}^a$

Second-Stage Variables

θ_i phase angle at bus $i \in \mathcal{N}^a$

v_i voltage magnitude at bus $i \in \mathcal{N}^a$

v_i^d induced DC voltage magnitude at bus $i \in \mathcal{N}^d$

l_e^d GIC flow on transformer line $e \in \mathcal{E}^\tau$

I_e^d the effective GIC on transformer line $e \in \mathcal{E}^\tau$

d_i^{qloss} GIC-induced reactive power loss at bus $i \in \mathcal{N}^a$

Δ_i^p excess real power generated at generator $i \in \mathcal{N}^g$

p_{ij}, q_{ij} real and reactive power flow on line $e_{ij} \in \mathcal{E}^a$, as measured at node i

f_i^p, f_i^q real and reactive power generated at bus $i \in \mathcal{N}^a$

l_i^{p+}, l_i^{q+} real and reactive power shed at bus $i \in \mathcal{N}^a$

l_i^{p-}, l_i^{q-} real and reactive power over-generated at bus $i \in \mathcal{N}^a$

Random Variables

$\widetilde{\nu}^E$, $\widetilde{\nu}^N$ GMD-induced geo-electric fields in Eastward and Northward, respectively

$\widetilde{\nu}_e^d$ induced voltage sources on transmission line $e \in \mathcal{E}$, as a function of $\widetilde{\nu}^E$ and $\widetilde{\nu}^N$

4.1 Introduction

Solar flares and coronal mass ejections form solar storms where a billion tons of charged particles escape from the sun and arrive at Earth causing geomagnetic disturbances

(GMDs). GMDs lead to changes in Earth's magnetic field, which then create geo-electric fields. These low-frequency geo-electric fields induce quasi-DC currents, also known as Geomagnetically-Induced Currents (GICs), in grounded sections of power system networks [10, 11, 105]. GICs are superimposed on the existing alternating currents (AC) and bias the AC in transformers. This bias can lead to half-cycle saturation and magnetic flux loss in regions outside of the transformer core. The energy stored in the stray flux increases the reactive power consumption of transformers, which could lead to load shedding since, in general, generators are not designed to handle such unexpected losses. In addition, the stray flux also drives eddy currents that can cause excessive transformer heating, which leads to reduced transformer life or, potentially, immediate damage [7]. Damaged transformers can disconnect the bulk electric power system and disrupt its ability to deliver power. Particularly, when GMD events occur on large-scale electric power systems, the resulting power outages can be catastrophic. For example, the GMD event in Quebec in 1989 led to the shutdown of the Hydro-Quebec power system. As a consequence, six million people suffered a power outage for nine hours. A report estimated that the net cost of this event was $13.2 million, with damaged equipment accounting for $6.5 million of the cost [19].

The potential GMD impacts to transformers in the bulk electric power system have motivated the United States government to sponsor research which will improve our understanding of GMD events and identify strategies to mitigate the impact of GMDs on power systems [8, 40]. To model the potential risks introduced by GICs, both the academia and the electric power industry have actively improved GIC modeling and GIC monitoring [25, 38, 58, 89, 94]. For example, the North American Electric Reliability Corporation (NERC) presented a procedure to quantify GICs in a system based on the corresponding geo-electric field [6]. These models have been used to conduct risk analyses that estimate the sensitivity of reactive power losses due to GICs. It was found that risk mitigation warrants further study.

The recent literature mainly focuses on mitigating two primary risks introduced by GICs. The first is voltage sag resulted from increased reactive power consumption on

transformers [7]; the second is transformer damage caused by excessive hot-spot thermal heating [1]. One mitigation approach is installing DC-current blocking devices to keep the GIC from accessing transformer neutrals [20]. However, these devices are expensive since a single unit can cost \$500K [66, 71, 123]. This high cost is a barrier for adopting this technology in practice. To address this issue, Lu *et al.* [74] developed a GIC-aware optimal AC power flow (ACOPF) model that uses existing topology control to mitigate the risks of GIC impacts. This work showed that topology reconfiguration can effectively protect power systems from GIC impacts, and left the development of a scalable algorithm for large systems as future work.

The model proposed by Lu *et al.* [73] is a first study of this problem – – their findings are insightful. However, the paper assumes a steady GMD event (i.e., the induced geo-electric field is constant). In reality, solar storms, such as solar flares and coronal mass ejections (CMEs), are unpredictable. Although ground- and space-based sensors and imaging systems have been utilized by the National Aeronautics and Space Administration (NASA) to observe these activities at various depths in the solar atmosphere, the intensity of a storm cannot be measured until the released particles reach Earth and interact with its geomagnetic field [85]. As a result, there is often uncertainty in predictions of solar storms and the induced geo-electric field, which introduce operational challenges of mitigating the potential risks by GIC to power systems.

This research extends our initial study of GIC effects induced by a GMD [74] in two ways. The model (1) allows line switching and generator ramping to mitigate GIC impacts and (2) assumes uncertain magnitude and orientation of a GMD. We formulate this problem as a two-stage distributionally robust (DR) optimization model which we call DR-OTSGMD. The first-stage problem selects a set of transmission lines and generators to serve power in a power system ahead of an imminent GMD event. The second-stage problem evaluates the performance of the network given the status of transmission lines, the reserved electricity for daily power service, and a realized GMD. In this model, the uncertain magnitude and direction of a GMD are captured by an ambiguity set of probability

distributions of the induced geo-electric field. The objective is to minimize the expected total cost for the worst-case distribution defined in the ambiguity set. Instead of assuming a specific candidate distribution, the ambiguity set is described by statistical properties of uncertainty, such as the support and moment information. As a result, the DR optimization approach yields less conservative solutions than the prevalent robust optimization [117,121]. In comparison to stochastic programming, the DR method does not require the complete information of the exact probability distribution, thus the decision does not rely on assumptions about unknown distributions [14]. Additionally, the reliability of the solutions found does not require a large number of random samples, leading to computational tractability and scalability for large-scale problems [70]. In the literature, the DR optimization approaches have been used to model a variety of problems [35, 37, 39, 45, 60, 101]. Recent work has focused on modeling the relevant problems in power systems, such as contingency-constrained unit commitment [28, 117, 120], optimal power flow with uncertain renewable energy generation [70, 75, 116, 119], planning and scheduling of power systems [17, 110], and energy management [93, 111].

We present a two-stage DR-OTSGMD model of the AC optimal power flow (OPF) problem with GIC effects induced by uncertain GMD events. The objective is to minimize the worst-case expected total cost over all probability distributions in an ambiguity set that is defined to capture the uncertainty of the GMD-induced geo-electric field. The main contributions of this chapter include:

- A two-stage DR-OTSGMD model that captures the uncertainty of the GMD-induced geo-electric field. This formulation considers the AC physics of power flow and reactive power consumption at transformers due to random GICs.

- A reformulation of the two-stage DR-OTSGMD problem which facilitates problem decomposition. The resulting problems are nonlinear and non-convex due to the AC physics of power flow. We show that solutions to these problems provide valid lower bounds.

- Extensive numerical analysis using the Epri21 test system validates the model and demonstrates the effectiveness of the proposed model to generate robust solutions.

The remainder of this chapter is organized as follows. In section 4.2, we discuss the two-stage DR-OTSGMD formulation and the ambiguity set of probability distributions for the induced geo-electric field. We describe linear approximations of nonlinear and non-convex functions in the problem, then derive a decomposition framework for solving this approximation. In Section 4.3, we present a column-and-constraint generation algorithm and demonstrate this approach using the Epri21 test system in Section 4.4. Finally, we conclude this chapter and provide directions for future research in Section 4.5.

4.2 Problem Formulation

4.2.1 GIC modeling

The computation of GIC-induced reactive power losses depends on the induced voltage sources ($\widetilde{\nu}_e^d$) on each power line $e \in \mathcal{E}^d$ in the network, which itself is determined by the geo-electric field integrated along the length of each transmission line. This relationship is modeled in Eq.(4.1)

$$\widetilde{\nu}_e^d = \oint \vec{E}_e \cdot d\vec{l}_e, \tag{4.1}$$

where, $\vec{E}_e$ is the geo-electric field in the area of transmission line $e \in \mathcal{E}^d$, and $d\vec{l}_e$ is the incremental line segment length including direction [6]. In practice, the actual geo-electric field varies with geographical locations. In this research, we use a common assumption that the geo-electric field in the geographical area of a transmission grid is uniformly distributed [6, 58, 123], i.e., $\vec{E} = \vec{E}_e$ for any $e \in \mathcal{E}^d$. Hence, only the coordinates of the line ending points are relevant and $\vec{E}$ can be resolved into its eastward (x axis) and northward (y axis) components [6]. Let $\vec{L}_e$ be the length of line e with direction. Thus, (4.1) can be reformulated as:

$$\widetilde{\nu}_e^d = \vec{E} \cdot \vec{L}_e = \widetilde{\nu}^N L_e^N + \widetilde{\nu}^E L_e^E, \quad \forall e \in \mathcal{E} \tag{4.2}$$

where $\widetilde{\nu}^N$ and $\widetilde{\nu}^E$ represent the geo-electric fields (V/km) in the northward and eastward directions, respectively, which are modeled as random variables in our model. L_e^N and L_e^E denote distances (km) along the northward and eastward directions, respectively, which depend on the geographical location (i.e., latitude and longitude) of associated substations [6].

4.2.2 The two-stage DR-OTSGMD Formulation

A transmission network is modeled as a graph with nodes $\mathcal{N}$ (buses and generators) and edges $\mathcal{E}$ (lines and transformers). Each edge has a switch which is represented as a binary variable used to control the on-off status of this line. For notation brevity, each edge $e_{ij} \in \mathcal{E}$ is given an arbitrary orientation from bus i to bus j, and we omit the ij subscript when the orientation is not relevant. We present a two-stage DR-OTSGMD formulation as the following.

$$\mathcal{Q}_o := \min_{\boldsymbol{z},\boldsymbol{\rho}} \sum_{i\in\mathcal{N}^g, e\in\mathcal{E}_i} z_e(c_i^0) + \sum_{i\in\mathcal{N}^g} \mathcal{F}_i(\rho_i) + \sup_{\mathbb{P}\in\mathbb{Q}} \mathbb{E}_{\mathbb{P}}[\mathcal{H}(\boldsymbol{z},\boldsymbol{\rho},\widetilde{\boldsymbol{\nu}}^{\boldsymbol{d}})] \tag{4.3a}$$

$$s.t. \quad z_e \in \{0,1\} \qquad \forall e_{ij} \in \mathcal{E}^a \tag{4.3b}$$

$$z_e \underline{gp}_i \leqslant \rho_i \leqslant z_e \overline{gp}_i \qquad \forall i \in \mathcal{N}^g, e \in \mathcal{E}_i \tag{4.3c}$$

The first-stage problem (4.3), referred to as the master problem, specifies a system topology and the real-power generation reserved for daily electricity consumption. The objective is to minimize the worst-case expected total cost including the fixed cost for keeping generators on and the fuel cost for the reserved essential real-power outputs. Constraint set (4.3b) defines line switching variables, and constraint set (4.3c) limits the reserved real-power generation that is determined prior to an imminent event. In the objective (4.3a), the fuel cost $\mathcal{F}_i(\rho_i)$ is formulated as a quadratic function of ρ_i, i.e., $\mathcal{F}_i(\rho_i) = c_i^2(\rho_i)^2 + c_i^1\rho_i$. Given on-off status z_e, reserved real-power generation ρ_i, and a realized GMD event measured by $\widetilde{\nu}^E$ and $\widetilde{\nu}^N$, $\mathcal{H}(\boldsymbol{z},\boldsymbol{\rho},\widetilde{\boldsymbol{\nu}}^{\boldsymbol{d}})$ represents the recourse cost and equals to the optimal objective value of the second-stage (which is referred to as the subproblem) formulated as

below.

$$\mathcal{H}(\boldsymbol{z}, \boldsymbol{\rho}, \widetilde{\nu}^d) = \min \sum_{i \in \mathcal{N}^g} \mathcal{F}_i(\Delta_i^p) + \sum_{i \in \mathcal{N}^a} \kappa_i^+ (l_i^{p+} + l_i^{q+}) + \kappa_i^- (l_i^{p-} + l_i^{q-}) \tag{4.4a}$$

$$s.t. \sum_{e_{ij} \in \mathcal{E}_i^+} p_{ij} + \sum_{e_{ji} \in \mathcal{E}_i^-} p_{ij} = f_i^p + l_i^{p+} - l_i^{p-} - d_i^p - v_i^2 g_i \qquad \forall i \in \mathcal{N}^a \tag{4.4b}$$

$$\sum_{e_{ij} \in \mathcal{E}_i^+} q_{ij} + \sum_{e_{ji} \in \mathcal{E}_i^-} q_{ij} = f_i^q + l_i^{q+} - l_i^{q-} - d_i^q - d_i^{qloss} + v_i^2 b_i \qquad \forall i \in \mathcal{N}^a \tag{4.4c}$$

$$p_{ij} = z_e(g_e v_i^2 - g_e v_i v_j \cos(\theta_i - \theta_j) - b_e v_i v_j \sin(\theta_i - \theta_j)) \qquad \forall e_{ij} \in \mathcal{E}^a \backslash \mathcal{E}^g \tag{4.4d}$$

$$q_{ij} = z_e(-(b_e + \frac{b_e^c}{2}) v_i^2 + b_e v_i v_j \cos(\theta_i - \theta_j) - g_e v_i v_j \sin(\theta_i - \theta_j)) \qquad \forall e_{ij} \in \mathcal{E}^a \backslash \mathcal{E}^g \tag{4.4e}$$

$$p_{ji} = z_e(g_e v_j^2 - g_e v_i v_j \cos(\theta_j - \theta_i) - b_e v_i v_j \sin(\theta_j - \theta_i)) \qquad \forall e_{ij} \in \mathcal{E}^a \backslash \mathcal{E}^g \tag{4.4f}$$

$$q_{ji} = z_e(-(b_e + \frac{b_e^c}{2}) v_j^2 + b_e v_i v_j \cos(\theta_j - \theta_i) - g_e v_i v_j \sin(\theta_j - \theta_i)) \qquad \forall e_{ij} \in \mathcal{E}^a \backslash \mathcal{E}^g \tag{4.4g}$$

$$p_{ij} + p_{ji} = 0, \; q_{ij} + q_{ji} = 0 \qquad \forall e_{ij} \in \mathcal{E}^g \tag{4.4h}$$

$$\underline{v}_i \leqslant v_i \leqslant \overline{v}_i \qquad \forall i \in \mathcal{N}^a \tag{4.4i}$$

$$z_e |\theta_i - \theta_j| \leqslant \overline{\theta} \qquad \forall e_{ij} \in \mathcal{E}^a \backslash \mathcal{E}^g \tag{4.4j}$$

$$p_{ij}^2 + q_{ij}^2 \leqslant z_e s_e^2, \quad p_{ji}^2 + q_{ji}^2 \leqslant z_e s_e^2 \qquad \forall e_{ij} \in \mathcal{E}^a \tag{4.4k}$$

$$z_e \underline{gp}_i \leqslant f_i^p \leqslant z_e \overline{gp}_i \qquad \forall i \in \mathcal{N}^g, e \in \mathcal{E}_i \tag{4.4l}$$

$$z_e \underline{gq}_i \leqslant f_i^q \leqslant z_e \overline{gq}_i \qquad \forall i \in \mathcal{N}^g, e \in \mathcal{E}_i \tag{4.4m}$$

$$-z_e \overline{u}_i^R \overline{gp}_i \leqslant f_i^p - \rho_i \leqslant z_e \overline{u}_i^R \overline{gp}_i \qquad \forall i \in \mathcal{N}^g, e \in \mathcal{E}_i \tag{4.4n}$$

$$\Delta_i^p \geqslant 0, \quad \Delta_i^p \geqslant f_i^p - \rho_i \qquad \forall i \in \mathcal{N}^g \tag{4.4o}$$

Formulations (4.4a) through (4.4o) describe system constraints for buses and branches in the AC circuit that takes into account the additional reactive power consumption due to GICs. The objective function (4.4a) minimizes the total cost including the fuel cost for the ramp-up generation of real power and the penalty for load shedding and over-generation. Note that the over-generation variables are introduced to facilitate the feasibility of the subproblem, thus l_i^{p-} and l_i^{q-} should be zero at optimality by associating them with very high penalty cost κ_i^-. Constraints (4.4b) and (4.4c) represent the nodal real and reactive power balance, including the reactive power consumption due to GICs. Constraints (4.4d) through (4.4g) model AC power flow on each transmission line with on-off variables z_e. Constraint set (4.4h) indicates that *fictitious* lines between output terminals of generators and their injection buses are modeled as transportation edges (i.e.,

$|p_{ij}| = |-p_{ji}| = f_i^p, |q_{ij}| = |-q_{ji}| = f_i^q \ \ \forall e_{ij} \in \mathcal{E}^g$). Constraints (4.4i) through (4.4o) describe the operational limits of the grid; constraint set (4.4i) limits the voltage magnitude at buses, while constraint set (4.4j) applies appropriate bounds on the phase angle difference between two buses when the line exists. Constraint set (4.4k) models operational thermal limits of lines in both directions. Constraints (4.4l) and (4.4m) model the availability and capacity of power generation; a generator is offline if its line is switched off. Constraints (4.4n) limit the deviations of real power generations from the reserved amount ρ_i. These ramp-down and ramp-up amounts are used to balance the additional reactive power consumption due to GICs. Constraints (4.4o) model the ramp-up generation (i.e., positive deviation) of real power at each generator. If generator $i \in \mathcal{N}^g$ ramps up, the minimum Δ_i^p is equal to $f_i^p - \rho_i$; 0 otherwise. Note that the fuel cost $F_i(\Delta_i^p)$ takes into account only the ramp-up power generation, thus there is no fuel cost if generator $i \in \mathcal{N}^g$ ramps down. Particularly, $\Delta_i^p = \max\{0, \ f_i^p - \rho_i\}$ and $F_i^R(0) = 0$.

$$\sum_{e \in \mathcal{E}_m^+} z_{\overrightarrow{e}} a_e \widetilde{\nu}_e^d - \sum_{e \in \mathcal{E}_m^-} z_{\overrightarrow{e}} a_e \widetilde{\nu}_e^d = -a_m v_m^d - \sum_{e_{mn} \in \mathcal{E}_m^+} z_{\overrightarrow{e}} a_e (v_m^d - v_n^d) + \sum_{e_{nm} \in \mathcal{E}_m^-} z_{\overrightarrow{e}} a_e (v_n^d - v_m^d) \ \forall m \in N^d \tag{4.5a}$$

$$I_e^d = z_{\overrightarrow{e}} a_e (v_m^d - v_n^d) \quad \forall e_{mn} \in \mathcal{E}^w \tag{4.5b}$$

$$\widetilde{I}_e^d \geqslant \sum_{\hat{e}_{ij} \in \mathcal{E}_e^w} \Theta(I_{\hat{e}}^d), \quad \widetilde{I}_e^d \geqslant -\sum_{\hat{e}_{ij} \in \mathcal{E}_e^w} \Theta(I_{\hat{e}}^d) \quad \forall e \in \mathcal{E}^\tau \tag{4.5c}$$

$$0 \leqslant \widetilde{I}_e^d \leqslant \max_{\forall \hat{e} \in \mathcal{E}^a} 2\overline{I}_{\hat{e}}^a \qquad \forall e \in \mathcal{E}^\tau \tag{4.5d}$$

$$d_i^{qloss} = \sum_{e \in \mathcal{E}_i^\tau} k_e v_i I_e^d \qquad \forall i \in \mathcal{N}^a \tag{4.5e}$$

The induced DC circuit and the effects associated with a GMD event are formulated in constraints (4.5a)-(4.5e). Recall that we link an edge $e \in \mathcal{E}^d$ in the DC circuit to an edge in the AC circuit with $\overrightarrow{e}$. In particular, for $e \in \mathcal{E}^d$, we use notation $\overrightarrow{e}$ to denote the associated AC edge of e. This is a one-to-one mapping for transmission lines and a many-to-one mapping for transformers (see Chapter 3). Using this notation, constraints (4.5a) and (4.5b) calculate the GIC flow on each DC line by applying Kirchhoff's current law. The GIC on a line is determined by the induced voltage source $\widetilde{\nu}_e^d$ and the quasi-DC voltage difference between two buses [6]. GIC flow is forced to 0 by $z_{\overrightarrow{e}}$ when line $\overrightarrow{e}$ is switched off. Instead of introducing additional discrete variables, constraint (4.5c) is used to model and relax the magnitude of $\sum_{\hat{e}_{ij} \in \mathcal{E}_e^w} \Theta(I_{\hat{e}}^d)$ where $\Theta(\cdot)$ is a linear function of GICs in transformer

windings defined in the form of (3.3)–(3.5) (see Chapter 3). Constraint set (4.5d) denotes the maximum allowed value of GIC flowing through transformers. We assume this limit is twice the upper bound of the AC flow in the network. Constraint set (4.5e) computes the reactive power load due to transformer saturation [11, 89, 122, 123] by using the effective GICs for each transformer type. The couplings between AC power flows and GIC occur in constraints (4.4c) and (4.5e).

4.2.3 Linear Approximation

Note that the subproblem (4.4a)–(4.5e) described above is nonlinear and non-convex, which is computationally hard to solve to optimality. In this section, we present outer-approximation methods to linearize these nonlinear terms in the subproblem.

Perspective Reformulation and Relaxation of the Fuel Cost Function In this chapter, fuel cost $\mathcal{F}_i(\cdot)$ is formulated as a quadratic function of the real power generation from generator $i \in \mathcal{N}^g$. Particularly, for each generator $i \in \mathcal{N}^g$, $\mathcal{F}_i(\Delta_i) = c_i^{R2}(\Delta_i)^2 + c_i^{R1}\Delta_i^p$ and $\mathcal{F}_i(f_i^p) = c_i^2(f_i^p)^2 + c_i^1 f_i^p$. For notation brevity, we represent the fuel cost function in a generic form: $\mathcal{F}_i(x_i) = \mathcal{C}^2(x_i)^2 + \mathcal{C}^1 x_i$. Next, we define a new variable $\breve{x}_i$ to capture the quadratic term $(x_i)^2$, such that

$$\breve{x}_i := (x_i)^2 \qquad \forall i \in \mathcal{N}^g \tag{4.6a}$$

Using perspective reformulation methods described in [50, 51, 72], we present a piecewise linearization of $\mathcal{F}_i(x_i)$ as follows:

$$\mathcal{F}_i(x_i) = \mathcal{C}_i^2 \breve{x}_i + \mathcal{C}_i^1 x_i \qquad \forall i \in \mathcal{N}^g \tag{4.7a}$$

$$\breve{x}_i \geqslant 2x_i^\ell(x_i) - z_e(x_i^\ell)^2 \qquad \forall i \in \mathcal{N}^g, e \in \mathcal{E}_i, \ell \in \{1, 2, ..., L\} \tag{4.7b}$$

where L represents the number of pieces and x_i^ℓ is a given real-power output of generator $i \in \mathcal{N}^g$ on piece ℓ. Constraints (4.7b) are referred to as perspective cuts which have been widely exploited to tighten convex relaxations for a class of indicator-induced MINLPs

[50, 72, 87]. If generator $i \in \mathcal{N}^g$ is turned off (i.e., $z_e = 0$), then the optimal solution of $\breve{x}_i$ should be 0, as this is a minimization problem. Otherwise, if $z_e = 1$, constraints (4.7b) define the feasible region of $\breve{x}_i$ to outer approximate the quadratic term in the cost function. Note that we reformulate both $\mathcal{F}_i(\rho_i)$ and $\mathcal{F}_i(\Delta_i^p)$ in the form of (4.7).

Linear Approximation of AC Physics Let $\mathcal{L}(\cdot)$ denotes a set of piecewise linear functions used to approximate a nonlinear (non-convex) term. We define new variables w_i for each bus $i \in \mathcal{N}^a$ and w_e^z, w_e^c, and w_e^s for each edge $e_{ij} \in \mathcal{E}^a$ to capture the non-convexities in the AC power flow equations (4.4b)–(4.4g). In particular, for $\forall i \in \mathcal{N}^a$ and $\forall e_{ij} \in \mathcal{E}^a \backslash \mathcal{E}^g$, we define

$$w_i := v_i^2, \quad w_{ie}^z := z_e v_i^2, \quad w_e^c := v_i v_j \cos(\theta_i - \theta_j), \quad w_e^s := v_i v_j \sin(\theta_i - \theta_j) \tag{4.8a}$$

Using this notation, formulation (4.4a)–(4.4m) can be reformulated as follows:

$$\min \quad (4.4a) \tag{4.9a}$$

$$s.t. \sum_{e_{ij} \in \mathcal{E}_i^+} p_{ij} + \sum_{e_{ji} \in \mathcal{E}_i^-} p_{ij} = f_i^p + l_i^{p+} - l_i^{p-} - d_i^p - w_i g_i \qquad \forall i \in \mathcal{N}^a \tag{4.9b}$$

$$\sum_{e_{ij} \in \mathcal{E}_i^+} q_{ij} + \sum_{e_{ji} \in \mathcal{E}_i^-} q_{ij} = f_i^q + l_i^{q+} - l_i^{q-} - d_i^q - d_i^{qloss} + w_i b_i \qquad \forall i \in \mathcal{N}^a \tag{4.9c}$$

$$p_{ij} = g_e w_{ie}^z - g_e w_e^c - b_e w_e^s \qquad \forall e_{ij} \in \mathcal{E}^a \backslash \mathcal{E}^g \tag{4.9d}$$

$$q_{ij} = -(b_e + \frac{b_e^c}{2}) w_{ie}^z + b_e w_e^c - g_e w_e^s \qquad \forall e_{ij} \in \mathcal{E}^a \backslash \mathcal{E}^g \tag{4.9e}$$

$$p_{ji} = g_e w_{je}^z - g_e w_e^c + b_e w_e^s \qquad \forall e_{ij} \in \mathcal{E}^a \backslash \mathcal{E}^g \tag{4.9f}$$

$$q_{ji} = -(b_e + \frac{b_e^c}{2}) w_{je}^z + b_e w_e^c + g_e w_e^s \qquad \forall e_{ij} \in \mathcal{E}^a \backslash \mathcal{E}^g \tag{4.9g}$$

$$z_e \underline{w}_e^c \leqslant w_e^c \leqslant z_e \overline{w}_e^c \qquad \forall e_{ij} \in \mathcal{E}^a \backslash \mathcal{E}^g \tag{4.9h}$$

$$z_e \underline{w}_e^s \leqslant w_e^s \leqslant z_e \overline{w}_e^s \qquad \forall e_{ij} \in \mathcal{E}^a \backslash \mathcal{E}^g \tag{4.9i}$$

$$z_e \underline{v}_i^2 \leqslant w_{ie}^z \leqslant z_e \overline{v}_i^2, \quad z_e \underline{v}_j^2 \leqslant w_{je}^z \leqslant z_e \overline{v}_j^2 \qquad \forall e_{ij} \in \mathcal{E}^a \backslash \mathcal{E}^g \tag{4.9j}$$

$$w_i - \overline{v}_i^2 (1 - z_e) \leqslant w_{ie}^z \leqslant w_i - \underline{v}_i^2 (1 - z_e) \qquad \forall e_{ij} \in \mathcal{E}^a \backslash \mathcal{E}^g \tag{4.9k}$$

$$w_j - \overline{v}_j^2(1-z_e) \leqslant w_{je}^z \leqslant w_j - \underline{v}_j^2(1-z_e) \qquad \forall e_{ij} \in \mathcal{E}^a \backslash \mathcal{E}^g \tag{4.9l}$$

$$\tan(\underline{\theta}) w_e^s \leqslant w_e^c \leqslant \tan(\overline{\theta}) w_e^s \qquad \forall e_{ij} \in \mathcal{E}^a \backslash \mathcal{E}^g \tag{4.9m}$$

$$\mathcal{L}\Big((w_e^c)^2 + (w_e^s)^2 - w_i w_j\Big) \leqslant 0 \qquad \forall e_{ij} \in \mathcal{E}^a \backslash \mathcal{E}^g \tag{4.9n}$$

$$w_i \geqslant \mathcal{L}(v_i^2) \qquad \forall i \in \mathcal{N}^a \tag{4.9o}$$

$$w_i \leqslant (\overline{v}_i + \underline{v}_i) v_i - \overline{v}_i \underline{v}_i \qquad \forall i \in \mathcal{N}^a \tag{4.9p}$$

$$\mathcal{L}(p_{ij}^2 + q_{ij}^2) \leqslant z_e s_e^2 \qquad \forall e_{ij} \in \mathcal{E}^a \tag{4.9q}$$

$$\mathcal{L}(p_{ji}^2 + q_{ji}^2) \leqslant z_e s_e^2 \qquad \forall e_{ij} \in \mathcal{E}^a \tag{4.9r}$$

$$(4.4h) - (4.4i), (4.4l) - (4.4m), (4.7a) - (4.7b), (4.4n) - (4.4o) \tag{4.9s}$$

In this formulation, constraints (4.9d)–(4.9g) force line flows to be zero when the line is switched-off and take the associated values otherwise, due to constraints (4.9h)–(4.9l). Constraints (4.9j)–(4.9l) represent the McCormick [77] relaxations of a bilinear product with one binary variable. Constraints (4.9m) are used to link new introduced variables w_e^s and w_e^c for each edge, and is equivalent to the phase angle limit constraints (4.4j). Constraint set (4.9n) describes linearizations of the second-order conic (SOC) constraints $(w_e^c)^2 + (w_e^s)^2 \leqslant w_i w_j$, where $\mathcal{L}(\cdot)$ is formulated as:

$$\mathcal{L}\Big((w_e^c)^2 + (w_e^s)^2 - w_i w_j\Big) = 2\Big(w_e^c w c_e^{\ell k} + w_e^s w s_e^{\ell k}\Big) - (w c_e^{\ell k})^2 - (w s_e^{\ell k})^2 - w_i w_j^\ell - w_j w_i^\ell + w_i^\ell w_j^\ell \qquad \forall e_{ij} \in \mathcal{E}^a,\ \ell \in \{1, ..., L\},\ k \in \{1, ..., K\} \tag{4.10a}$$

$$w_i^\ell = \frac{(\overline{w}_i - \underline{w}_i)\ell}{L}, \quad w_j^\ell = \frac{(\overline{w}_j - \underline{w}_j)\ell}{L} \qquad \forall e_{ij} \in \mathcal{E}^a,\ \ell \in \{1, ..., L\} \tag{4.10b}$$

$$w c_e^{\ell k} = w_i^\ell w_j^\ell \cos(\frac{2\pi k}{K}), \quad w s_e^{\ell k} = w_i^\ell w_j^\ell \sin(\frac{2\pi k}{K}) \qquad \forall e_{ij} \in \mathcal{E}^a,\ \ell \in \{1, ..., L\} \tag{4.10c}$$

where both L and K are the total number of pieces (it is possible that $L \neq K$), and the number of added linear cuts is $L \times K$. Next, constraints (4.9o)–(4.9p) linearize the quadratic term $w_i := v_i^2$ for each bus $i \in \mathcal{N}^a$. We present their associated piecewise linear functions

$\mathcal{L}(\cdot)$ as:

$$\mathcal{L}(v_i^2) = 2v_i^\ell v_i - (v_i^\ell)^2, \quad v_i^\ell = \frac{(\overline{v}_i - \underline{v}_i)\ell}{L} \qquad \forall i \in \mathcal{N}^a,\ \ell \in \{1, ..., L\} \tag{4.11}$$

where v_i^ℓ is a given voltage value on piece $\ell \in \{1, ..., L\}$. Similarly, line capacity constraints (4.4j) can be outer approximated as the following:

$$\mathcal{L}(p_{ij}^2 + q_{ij}^2) = 2p_{ij}p_{ij}^\ell - (p_{ij}^\ell)^2 + 2q_{ij}q_{ij}^\ell - (q_{ij}^\ell)^2 \qquad \forall e_{ij} \in \mathcal{E}^a,\ \ell \in \{1, ..., L\} \tag{4.12a}$$

$$\mathcal{L}(p_{ji}^2 + q_{ji}^2) = 2p_{ji}p_{ji}^\ell - (p_{ji}^\ell)^2 + 2q_{ji}q_{ji}^\ell - (q_{ji}^\ell)^2 \qquad \forall e_{ij} \in \mathcal{E}^a,\ \ell \in \{1, ..., L\} \tag{4.12b}$$

$$p_{ij}^\ell = p_{ji}^\ell = s_e \cos(\frac{2\pi\ell}{L}), \quad q_{ij}^\ell = q_{ji}^\ell = s_e \sin(\frac{2\pi\ell}{L}) \qquad \forall \ell \in \{1, ..., L\} \tag{4.12c}$$

Convex Envelopes of Bilinear terms in the GIC-Associated DC Circuit We note that all nonlinearities and non-convexities are from these bilinear terms: (1) $z_{\overrightarrow{e}}(v_m^d - v_n^d)$ and (2) $v_i I_e^d$. Given any two variables x_i, $x_j \in \mathbb{R}$, the McCormick (MC) relaxation [77] can be used to linearize bilinear product $x_i x_j$ by introducing a new variable $\breve{x}_{ij} \in \langle x_i, x_j \rangle^{MC}$. The feasible region of $\breve{x}_{ij}$ is defined as follows:

$$\breve{x}_{ij} \geqslant \underline{x}_i x_j + \underline{x}_j x_i - \underline{x}_i\, \underline{x}_j \tag{4.13a}$$

$$\breve{x}_{ij} \geqslant \overline{x}_i x_j + \overline{x}_j x_i - \overline{x}_i\, \overline{x}_j \tag{4.13b}$$

$$\breve{x}_{ij} \leqslant \underline{x}_i x_j + \overline{x}_j x_i - \underline{x}_i\, \overline{x}_j \tag{4.13c}$$

$$\breve{x}_{ij} \leqslant \overline{x}_i x_j + \underline{x}_j x_i - \overline{x}_i\, \underline{x}_j \tag{4.13d}$$

$$\underline{x}_i \leqslant x_i \leqslant \overline{x}_i,\ \underline{x}_j \leqslant x_j \leqslant \overline{x}_j \tag{4.13e}$$

Let $v_{mn}^{zd} := z_{\overrightarrow{e}}(v_m^d - v_n^d)$ and $u_{ie}^d := v_i I_e^d$, the linearzied formulations of (4.5a)-(4.5e) are presented below:

$$\sum_{e \in \mathcal{E}_m^+} z_{\overrightarrow{e}} a_e \widetilde{\nu}_e^d - \sum_{e \in \mathcal{E}_m^-} z_{\overrightarrow{e}} a_e \widetilde{\nu}_e^d = -a_m v_m^d - \sum_{e_{mn} \in \mathcal{E}_m^+} a_e v_{mn}^{zd} + \sum_{e_{nm} \in \mathcal{E}_m^-} a_e v_{nm}^{zd} \quad \forall m \in \mathcal{N}^d \tag{4.14a}$$

$$l_e^d = a_e v_{mn}^{zd} \qquad \forall e_{mn} \in \mathcal{E}^w \tag{4.14b}$$

$$d_i^{qloss} = \sum_{e \in \mathcal{E}_i^\tau} k_e u_{ie}^d \qquad \forall i \in \mathcal{N}^a \tag{4.14c}$$

$$v_{mn}^{zd} \in \langle z_{\overrightarrow{e}},\ v_m^d - v_n^d \rangle^{MC} \qquad \forall e_{mn} \in \mathcal{E}^d \tag{4.14d}$$

$$u_{ie}^d \in \langle v_i,\ I_e^d \rangle^{MC} \qquad \forall i \in \mathcal{N}^a,\ e \in \mathcal{E}_i^\tau \tag{4.14e}$$

$$(4.5c) - (4.5d) \tag{4.14f}$$

4.2.4 Model of Uncertainty

This section focuses on constructing an ambiguity set (denoetd by $\mathbb{Q}$) of probability distributions for the random geo-electric field induced by a GMD event. Let $\widetilde{\boldsymbol{\omega}}$ be a vector of all random variables (i.e., $\widetilde{\boldsymbol{\omega}} = [\widetilde{\nu}^E, \widetilde{\nu}^N]^T$), and $\boldsymbol{\mu} = [\mu^E, \mu^N]^T$ be the mean vector of the eastward and northward geo-electric fields, then ambiguity set $\mathbb{Q}$ can be formulated in the following form:

$$\mathbb{Q} = \begin{cases} & \widetilde{\boldsymbol{\omega}} \in \mathbb{R}^2 \\ \mathbb{P} \in \mathcal{P}_0(\mathbb{R}): & \mathbb{E}_{\mathbb{P}}(\widetilde{\boldsymbol{\omega}}) = \boldsymbol{\mu} \\ & \mathbb{P}\Big(\widetilde{\boldsymbol{\omega}} \in \Omega\Big) = 1 \end{cases} \tag{4.15}$$

where $\mathcal{P}_0(\mathbb{R})$ denotes the set of all probability distributions on $\mathbb{R}$ and $\mathbb{P}$ presents a probability measure in $\mathcal{P}_0$. Note that random variables $\widetilde{\boldsymbol{\omega}}$ are not associated with any specific probability distribution. The second line of $\mathbb{Q}$ suggests that the expectation of $\widetilde{\boldsymbol{\omega}}$ is $\boldsymbol{\mu}$. The third line defines the support of the random variables, Ω, which contains all the possible outcomes of $\widetilde{\boldsymbol{\omega}}$. We formulate this support set based on valid bounds of geo-electric fields in eastward and northward directions, such that:

$$\Omega := \Big\{(\widetilde{\nu}^N, \widetilde{\nu}^E) \in \mathbb{R}: 0 \leqslant \widetilde{\nu}^N \leqslant \overline{\nu}^M,\ -\overline{\nu}^M \leqslant \widetilde{\nu}^E \leqslant \overline{\nu}^M,\ \mathcal{L}\Big((\widetilde{\nu}^N)^2 + (\widetilde{\nu}^E)^2\Big) \leqslant (\overline{\nu}^M)^2\Big\} \tag{4.16a}$$

The first two constraints in Ω define individual bounds of $\widetilde{\nu}^N$ and $\widetilde{\nu}^E$, respectively. Given a prespecified upper bound on the geo-electric field amplitude (denoted by $\overline{\nu}^M$), the third inequality further limits the values of $\widetilde{\nu}^N$ and $\widetilde{\nu}^E$, where $\mathcal{L}\Big((\widetilde{\nu}^N)^2 + (\widetilde{\nu}^E)^2\Big)$ denotes a set

of piecewise linear functions of the following form:

$$\mathcal{L}\Big((\widetilde{\nu}^N)^2 + (\widetilde{\nu}^E)^2\Big) = 2\widetilde{\nu}^N\widetilde{\nu}^N_\ell - (\widetilde{\nu}^N_\ell)^2 + 2\widetilde{\nu}^E\widetilde{\nu}^E_\ell - (\widetilde{\nu}^E_\ell)^2 \qquad \forall \ell \in \{1, ..., L\} \tag{4.17a}$$

$$\widetilde{\nu}^N_\ell = \overline{\nu}^M \cos(\frac{\pi\ell}{L}), \;\; \widetilde{\nu}^E_\ell = \overline{\nu}^M \sin(\frac{\pi\ell}{L}) \qquad \forall \ell \in \{1, ..., L\} \tag{4.17b}$$

where L represents the number of linear pieces. $\widetilde{\nu}^N_\ell$ and $\widetilde{\nu}^E_\ell$ are given values of $\widetilde{\nu}^N$ and $\widetilde{\nu}^E$, respectively, on piece ℓ. Recall that we model the geomagnetic field magnitude in a rectangular form $(\widetilde{\nu}^N)^2+(\widetilde{\nu}^E)^2 = (|\vec{E}|)^2$ (see Eq.(4.2)), thus the bounds of combined $\widetilde{\nu}^N$ and $\widetilde{\nu}^E$ are calculated as $(\widetilde{\nu}^N)^2+(\widetilde{\nu}^E)^2 \leqslant (\overline{\nu}^M)^2$. In this research, we linearize Ω using (4.17) and reformulate this two-stage DRO-OTSGMD model as a tractable mixed-integer linear (MIP) model (discussed in the next section). Figure 4.1 gives two examples that illustrate feasible domains of $\widetilde{\nu}^E$ and $\widetilde{\nu}^N$, where vector $\vec{E}$ represents the geo-electric field in the area of a transmission system. In the figure, the dotted half cycle represents the quadratic boundary of $\vec{E}$ (i.e., $(\widetilde{\nu}^E)^2 + (\widetilde{\nu}^N)^2 \leqslant (\overline{\nu}^M)^2$). The tangent lines at this boundary are used to outer approximate the feasible domain of random variables and formulated as (4.17) (i.e., $L = 5$ in the figure). In this case, Ω can be represented by the surrounded (yellow) area under these tangent lines. Note that the figure only presents the angle of $\vec{E}$ from 0 (east) to π (north) because the geo-electric field is uniform and the effects are symmetric with respect to east (west) direction [74]. For notation brevity, we express uncertainty set Ω in the following linear matrix form:

$$\Omega := \Big\{\widetilde{\boldsymbol{\omega}} \in \mathbb{R}^2 : \boldsymbol{D}\widetilde{\boldsymbol{\omega}} \leqslant \boldsymbol{d}\Big\} \tag{4.18a}$$

where $\boldsymbol{D} \in \mathbb{R}^{M_0 \times |\widetilde{\boldsymbol{\omega}}|}$ and $\boldsymbol{d} \in \mathbb{R}^{M_0}$, M_0 is the number of constraints in the support set Ω. In the next section, we use this linear form of Ω to present a reformulation of the two-stage DR-OTSGMD problem described in Section 4.2.2.

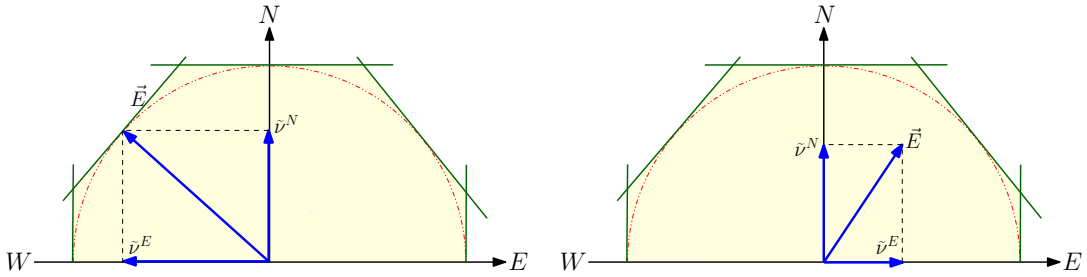

(a) $\tilde{\nu}^E < 0$, $|\vec{E}| = \overline{\nu}^M$ (b) $\tilde{\nu}^E > 0$, $|\vec{E}| < \overline{\nu}^M$

Figure 4.1: Examples of feasible regions of $\tilde{\nu}^E$ and $\tilde{\nu}^N$. The geo-electric field $\vec{E}$ is formed by $\tilde{\nu}^E$ and $\tilde{\nu}^N$. In Fig.4.1(a), the magnitude of $\vec{E}$ equals $\overline{\nu}^M$ and angle relative to east is larger than $\frac{\pi}{2}$. In Fig.4.1(b), the magnitude of $\vec{E}$ is less than $\overline{\nu}^M$ and the angle is smaller than $\frac{\pi}{2}$.

4.2.5 Reformulation of the Two-Stage DR-OTSGMD

Using linear approximation methods described in Section 4.2.3, the subproblem becomes linear and it returns a *lower bound* of the original objective. For notation brevity, we present the linearized program in a succinct form as follows:

$$\min_{\boldsymbol{y}} \boldsymbol{a}^T\boldsymbol{y} + \sup_{\mathbb{P}\in\mathbb{Q}} \mathbb{E}_{\mathbb{P}}[\mathcal{H}(\boldsymbol{y}, \tilde{\boldsymbol{\omega}})] \tag{4.19a}$$

$$s.t. \quad y_i \in \{0,1\} \qquad \forall i \in \{1,2,...,|\mathcal{E}^a|\} \tag{4.19b}$$

$$\boldsymbol{A}\boldsymbol{y} \geqslant \boldsymbol{b} \tag{4.19c}$$

where

$$\mathcal{H}(\boldsymbol{y}, \tilde{\boldsymbol{\omega}}) = \min_{\boldsymbol{x}} \boldsymbol{c}^T\boldsymbol{x} \tag{4.19d}$$

$$s.t. \quad \boldsymbol{G}\boldsymbol{y} + \boldsymbol{E}\boldsymbol{x} \geqslant \boldsymbol{h} \tag{4.19e}$$

$$\boldsymbol{T}(\tilde{\boldsymbol{\omega}})\boldsymbol{y} = \boldsymbol{W}\boldsymbol{x} \tag{4.19f}$$

where $\boldsymbol{y} = [\boldsymbol{z}, \boldsymbol{\rho}]^T$ represents first-stage variables. $\boldsymbol{x} = [\Delta^p,\ f^p,\ f^q,\ p,\ g,\ \theta, v,\ w,\ w^z,\ w^c,\ w^s,\ v^d,\ l^d,\ I^d,\ v^{zd},\ u^d,\ d^{qloss}]^T$ consists of the second-stage recourse variables that depend on random variables $\tilde{\boldsymbol{\omega}}$. Let N_1 and N_2 is the dimension of $\boldsymbol{y}$ and $\boldsymbol{x}$, respectively; M_1 be the number of constraints in the first stage; M_2 and M_3 represent the number of constraints that are independent of and affected by random variables, respectively. Constraints (4.19b)

represent constraints (4.3b). Constraints (4.19c) represent constraints (4.3c) and (4.7a)–(4.7b), where $\boldsymbol{A} \in \mathbb{R}^{M_1 \times N_1}$ and $\boldsymbol{b} \in \mathbb{R}^{M_1}$. Constraints (4.19e) represent constraints (4.9b)–(4.12c) and (4.14b)–(4.14f), where $\boldsymbol{G} \in \mathbb{R}^{M_2 \times N_1}$, $\boldsymbol{E} \in \mathbb{R}^{M_2 \times N_2}$ and $\boldsymbol{h} \in \mathbb{R}^{M_2}$. Constraint set (4.19f) represents constraints (4.14a) that are all equations involved the random variables in the second stage, where $\boldsymbol{T}(\widetilde{\boldsymbol{\omega}}) \in \mathbb{R}^{M_3 \times N_1}$ and $\boldsymbol{W} \in \mathbb{R}^{M_3 \times N_2}$. The detailed formulation presented in Section 4.2.2 shows that only coefficient matrix $\boldsymbol{T}(\widetilde{\boldsymbol{\omega}}) \in \mathbb{R}^{M_3 \times N_1}$ is affected by random variables $\widetilde{\boldsymbol{\omega}}$ (see Eq. (4.14a)). Particularly, $\boldsymbol{T}(\widetilde{\boldsymbol{\omega}})$ is an affine function of $\widetilde{\boldsymbol{\omega}}$, such that $\boldsymbol{T}(\widetilde{\boldsymbol{\omega}}) = \sum_{i=1}^{|\widetilde{\boldsymbol{\omega}}|} \boldsymbol{T}^i \widetilde{\omega}_i$ where $\boldsymbol{T}^i \in \mathbb{R}^{M_3 \times N_1} \quad \forall i = 0, 1, ..., |\widetilde{\boldsymbol{\omega}}|$.

In remainder of this section, we derive a reformulation of the two-stage DR-OTSGMD problem which can be solved by applying a decomposition framework. First, we present an equivalent formulation of the worst-case expected cost $\sup_{\mathbb{P} \in \mathbb{Q}} \mathbb{E}_{\mathbb{P}}[\mathcal{H}(\boldsymbol{y}, \widetilde{\boldsymbol{\omega}})]$ in the objective function (4.19a). According to Zhao *et al.* [120], it can be written as an optimization problem (4.20) by exploiting constraints in ambiguity set $\mathbb{Q}$.

$$\sup_{\mathbb{P} \in \mathbb{Q}} \mathbb{E}_{\mathbb{P}}[\mathcal{H}(\boldsymbol{y}, \widetilde{\boldsymbol{\omega}})] = \max_{\mathbb{P}} \int_{\Omega} \mathcal{H}(\boldsymbol{y}, \widetilde{\boldsymbol{\omega}}) \mathbb{P}(d\widetilde{\boldsymbol{\omega}}) \tag{4.20a}$$

$$s.t. \quad \int_{\Omega} \widetilde{\boldsymbol{\omega}} \ \mathbb{P}(d\widetilde{\boldsymbol{\omega}}) = \boldsymbol{\mu} \tag{4.20b}$$

$$\int_{\Omega} \mathbb{P}(d\widetilde{\boldsymbol{\omega}}) = 1 \tag{4.20c}$$

Constraints (4.20b)–(4.20c) precisely describe the ambiguity set defined in (4.15). Constraint (4.20b) is an equivalent formulation of the second line in $\mathbb{Q}$ (i.e., $\mathbb{E}_{\mathbb{P}}(\widetilde{\boldsymbol{\omega}}) = \boldsymbol{\mu}$) which defines the mean value of random variables $\widetilde{\boldsymbol{\omega}}$. Constraint (4.20c) ensures that Ω contains all the possible outcomes of $\widetilde{\boldsymbol{\omega}}$. By applying standard duality theory [16], $\sup_{\mathbb{P} \in \mathbb{Q}} \mathbb{E}_{\mathbb{P}}[\mathcal{H}(\boldsymbol{y}, \widetilde{\boldsymbol{\omega}})]$ can be evaluated by solving the dual problem of (4.20) as follows:

$$\min_{\boldsymbol{\lambda}, \eta} \boldsymbol{\mu}^T \boldsymbol{\lambda} + \eta \tag{4.21a}$$

$$s.t. \ \ \boldsymbol{\lambda}^T \widetilde{\boldsymbol{\omega}} + \eta \geqslant \mathcal{H}(\boldsymbol{y}, \widetilde{\boldsymbol{\omega}}) \qquad \forall \widetilde{\boldsymbol{\omega}} \in \Omega \tag{4.21b}$$

where $\boldsymbol{\lambda}$ and η are dual variables associated with primal constraints (4.20*b*) and (4.20*c*),

respectively. We reformulate the problem as (4.22) by incorporating (4.21) in formulation (4.19).

$$\mathcal{Q}_d := \min_{\boldsymbol{y},\boldsymbol{\lambda},\eta} \boldsymbol{a}^T\boldsymbol{y} + \boldsymbol{\mu}^T\boldsymbol{\lambda} + \eta \tag{4.22a}$$

$$s.t.\ \ (4.19b) - (4.19c) \tag{4.22b}$$

$$\eta \geqslant \mathcal{H}(\boldsymbol{y}, \widetilde{\boldsymbol{\omega}}) - \boldsymbol{\lambda}^T\widetilde{\boldsymbol{\omega}} \qquad \forall \widetilde{\boldsymbol{\omega}} \in \Omega \tag{4.22c}$$

where

$$\mathcal{H}(\boldsymbol{y}, \widetilde{\boldsymbol{\omega}}) = \min_{\boldsymbol{x}} \left\{ \boldsymbol{c}^T\boldsymbol{x} : \boldsymbol{G}\boldsymbol{y} + \boldsymbol{E}\boldsymbol{x} \geqslant \boldsymbol{h},\ \boldsymbol{T}(\widetilde{\boldsymbol{\omega}})\boldsymbol{y} = \boldsymbol{W}\boldsymbol{x} \right\} \tag{4.22d}$$

Note that constraints (4.22c) must be satisfied for all realizations of $\widetilde{\boldsymbol{\omega}}$ over its support Ω. Hence, it is equivalent to the following formulation.

$$\eta \geqslant \max_{\forall \widetilde{\boldsymbol{\omega}} \in \Omega} \left\{ \mathcal{H}(\boldsymbol{y}, \widetilde{\boldsymbol{\omega}}) - \boldsymbol{\lambda}^T\widetilde{\boldsymbol{\omega}} \right\} \tag{4.23}$$

The right-hand side of constraints (4.23) can be rewritten as an inner maximization problem. The derivation is the following.

$$\max_{\forall \widetilde{\boldsymbol{\omega}} \in \Omega} \left\{ \mathcal{H}(\boldsymbol{y}, \widetilde{\boldsymbol{\omega}}) - \boldsymbol{\lambda}^T\widetilde{\boldsymbol{\omega}} \right\} \ = \max_{\forall (\boldsymbol{\gamma},\boldsymbol{\pi}) \in \boldsymbol{\Gamma}, \widetilde{\boldsymbol{\omega}} \in \Omega} \left\{ (\boldsymbol{h} - \boldsymbol{G}\boldsymbol{y})^T\boldsymbol{\gamma} + \boldsymbol{y}^T \big(\sum_{i=1}^{|\widetilde{\boldsymbol{\omega}}|} (\boldsymbol{T}^i)^T \boldsymbol{\pi} \widetilde{\omega}_i \big) - \boldsymbol{\lambda}^T\widetilde{\boldsymbol{\omega}} \right\} \tag{4.24a}$$

$$\boldsymbol{\Gamma} = \begin{cases} \boldsymbol{E}^T\boldsymbol{\gamma} + \boldsymbol{W}^T\boldsymbol{\pi} \leqslant \boldsymbol{c} \\ \boldsymbol{\gamma} \geqslant \boldsymbol{0} \end{cases} \tag{4.24b}$$

where $\boldsymbol{\gamma} \in \mathbb{R}^{M_2}$ and $\boldsymbol{\pi} \in \mathbb{R}^{M_3}$ are dual variables associated with constraints (4.19e) and (4.19f), respectively. $\boldsymbol{\Gamma}$ denotes the feasible domain of the dual variables. For fixed $\boldsymbol{y}$ and $\boldsymbol{\lambda}$, the objective function (4.24a) contains bilinear terms $\boldsymbol{\pi}\widetilde{\omega}_i$. The literature presents several methods to solve robust optimization (RO) models with bilinear terms in the inner (sub-) problem, including heuristics [114] and MIP reformulations [79,109,118]. The former finds local optima for two-stage robust problems for which the uncertainty set is a general polyhedron (e.g., non-convex regular polyhedra [49]). The latter finds exact solutions for RO problems by exploiting the special structure of the uncertainty set. A recent work by

Zhao and Zeng [121] develops an exact algorithm for two-stage RO problems for which the uncertainty set is a general polyhedron. The authors derive an equivalent MIP formulation for the inner problem by using the strong Karush–Kuhn–Tucker (KKT) conditions. However, this MIP formulation can be challenging to solve when binary variables are introduced to linearize complementary slackness constraints. Hence, it is challenging to derive exact solutions for RO models for which the uncertainty set is a general polyhedron. Thus, we leave the exploration of exact solution methods as future work. In this research, we focus on generating a lower bound for reformulation $\mathcal{Q}^d$ described in (4.22).

From formulation (4.24), we observe that $\widetilde{\boldsymbol{\omega}}$ only appears in the objective function (4.24a), thus different realizations of $\widetilde{\boldsymbol{\omega}}$ do not affect the feasible region of the dual variables, $\boldsymbol{\Gamma}$ (4.24b). Meanwhile, note that $\boldsymbol{\Gamma}$ is nonempty, since formulation (4.22d) is feasible for any given first-stage solution due to load shedding and over-generation options. Let $(\widehat{\boldsymbol{\pi}}, \widehat{\boldsymbol{\gamma}}) \in \boldsymbol{\Gamma}$ be any feasible dual solution to formulation (4.24). It follows that $\widehat{\boldsymbol{y}}$ and $\widehat{\boldsymbol{\lambda}}$ are given solutions of first-stage variables $\boldsymbol{y}$ and $\boldsymbol{\lambda}$, respectively. Hence, for fixed $\boldsymbol{y}$, $\boldsymbol{\lambda}$, $\boldsymbol{\pi}$ and $\boldsymbol{\gamma}$, the maximum value of (4.24a) equals the optimal objective value of the following *linear programming* (LP) formulation:

$$\max_{\forall \widetilde{\boldsymbol{\omega}} \in \Omega} \Big\{ (\boldsymbol{h} - \boldsymbol{G}\widehat{\boldsymbol{y}})^T \widehat{\boldsymbol{\gamma}} + \widehat{\boldsymbol{y}}^T \big(\sum_{i=1}^{|\widetilde{\boldsymbol{\omega}}|} (\boldsymbol{T}^i)^T \widehat{\boldsymbol{\pi}} \widetilde{\omega}_i \big) - \widehat{\boldsymbol{\lambda}}^T \widetilde{\boldsymbol{\omega}} \Big\} \tag{4.25}$$

Based on LP geometry [16, 22], since Ω is a bounded and nonempty polyhedron (i.e., $\Omega := \{\widetilde{\boldsymbol{\omega}} \in \mathbb{R}^2 : \boldsymbol{D}\widetilde{\boldsymbol{\omega}} \leqslant \boldsymbol{d}\}$), there exists an optimal (worst-case) solution of $\widetilde{\boldsymbol{\omega}}$ which is an extreme point of Ω. Further, we note that the worst-case $\widetilde{\boldsymbol{\omega}}$ is not required to be a vertex of Ω in some special cases. For example, if $\boldsymbol{y} = \boldsymbol{0}$ and $\boldsymbol{\lambda} = \boldsymbol{0}$, then the worst-case $\widetilde{\boldsymbol{\omega}}$ could be any feasible value in Ω (i.e., the optimal solution of $\widetilde{\boldsymbol{\omega}}$ is not unique).

Remark 4.2.1. *Given that Ω is bounded and nonempty. Then, for any given first-stage decision $\boldsymbol{y}$ and $\boldsymbol{\lambda}$, there exists an optimal (worst-case) solution of $\widetilde{\boldsymbol{\omega}}$ which is an extreme point of Ω.*

Based on remark 4.2.1 and the above discussion, we derive a MIP formulation by introducing binary variables associated with each extreme point of Ω. The formulation is desribed in the following form.

$$\mathcal{Q}_v := \min_{\boldsymbol{y},\boldsymbol{\lambda},\eta} \boldsymbol{a}^T\boldsymbol{y} + \boldsymbol{\mu}^T\boldsymbol{\lambda} + \eta \tag{4.26a}$$

$$s.t.\ \ (4.19b) - (4.19c) \tag{4.26b}$$

where

$$\eta \geqslant \max_{\boldsymbol{\gamma},\boldsymbol{\pi},\widetilde{\boldsymbol{\omega}}} (\boldsymbol{h} - \boldsymbol{G}\boldsymbol{y})^T\boldsymbol{\gamma} + \boldsymbol{y}^T\big(\sum_{i=1}^{|\widetilde{\boldsymbol{\omega}}|}\sum_{j=1}^{|\mathcal{K}|}(\boldsymbol{T}^i)^T\boldsymbol{\zeta}_j\widetilde{\omega}_{ij}^*\big) - \boldsymbol{\lambda}^T\widetilde{\boldsymbol{\omega}} \tag{4.26c}$$

$$s.t.\ \boldsymbol{E}^T\boldsymbol{\gamma} + \boldsymbol{W}^T\boldsymbol{\pi} \leqslant \boldsymbol{c} \tag{4.26d}$$

$$\boldsymbol{\gamma} \geqslant \boldsymbol{0} \tag{4.26e}$$

$$\zeta_{jl} \in \langle \beta_j,\ \pi_l \rangle^{MC} \qquad \forall j \in \{1,...,|\mathcal{K}|\},\ \forall l \in \{1,...,M_3\} \tag{4.26f}$$

$$\widetilde{\boldsymbol{\omega}} = \sum_{j=1}^{|\mathcal{K}|} \beta_j\widetilde{\boldsymbol{\omega}}_j^* \tag{4.26g}$$

$$\sum_{j=1}^{|\mathcal{K}|} \beta_j = 1 \tag{4.26h}$$

$$\beta_j \in \{0,1\}, \qquad \forall j \in \{1,...,|\mathcal{K}|\} \tag{4.26i}$$

where $\mathcal{K}$ is the set of vertexes (denoted as $\widetilde{\boldsymbol{\omega}}^*$) of the uncertainty set Ω and $\widetilde{\omega}_{ij}^*$ represents the j^{th} extreme point in $\mathcal{K}$. β_j are binary variables used to control the selection of an extreme point $\widetilde{\boldsymbol{\omega}}_j^*$. $\boldsymbol{\zeta}_j \in \mathbb{R}^{M_3}$ are continuous variables introduced for linearizing bilinear products $\beta_j\boldsymbol{\pi}$ via McCormick Relaxations. Note that this linearization is exact due to $\beta_j \in \{0,1\}$ [83]. The underlying idea of this MIP model is that we only consider the extreme points of Ω as candidate solutions for $\widetilde{\boldsymbol{\omega}}$. Hence, for any given first-stage decision $(\boldsymbol{y},\boldsymbol{\lambda})$, the resulting worst-case $\widetilde{\boldsymbol{\omega}}$ will be a vertex of Ω.

Proposition 4.2.2. *The worst-case expected total cost obtained from formulation $\mathcal{Q}_v$ is a lowed bound to the reformulated two-stage DR-OTSGMD problem $\mathcal{Q}_d$.*

Proof. Let $\mathfrak{Q}_d^*$ and $\mathfrak{Q}_v^*$ be the optimal objective values to formulations $\mathfrak{Q}_d$ and $\mathfrak{Q}_v$, respectively. η_d^* and η_v^* represent the optimal values of η to models $\mathfrak{Q}_d$ and $\mathfrak{Q}_v$, respectively. Since $\mathcal{K}$ represents the vertexes of Ω, then $\mathcal{K} \subseteq \Omega$ and the following holds:

$$\max_{\forall \widetilde{\boldsymbol{\omega}} \in \Omega} \left\{ \mathcal{H}(\boldsymbol{y}, \widetilde{\boldsymbol{\omega}}) - \boldsymbol{\lambda}^T \widetilde{\boldsymbol{\omega}} \right\} \geqslant \max_{\forall \widetilde{\boldsymbol{\omega}} \in \mathcal{K}} \left\{ \mathcal{H}(\boldsymbol{y}, \widetilde{\boldsymbol{\omega}}) - \boldsymbol{\lambda}^T \widetilde{\boldsymbol{\omega}} \right\} \tag{4.27}$$

As a result, for any given first-stage decisions $\boldsymbol{y}$ and $\boldsymbol{\lambda}$, the following is true: $\boldsymbol{a}^T \boldsymbol{y} + \boldsymbol{\mu}^T \boldsymbol{\lambda} + \eta_d^* \geqslant \boldsymbol{a}^T \boldsymbol{y} + \boldsymbol{\mu}^T \boldsymbol{\lambda} + \eta_v^*$ (see constraints (4.22c) and (4.26c)), i.e., $\mathfrak{Q}_v^* \leqslant \mathfrak{Q}_d^*$. □

Proposition 4.2.3. *Solving formulation $\mathfrak{Q}_v$ yields a lower bound of the worst-case expected total cost to the two-stage DR-OTSGMD problem $\mathfrak{Q}_o$.*

Proof. Let $\mathfrak{Q}_o^*$, $\mathfrak{Q}_d^*$, and $\mathfrak{Q}_v^*$ be the optimal objective function values of formulations $\mathfrak{Q}_o$, $\mathfrak{Q}_d$, and $\mathfrak{Q}_v$, respectively. As described in Section 4.2.3, $\mathfrak{Q}_d$ is a linear approximation of $\mathfrak{Q}_o$. Hence, $\mathfrak{Q}_d$ yields a lower bound for $\mathfrak{Q}_o$, i.e., $\mathfrak{Q}_d^* \leqslant \mathfrak{Q}_o^*$. Further, $\mathfrak{Q}_v^* \leqslant \mathfrak{Q}_d^*$ based on proposition 4.2.2. Thus, $\mathfrak{Q}_v^* \leqslant \mathfrak{Q}_d^* \leqslant \mathfrak{Q}_o^*$. □

4.3 Solution Methodology: A column-and-constraint generation algorithm

To solve the proposed two-stage DR-OTSGMD problem, we use the column-and-constraint generation (C&CG) algorithm described in [118]. Similar to Benders' decomposition, the C&CG algorithm is a cutting plane method. It iteratively refines the feasible domain of a problem by sequentially generating a set of recourse variables and their associated constraints. The algorithmic description for the C&CG procedure is presented in Algorithm 4. In this algorithm, we use notation $\mho$ to denote a subset of $\mathcal{K}$. LB and UB represent a lower and an upper bound of formulation (4.26), respectively. ϵ is a sufficiently small positive constant. Lines 3-10 are the main body of the C&CG which describe a cutting plane procedure for the first $\mathfrak{K}$ iterations. In lines 4-5, the LB is evaluated during iteration $\mathfrak{K}$ using the incumbent solution $\widehat{\boldsymbol{y}}^{\mathfrak{K}+1}$, $\widehat{\boldsymbol{\lambda}}^{\mathfrak{K}+1}$ and $\widehat{\eta}^{\mathfrak{K}+1}$. Note that in the initial iteration

($\mathfrak{K} = 0$), set $\mathcal{O}$ is empty and master problem $\mathcal{P}(\cdot)$ lacks constraints (4.28a)-(4.28c). In lines 6-7, the subproblem $\mathcal{Q}(\cdot)$ is solved, UB is estimated, and the worst-case scenario $\widehat{\widetilde{\boldsymbol{\omega}}}^{\mathfrak{K}+1}$ is generated using the incumbent decision $(\widehat{\boldsymbol{y}}^{\mathfrak{K}+1}, \widehat{\boldsymbol{\lambda}}^{\mathfrak{K}+1})$. Line 8 generates a new set of recourse variables $\boldsymbol{x}^{\mathfrak{K}+1}$ and associated constraints (4.30) for $\mathcal{P}(\cdot)$. Note that constraint (4.30a) is valid only if subproblem $\mathcal{Q}(\cdot)$ is bounded (i.e., complete recourse). Indeed, for any given first-stage solution, formulation (4.22d) is feasible due to load shedding and over-generation options. Line 9 expands set $\mathcal{O}$ and adds these newly-generated variables and constraints to the master problem $\mathcal{P}(\cdot)$ to tighten the feasible domain of the first-stage variables (line 4). The process is repeated until the objective values of the upper and lower bound converge (line 3).

Algorithm 4 Column-and-Constraint Generation (C&CG)

1: **function** C&CG
2: Set $\mathfrak{K} \leftarrow 0$, $LB \leftarrow -\infty$, $UB \leftarrow +\infty$, $\mathcal{O} = \varnothing$
3: **while** $\frac{|UB-LB|}{LB} \leqslant \epsilon$ **do**
4: Solve the following master problem

$$\mathcal{P}(\widehat{\widetilde{\boldsymbol{\omega}}} \in \mathcal{O}) = \min_{\boldsymbol{y},\boldsymbol{\lambda},\eta,\boldsymbol{x}} \boldsymbol{a}^T\boldsymbol{y} + \boldsymbol{\mu}^T\boldsymbol{\lambda} + \eta$$

$$s.t.\ \ (4.19b) - (4.19c)$$

$$\eta \geqslant \boldsymbol{c}^T\boldsymbol{x}^l - \boldsymbol{\lambda}^T\widehat{\widetilde{\boldsymbol{\omega}}}^l \qquad \forall l \leqslant \mathfrak{K} \tag{4.28a}$$

$$\boldsymbol{G}\boldsymbol{y} + \boldsymbol{E}\boldsymbol{x}^l \geqslant \boldsymbol{h} \qquad \forall l \leqslant \mathfrak{K} \tag{4.28b}$$

$$\boldsymbol{T}(\widehat{\widetilde{\boldsymbol{\omega}}}^l)\boldsymbol{y} = \boldsymbol{W}\boldsymbol{x}^l \qquad \forall l \leqslant \mathfrak{K} \tag{4.28c}$$

5: Use the optimal solution $\widehat{\boldsymbol{y}}^{\mathfrak{K}+1}$, $\widehat{\boldsymbol{\lambda}}^{\mathfrak{K}+1}$ and $\widehat{\eta}^{\mathfrak{K}+1}$ to calculate $LB \leftarrow \mathcal{P}(\widehat{\widetilde{\boldsymbol{\omega}}} \in \mathcal{O})$
6: Solve

$$\mathcal{Q}(\widehat{\boldsymbol{y}}^{\mathfrak{K}+1}, \widehat{\boldsymbol{\lambda}}^{\mathfrak{K}+1}) = \max_{\boldsymbol{\gamma},\boldsymbol{\pi},\widetilde{\boldsymbol{\omega}}} (\boldsymbol{h} - \boldsymbol{G}\widehat{\boldsymbol{y}}^{\mathfrak{K}+1})^T\boldsymbol{\gamma} + (\widehat{\boldsymbol{y}}^{\mathfrak{K}+1})^T\Big(\sum_{i=1}^{|\widetilde{\boldsymbol{\omega}}|}\sum_{j=1}^{|\mathcal{K}|}(\boldsymbol{T}^i)^T\boldsymbol{\zeta}_j\widetilde{\omega}_{ij}^*\Big) - (\widehat{\boldsymbol{\lambda}}^{\mathfrak{K}+1})^T\widetilde{\boldsymbol{\omega}} \tag{4.29a}$$

$$s.t.\ \ (4.26d) - (4.26i)$$

7: Use the optimal solution $\widehat{\widetilde{\boldsymbol{\omega}}}^{\mathfrak{K}+1}$ to calculate $UB \leftarrow LB - \widehat{\eta}^{\mathfrak{K}+1} + \mathcal{Q}(\widehat{\boldsymbol{y}}^{\mathfrak{K}+1}, \widehat{\boldsymbol{\lambda}}^{\mathfrak{K}+1})$
8: Generate a new set of recourse variables $\boldsymbol{x}^{\mathfrak{K}+1}$ and the following constraints for $\mathcal{P}(\cdot)$

$$\eta \geqslant \boldsymbol{c}^T\boldsymbol{x}^{\mathfrak{K}+1} - \boldsymbol{\lambda}^T\widehat{\widetilde{\boldsymbol{\omega}}}^{\mathfrak{K}+1} \tag{4.30a}$$

$$\boldsymbol{G}\boldsymbol{y} + \boldsymbol{E}\boldsymbol{x}^{\mathfrak{K}+1} \geqslant \boldsymbol{h} \tag{4.30b}$$

$$\boldsymbol{T}(\widehat{\widetilde{\boldsymbol{\omega}}}^{\mathfrak{K}+1})\boldsymbol{y} = \boldsymbol{W}\boldsymbol{x}^{\mathfrak{K}+1} \tag{4.30c}$$

9: Update $\mathcal{O} \leftarrow \mathcal{O} \bigcup \widehat{\widetilde{\boldsymbol{\omega}}}^{\mathfrak{K}+1}$ and $\mathfrak{K} \leftarrow \mathfrak{K} + 1$
10: **end while**
11: **return** $\widehat{\boldsymbol{y}}^{\mathfrak{K}}$
12: **end function**

Note that the optimal solution of the reformulation (4.26) can be obtained by enumerating all the possible uncertain scenarios (vertexes) in $\mathcal{K}$. However, full enumeration is computationally intractable when subset $\mathcal{K}$ is large. One advantage of the C&CG is that the computational efforts could be significantly reduced by a partial enumeration of non-trivial scenarios of the random variables $\tilde{\boldsymbol{\omega}}$. Additionally, the C&CG algorithm is known to converge in a finite number of iterations since the number of extreme points in $\mathcal{K}$ is finite [121].

4.4 Case Study

This section analyzes the performance of a power system when exposed to uncertain geo-electric fields induced by GMDs. We use a modified version of the Epri21 system [3]. Its size is comparable to a previous work [123] that considered minimization of the quasi-static GICs and did not consider ACOPF with topology control. Computational experiments were performed using the HPC Palmetto cluster at Clemson University with Intel Xeon E5-2665, 24 cores and 120GB of memory. All implementations are completed using Julia/JuMP [36]. All cases are solved using CPLEX 12.7.0 (default options).

4.4.1 Data Collection and Analysis

The main source of data about GMDs is a recent work by Woodroffe *et al.* [113]. The authors analyzed a 100-year of data related to storms and indicate that the magnitude of the corresponding induced geo-electric fields varies with the magnetic latitudes. The authors also categorized geomagnetic storms into three classes, strong, severe and extreme, according to the range of geoelectromagnetic disturbances (Dst). Table 4.1 summaries a set of parameters used for describing the uncertain electric fields induced by GMDs. In this table, $\overline{\nu}^M$ denotes the maximum amplitude of geo-electric fields induced by GMDs (see Section 4.2.4). Its value is obtained by the upper bound of a 95% confidence interval (CI) of a 100-year peak GMD magnitude presented in Woodroffe *et al.* [113] (Table 1-3 in [113]

). The values of μ^N and μ^E are estimated via extreme value analysis of electric fields from 15 geomagnitude storms using a Generalized Extreme Value Distribution model for both northward and eastward components (i.e., $\widetilde{\nu}^N$ and $\widetilde{\nu}^E$). In addition, it is important to notice

Table 4.1: Peak GMD amplitudes for geomagnetic storms with different magnetic latitudes based on 100 years of historical data. μ^E and μ^N are the mean values of geo-electric fields in the eastward and northward directions. MLAT denotes the geomagnetic latitude. Dst represents geoelectromagnetic disturbances.

	$\overline{\nu}^M$ (μ^N, μ^E) (V/km)		
MLAT	Strong ($-100nT \geqslant Dst > -200nT$)	Severe ($-200nT \geqslant Dst > -300nT$)	Extreme ($-300nT \geqslant Dst$)
40°–45°	1.6 (0.9, 0.8)	2.0 (0.9, 0.8)	3.5 (1.1, 0.9)
45°–50°	1.2 (0.7, 0.7)	1.6 (0.8, 0.7)	3.5 (1.5, 1.3)
50°–55°	3.5 (2.1, 1.8)	5.0 (2.5, 2.1)	6.0 (3.1, 2.7)
55°–60°	11.5 (6.6, 5.6)	6.6 (3.7, 3.1)	9.1 (4.2, 3.6)
60°–65°	6.6 (5.0, 4.3)	6.6 (4.3, 3.6)	12.7 (5.9, 5.1)
65°–70°	8.8 (6.1, 5.2)	8.8 (5.3, 4.5)	10.6 (5.8, 4.9)
70°–75°	7.7 (5.1, 4.3)	6.3 (3.9, 3.3)	16.1 (6.8, 5.8)

that latitudes in Table 4.1 are relative to a magnetic coordinate system which usually differs from the corresponding values in the geographic system. Hence, the magnetic latitudes should be converted to corresponding latitudes in a geographic system, and vice versa. In this research, we convert the *geographic latitudes* of substations in a power system to their corresponding *magnetic latitudes* using the transformation method described in Appendix A. After transformation, the MLAT of the Epri21 system is between $55^\circ - 60^\circ$.

Tables 4.2–4.4 present problem parameters that we derived for this modified Epri21 case. We consider that this system is located in Quebec, Canada in order to use the corresponding geographic location. We consider that cost of shedding/over-generating load is ten times of the most expensive generation cost; and the fuel cost coefficients of additional real-power generation (i.e., Δ_i) is 20% more than the reserved generation prior to a storm.

Table 4.2: (a) Transformer winding resistance and k are estimated based on the test cases provided in [6, 58]. (b) The nominal line length for the Epri21 system [3] is used to derive an approximate geospatial layout of the power system nodes

.

(a) Transformer data

Name	Type	Resistance W1(Ohm)	Bus No.	Resistance W2(Ohm)	Bus No.	Line No.	k (p.u.)
T 1	wye-delta	0.1	1	0.001	2	16	1.2
T 2	Gwye-Gwye	0.2	4	0.1	3	17	1.6
T 3	Gwye-Gwye	0.2	4	0.1	3	18	1.6
T 4	Auto	0.04	3	0.06	4	19	1.6
T 5	Auto	0.04	3	0.06	4	20	1.6
T 6	Gwye-Gwye	0.04	5	0.06	20	21	1.6
T 7	Gwye-Gwye	0.04	5	0.06	20	22	1.6
T 8	GSU	0.15	6	0.001	7	23	0.8
T 9	GSU	0.15	6	0.001	8	24	0.8
T 10	GSU	0.1	12	0.001	13	25	0.8
T 11	GSU	0.1	12	0.001	14	26	0.8
T 12	Auto	0.04	16	0.06	15	27	1.1
T 13	Auto	0.04	16	0.06	15	28	1.1
T 14	GSU	0.1	17	0.001	18	29	1.2
T 15	GSU	0.1	17	0.001	19	30	1.2

(b) Transmission line data

Line	From Bus	To Bus	Length (km)
1	2	3	122.8
2	4	5	162.1
3	4	5	162.1
4	4	6	327.5
5	5	6	210.7
6	6	11	97.4
7	11	12	159.8
8	15	4	130.0
9	15	6	213.5
10	15	6	213.5
11	16	20	139.2
12	16	17	163.2
13	17	20	245.8
14	17	2	114.5
15	21	11	256.4

Table 4.3: (a) The substation grounding resistance GR is estimated from typical values of grounding resistance of substations provided in [80]. (b) The original line parameters r_e^o and x_e^o are scaled by the ratio β_e of the new to original line lengths.

(a) Substation data

Name	Latitude	Longitude	GR(Ohm)
SUB 1	46.61	-77.87	0.20
SUB 2	47.31	-76.77	0.20
SUB 3	46.96	-74.68	0.20
SUB 4	46.55	-76.27	1.00
SUB 5	45.71	-74.56	0.10
SUB 6	46.38	-72.02	0.10
SUB 7	47.25	-72.09	0.22
SUB 8	47.20	-69.98	0.10

(b) Other parameters

κ_i^+	\$ 1000 /MW (or MVar)
κ_i^-	\$ 1000 /MW (or MVar)
$\underline{v}_i$	0.9 p.u.
$\overline{v}_i$	1.1 p.u.
c_i^{R1}	$120\% c_i^1$
c_i^{R2}	$120\% c_i^2$
$\overline{I}_e^a$	$T_e / \min\{\underline{v}_i, \underline{v}_j\}$
r_e	$(\beta_e) r_e^o$
x_e	$(\beta_e) x_e^o$
$\overline{\theta}$	30°

Table 4.4: Generator Data

Name	Bus No.	$\underline{gp}$ (MW)	$\overline{gp}$ (MW)	$\underline{gq}$ (MVar)	$\overline{gq}$ (MVar)	c^2, c^1, c^0 (\$)
G 1	1	200	1000	-350	500	0.11, 5, 60
G 2	7	180	900	-350	400	0.11, 5, 60
G 3	8	180	900	-350	400	0.11, 5, 60
G 4	13	100	500	-200	225	0.11, 5, 60
G 5	14	100	500	-200	225	0.11, 5, 60
G 6	18	160	800	-300	400	0.11, 5, 60
G 7	19	160	800	-300	400	0.11, 5, 60

4.4.2 Experimental Results

To evaluates the performance of the Epri21 system under the influence of uncertain geomagnetic storms, we consider three different storm levels described in Table 4.1: extreme, severe and strong. We assume that generator ramping limits change from 0% to 30% of its maximum real power generation ($\overline{gp}$) in 5% steps. To analyze the benefits of capturing uncertain events via the DR optimization, we study the following four cases:

1. C0: The ACOTS with GIC effects induced by the mean geo-electric fields (i.e., μ^E and μ^N):
   $M_{mean} := \text{Min}\left\{\boldsymbol{a}^T\boldsymbol{y} + \boldsymbol{c}^T\boldsymbol{x}\text{: (4.19b)-(4.19c), (4.19e)-(4.19f); } \tilde{\boldsymbol{\omega}} = [\nu^E, \nu^N]^T\right\} \Leftrightarrow \boldsymbol{y}^*_{mean}, \mathfrak{C}^*_{mean}$

2. C1: The two-stage DR-OTSGMD:
   $M_{dr} := \text{Min}\Big\{\text{(4.26a): (4.26b)-(4.26i)}\Big\} \Leftrightarrow \boldsymbol{y}^*_{dr}, \mathfrak{C}^*_{dr}$

3. C2: The two-stage DR-OTSGMD with fixed topology configuration and generator setpoints:
   $M_{fm} := \text{Min}\Big\{\text{(4.26a): (4.26b)-(4.26i); } \boldsymbol{y} = \boldsymbol{y}^*_{mean}\Big\} \Leftrightarrow \boldsymbol{y}^*_{mean}, \mathfrak{C}^*_{fm}$

4. C3: The two-stage DR-OTSGMD with fixed topology configuration:
   $M_{ft} := \text{Min}\Big\{\text{(4.26a): (4.26b)-(4.26i); } y_i = 1\ \forall i \in \{1, ..., |\mathcal{E}^a|\}\Big\} \Leftrightarrow \boldsymbol{y}^*_{ft}, \mathfrak{C}^*_{ft}$

where M_α is the optimization model for case α; $\boldsymbol{y}^*_\alpha$ and $\mathfrak{C}^*_\alpha$ represent the optimal first-stage decisions and objective function value, respectively. The values of $\boldsymbol{y}^*_\alpha$ and $\mathfrak{C}^*_\alpha$ are obtained by solving M_α. Case C0 identifies the optimal first-stage decisions $\boldsymbol{y}^*_{mean}$ (i.e., generation and topology) and evaluates the objective $\mathfrak{C}^*_{mean}$ according to the mean geo-electric fields (V/km) in the northward and eastward directions. Case C1 identifies a solution for the two-stage DR-OTSGMD model assuming uncertain GMDs. Case C2 finds a solution to the worst-case expected cost $\mathfrak{C}^*_{fm}$ of the DR optimization model using the generation and topology decisions of Case C0. Finally, Case C3 is similar to Case C1, but topology reconfiguration is not allowed.

4.4.2.1 Case C0: GIC mitigation for the mean geo-electric fields

Case C0 assumes that power system operators use the mean value of a storm level (i.e., strong, severe and extreme) to optimize power generation and system topology. It is

assumed that the induced northward and eastward geo-electric fields equal the corresponding mean values μ^N and μ^E, respectively. In Table 4.5, we summarize the computational results for Case C0 under different storm levels and ramping limits. The results suggest that the cost of mitigating the impacts of a storm decreases as ramping limits increase. The highest cost occurs when generator ramping in not allowed (i.e., $\overline{u}_i^R = 0$). This is the reason why increasing ramping limits from 0 to 30% leads to a 66.1% cost decrease for strong GMD events. Additionally, the total cost varies with storm levels; increasing the intensity of geoelectirc field induced by a storm results in higher cost. Costs increase with storm level; however, this increase is not significant, mainly because the cost changes due to generator dispatch are small. For example, the cost difference between strong and severe storms is only 0.29% when ramping limits equal 10%.

Table 4.5: Computational results for Case C0 with respect to different storm levels (SL) and ramping limits ($\overline{u}_i^R$). TC denotes the minimum total cost for generator dispatch and load shedding. μ^E and μ^N are the mean values of geo-electric fields for northward and eastward components, respectively. $\boldsymbol{z}^*$ represents the optimal line switching decisions.

SL(55°–60°)	$\overline{u}_i^R$ (%)	TC ($)	μ^E, μ^N (V/km)	$\boldsymbol{z}^*$	Wall Time (sec)
Strong	0	379,209	5.6, 6.6	13, 15, 18, 21, 22	261
	5	341,199	5.6, 6.6	13, 15, 17, 21, 22	276
	10	307,682	5.6, 6.6	13, 15, 18, 21, 22	243
	15	280,176	5.6, 6.6	13, 15, 18, 21, 22	244
	20	257,539	5.6, 6.6	13, 15, 17, 21, 22	99
	25	240,465	5.6, 6.6	13, 15, 20, 21, 22	262
	30	228,336	5.6, 6.6	13, 15, 18, 21, 22	251
Severe	0	379,177	3.1, 3.7	13, 15, 17, 18, 21, 22	85
	5	341,167	3.1, 3.7	13, 15, 18, 21, 22	254
	10	306,794	3.1, 3.7	13, 15, 17, 18, 21, 22	106
	15	280,149	3.1, 3.7	13, 15, 17, 18, 21, 22	262
	20	257,513	3.1, 3.7	13, 15, 17, 18, 21, 22	268
	25	240,394	3.1, 3.7	13, 15, 17, 18, 21, 22	197
	30	227,872	3.1, 3.7	13, 15, 17, 18, 21, 22	263
Extreme	0	379,181	3.6, 4.2	13, 15, 17, 18, 21, 22	267
	5	341,171	3.6, 4.2	13, 15, 17, 21, 22	273
	10	307,654	3.6, 4.2	13, 15, 17, 18, 21, 22	284
	15	280,152	3.6, 4.2	13, 15, 17, 18, 21, 22	297
	20	257,516	3.6, 4.2	13, 15, 18, 21, 22	274
	25	240,445	3.6, 4.2	13, 15, 17, 18, 21, 22	204
	30	228,316	3.6, 4.2	13, 15, 18, 21, 22	266

4.4.2.2 Case C1: DR optimization for GIC mitigation under uncertainty

In Case C1, uncertain GMD events are modeled via an ambiguity set which represents the probability distributions of geo-electric field properties (see Section 4.2.4). The proposed outer approximation of Ω consists of 90 linear cuts. This results in 90 extreme points, and consequently, 90 distinct values of $\widetilde{\boldsymbol{\omega}}$ (i.e., $|\mathcal{K}| = 90$) which are evaluated in formulation (4.26). Similar to Case C0, we conduct sensitivity analysis with respect to storm levels and ramping limits. Table (4.6) summarizes these computational results. The results show that, similar to Case C0, the worst-case expected total cost (WETC) decreases as the ramping limits increase. This decrease is as large as 57.2% for a strong storm (i.e., $\overline{u}_i^R = 30\%$ versus $\overline{u}_i^R = 0\%$).

Table 4.6: Computational results for Case C1 with respect to different strom levels (SL) and ramping limits ($\overline{u}_i^R$). WETC denotes the worst-case expected total cost. $\widetilde{\nu}^{*E}$, $\widetilde{\nu}^{*N}$ represent the worst-case geo-electric fields for eastward and northward components, respectively. $\boldsymbol{z}^*$ represents the optimal line switching decisions.

SL(55°–60°)	$\overline{u}_i^R$ (%)	WETC ($)	$\widetilde{\nu}^{*E}$, $\widetilde{\nu}^{*N}$ (V/km)	$\boldsymbol{z}^*$	Wall Time (sec)
Strong	0	454,447	8.1, 8.1	2, 3, 15, 17–20, 22, 27, 28	5,264
	5	401,735	8.1, 8.1	1, 2, 9, 10, 15, 17–22, 28	6,758
	10	369,019	8.1, 8.1	1, 2, 9, 10, 15, 17–22, 28	7,950
	15	340,884	8.1, 8.1	1, 2, 9, 10, 15, 17–22, 27	5,808
	20	318,382	8.1, 8.1	1, 2, 9, 10, 15, 17–22, 27	6,152
	25	301,321	8.1, 8.1	1, 2, 9, 10, 15, 17–22, 27	5,637
	30	288,987	8.1, 8.1	1, 2, 9, 10, 15, 17–22, 28	7,804
Severe	0	379,294	4.7, 4.7	15, 17, 19, 27, 28	2,324
	5	341,280	4.7, 4.7	15, 17, 19, 20, 27, 28	1,264
	10	307,760	4.7, 4.7	15, 19, 20, 27, 28	2,077
	15	280,246	4.7, 4.7	15, 19, 20, 27, 28	905
	20	257,605	4.7, 4.7	15, 17, 20, 27, 28	535
	25	240,528	4.7, 4.7	15, 17, 19, 27, 28	417
	30	228,394	4.7, 4.7	15, 19, 20, 27, 28	3,496
Extreme	0	379,586	7.1, 5.7	2, 8, 18–20, 21, 27, 28	4,605
	5	341,564	7.1, 5.7	2, 8, 18–20, 21, 27, 28	2,114
	10	308,031	7.1, 5.7	2, 8, 18–20, 21, 27, 28	4,468
	15	280,486	7.1, 5.7	2, 8, 17, 19, 20, 22, 27, 28	2,266
	20	257,826	7.1, 5.7	2, 8, 17, 19, 20, 21, 27, 28	2,932
	25	240,743	7.1, 5.7	2, 8, 17, 20, 21, 27, 28	1,426
	30	228,590	7.1, 5.7	2, 8, 17, 19, 20, 22, 27, 28	3,172

Moreover, we observe that, for a given storm level, the worst-case geo-electric field remains the same at different ramping limits. For example, in extreme storm, $\widetilde{\nu}^{*E}$ and $\widetilde{\nu}^{*N}$ always equal 7.1 and 5.7 V/km, respectively. This indicates that, for a given storm level, the worst scenario for the system is always due to the same extreme point of Ω. In addition, the difference in the WETC between strong and extreme (and severe) events is considerable. For example, the cost difference between strong and severe events is 19.8% when $\overline{u}_i^R = 0$. Table 4.7 reports the amount and percentage of the WETC due to load shedding. The results suggest that, for Case C1 the increase in WETC under a strong event is primarily due to changes in load shedding. For example, no load shedding is observed for any ramping limit in severe storms. However, in the case of strong storms, an average 16.94% of the WETC on average is due to load shedding.

4.4.2.3 Case Comparisons: Cost Benefits of the DR optimization

Figure 4.2 summarizes the total cost $\mathfrak{C}^*$ for all cases defined in Section (4.4.2). The DR optimization model results in higher costs for all problems solved. These costs are highest when the storm level is strong. Tables 4.5 and 4.6 suggest that the computation time required for solving Case C1 are higher than Case C0. Hence, modeling uncertainty in geo-electric fields results in a significant increase in computational efforts, but it also provides significant cost savings over the deterministic model which ignores uncertainty.

The cost benefits of the DR optimization can be evaluated by comparing Case C1 with C2. Similar to Case C1, the worst-case expected cost of Case C2 decreases as ramping limits increase. For all storm levels, the cost benefits of the DR-OTSGMD vary with ramping limits. The differences in cost are statistically significant. For example, when a strong storm is exposed, the cost savings are as much as 122.12% (i.e., $(\mathfrak{C}^*_{fm} - \mathfrak{C}^*_{dr})/\mathfrak{C}^*_{dr}$). This is because the generation and topology decisions in Case C1 are determined by the DR model; however, these decisions for Case C2 are fixed to Case C0.

We also compare Case C1 with C3 to evaluate the performance of network reconfiguration. The results displayed in Figure 4.2 suggest that line switching decisions could

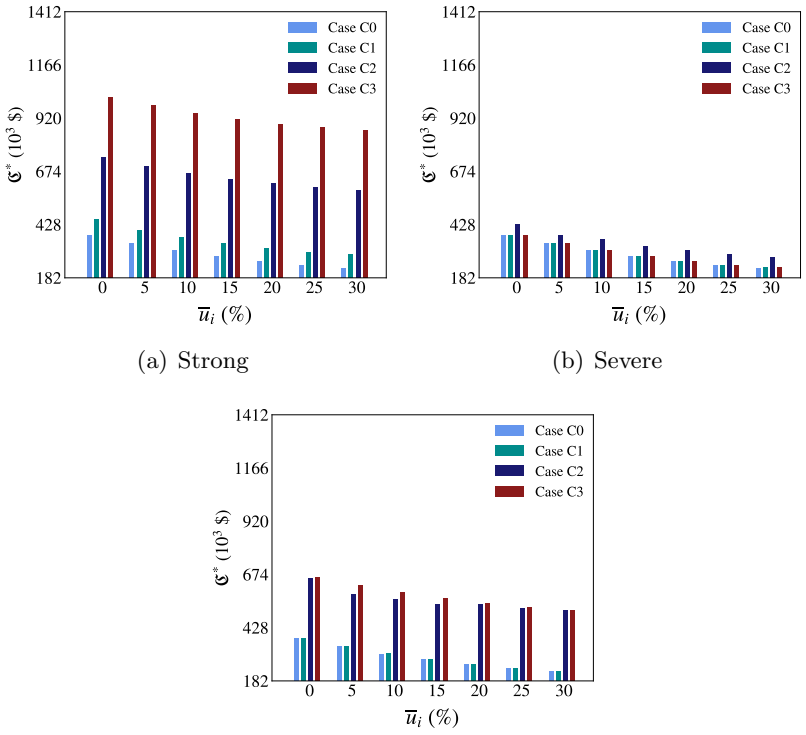

(a) Strong

(b) Severe

(c) Extreme

Figure 4.2: Cost comparisons among all cases.

significantly lower the cost of GIC mitigation under uncertainty, in particular for strong and extreme storms. For example, Figure 4.2(a) shows that the WETC is higher than Case C2 and has significantly increased when line switching is not allowed in the two-stage DR-OTSGMD model. Notice that when $\overline{u}_i^R = 10\%$, the cost increase in Case C3 as compared to C1 is 206.4% and the increase in cost in Case C2 as compared to C1 is 116.5%.

Table 4.7 demonstrates the impacts of load shedding on cost. The results indicate that the cost differences between any two cases are primarily because of load shedding. For example, in the case of extreme storms, the total cost of Case C2 is much higher than Case C1. This is due to the fact that the topology control in Case C1 enables all of the load to be served. In contrast, the fixed topology in Case C2 results in a load shedding cost of 39.28% on average. Similarly, for severe storms, load shedding is observed only in Case C2. As a consequence, Case C2 yields the highest cost in comparison to the other three cases.

Table 4.7: Load shedding costs for all cases. The average (Avg.), minimum (Min.), maximum (Max.) and the standard deviation (Std.) of load shedding cost (LSC) are computed over ramping limits from 0% – 30%. For Case C1, C2 and C3, LSC is associated with the worst-case geo-electric fields. Solutions displayed in parentheses denote the percentage of the total cost ($\mathfrak{C}^*$) due to load shedding. "-" indicates that no load shedding is observed.

		LSC(% of the $\mathfrak{C}^*$)			
SL(55°–60°)	Case	Avg.	Min.	Max.	Std.
Strong	C0	-	-	-	-
	C1	59,995 (16.94)	53,289 (13.73)	94,839 (20.87)	15,377 (2.40)
	C2	243,842 (37.78)	242,923 (33.05)	244,951 (41.34)	923 (3.10)
	C3	421,148 (45.58)	420,558 (41.48)	421,569 (48.68)	367 (2.64)
Severe	C0	-	-	-	-
	C1	-	-	-	-
	C2	113 (0.03)	71 (0.02)	121 (0.04)	19 (0.01)
	C3	-	-	-	-
Extreme	C0	-	-	-	-
	C1	-	-	-	-
	C2	182,874 (33.05)	158,603 (28.33)	191,813 (37.78)	14,605 (4.00)
	C3	223,739 (39.28)	216,536 (34.37)	227,672 (42.39)	4,940 (3.06)

4.5 Conclusions and Future Research

In this chapter, we propose a two-stage DR-OTSGMD formulation for solving OTS problems that take into account reactive power consumption induced by uncertain geo-electric fields. We construct an ambiguity set to characterize a set of probability distributions of the geo-electric fields, and aim to minimize the worst-case expected total cost over all geo-electric field distributions defined in the ambiguity set. Since the proposed DR formulation is intractable, we derive a reformulation that leads to a decomposition framework for solving our problem based on the C&CG algorithm. We prove that that solving this reformulation yields a lower bound of the original proposed DR model. The case studies based on the modified Epri21 system show that considering the uncertainty of the GMD-induced geo-electric field is crucial and the DR optimization method is an effective approach to deal with this uncertainty.

There remain a number of future directions. For example, considering additional moment information, such as the variations of random variables, could enhance the modeling

of the ambiguity set. Additionally, improving the proposed algorithm is necessary for solving large-size instances. Another potential extension is to extending the formulation to integrate N-1 security (contingency) constraints in order to increase the resiliency of transmission systems under GMD extreme events.

Chapter 5

Conclusions and Future Research

An electric power system consists of various components that generate and deliver large amounts of electricity from distant sources to demanding consumers. Given the rapid growth in electricity demand, the cost-effective utilization of power utilities while providing reliable accessibility is extremely important. The alternating current optimal power flow (ACOPF) problem is one of the most fundamental optimization problems for identifying the economic and reliable operations of electric power systems. Solving the ACOPF problem for large-sized systems is computationally challenging because of the complexities imposed by nonlinear and non-convex AC physics. In the first phase of this dissertation, we focus on developing computationally efficient approaches for the ACOPF problem in order to improve power dispatch efficiency, as this could significantly save generation cost each year.

Next, we shift our study to the impacts of geomagnetic disturbances (GMDs) on electrical power systems. GMDs, casued by solar storms, create geo-electric fields which then induce quadi-DC currents (GICs) in grounded sections of power system networks. GICs can saturate transformers, resulting in hot-spot heating and reactive power consumption which can severely impact the ability of a power system to deliver power. To address this security issue, we develop a mixed-integer, nonlinear model which incorporates these effects into the optimal transmission switching (OTS) problem. This optimization problem (which we call OTS-GMD) is the network design version of the ACOPF problem that allows topology

reconfiguration to mitigate GMD-induced effects. We seek to identify an optimal topology control and generator dispatch within a timeframe that is compatible with real-time actions for GMD mitigation. Further, GMDs are unpredictable in reality, which makes it difficult to accurately predict the induced geo-electric field. Hence, it is essential to consider the uncertain amplitude and direction of the induced geo-electric field. In this context, we propose a distributionally robust (DR) approach to produce solutions that are robust to these uncertainties.

This dissertation makes three key contributions to the literature related to OPF and its variations. The first contribution of this dissertation is the development of a computationally efficient algorithm for solving the ACOPF problem to global optimality (Chapter 2). There has been an increasing interest on convex relaxation-based solution approaches for the ACOPF problem, such as second-order-conic (SOC) relaxations [64], quadratically constrained (QC) relaxations [56], and semi-definite programming (SDP) relaxations [13]. These relaxations typically yield tight lower bounds for practical problems. However, there are still problem instances for which these lower bounds are weak. Based on state-of-the-art QC relaxations, we propose novel formulations for tight piecewise convex relaxations of trilinear and quadratic functions in the AC power flow equations. Further, we develop an adaptive, multivariate partitioning (AMP) algorithm with bound tightening and heuristic branching strategies that progressively improves these tight relaxations. Except for a few challenging instances, our methodologies close the best known gaps for many hard instances found in the literature.

The second contribution of this dissertation is our modeling of GIC impacts on transmission systems and developing a heuristic to quickly solve the OTS problem that incorporates GICs with AC power flow physics (Chapter 3). This research builds upon our work on convex relaxations of the ACOPF problem in Chapter 2. The proposed models design transmission systems able to better withstand GMD events. Although a few studies propose models for mitigating the impact of GICs on the power grid, there is a lack of research on modeling the impacts of GICs in combination with AC power flow physics. Our

model captures the impacts of GICs to power systems which consider different transformer types. In addition, we incorporate AC power flow and exploit line switching to mitigate the risks associated with GICs. Further, we create a local search algorithm that yields high-quality solutions quickly. This heuristic method starts from a reference topology decision and iteratively improves solution quality by locally searching around the best known solution. Our experimental results for the modified RTS96 system [48] show that our proposed local branching search method can find near-optimal solutions and offer a significant improvement in computational time as compared to the Gurobi MIP optimizer.

The third contribution of this dissertation is the modeling of uncertain GMD events. We propose a solution approach which is robust to prediction errors related to the amplitude and direction of a GMD (Chapter 4). Our model extends the work presented in Chapter 3 by relaxing the assumptions that the strength and direction of the GMD-induced geo-electric field are deterministic. In reality, solar activities are unpredictable and vary with time, thus there is often uncertainty in predictions of solar storms and the induced geo-electric fields. To capture these uncertainties, we develop a two-stage DR optimization model which we call DR-OTSGMD. As the true probability distribution of the induced geo-electric field is hard to estimate, we construct an ambiguity set to characterize a set of probability distributions that the geo-electric field may follow. The objective is to minimize the expected total costs for the worst-case distribution defined in the ambiguity set. Further, we derive a reformulation that leads to a decomposition framework for solving our problem based on a column-and-constraint generation (C&CG) algorithm. The resulting solution yields a valid lower bound of the original proposed two-stage DR-OTSGMD model. Our computational results for the modified Epri21 system show that the DR optimization method is effective for generating robust solutions.

We have identified other interesting problems for future research. In Chapter 2, we use the proposed tight piecewise convex relaxations to solve the polar form of the ACOPF formulation. Testing the performance of our methods for equivalent formulations of the ACOPF problem is a future research direction to consider. Since power flow networks are

sparse, exploiting this network structure can lead to the development of computationally efficient algorithms. Next, we acknowledge that there are other branching strategies leading to better convergence of AMP and are worth investigating in the future. The heuristic proposed in Chapter 3 provides high-quality solution bounds for the proposed OTS-GMD problem. Thus, the development of exact solution algorithms which can solve the problem in a timely manner may be a research direction worth pursuing. Researchers may also be interested to investigate the following extensions of our OTS-GMD problem: (a) capturing other effects of GMD on transformers (e.g., harmonic distortion), (b) modeling time-extended variations in the geo-electric field, and (c) considering N-1 security constraints are crucial to increase the resiliency of transmission systems under GMD extreme events.

In Chapter 4, the ambiguity set is formulated by exploiting empirical means of the uncertain amplitude and direction of the induced geo-electric field. Considering additional moment information, such as the standard deviation of the uncertainties in the geo-electric field, could enhance the modeling of the ambiguity set. The computation time required to solve small test cases implies that a key practical barrier for adopting the proposed two-stage DR-OTSGMD model is scalability. Hence, the development of computationally efficient algorithms is essential to solve practically-sized power systems. Finally, there are other resiliency options, such as building new lines and phase-shifting transformers, that can be used to mitigate GIC effects — these are additionally promising directions for future exploration.

Appendices

Appendix A Convert from Magnetic to Geographic Coordinates

Table 1: The dipole coefficients from the International Geophysical Reference Field (IGRF)

Epoch	g01	g11	h11
1965	-30334	-2119	5776
1970	-30220	-2068	5737
1975	-30100	-2013	5675
1980	-29992	-1956	5604
1985	-29873	-1905	5500
1990	-29775	-1848	5406
1995	-29692	-1784	5306
2000	-29619	-1728	5186
2005	-29554	-1669	5077
2010	-29496	-1586	4944
2015	-29442	-1501	4797

Denote geomagnetic (MAG) and geographic (GEO) coordinates as $Q_m = [x_m, y_m, z_m]^T$ and $Q_g = [x_g, y_g, z_g]^T$, respectively. In some coordinate systems, position $[x, y, z]^T$ is often defined by latitudes φ, longitude Θ and radial distance R [52], such that:

$$x = R\cos(\varphi)\cos(\Theta) \tag{1a}$$

$$y = R\cos(\varphi)\sin(\Theta) \tag{1b}$$

$$y = R\sin(\varphi) \tag{1c}$$

And

$$R = (x^2 + y^2 + z^2)^{1/2} \tag{2a}$$

$$\varphi = arccos(\frac{x}{(x^2 + y^2)^{\frac{1}{2}}} \tag{2b}$$

$$\Theta = \begin{cases} arccos(\frac{z}{(x^2+y^2)^{\frac{1}{2}}}, & \text{if } y \geqslant 0 \\ -arccos(\frac{z}{(x^2+y^2)^{\frac{1}{2}}}, & \text{otherwise} \end{cases} \tag{2c}$$

Using above notation, the MAG coordinates can be converted to the GEO coordinates using the following equation:

$$Q_m = T \cdot Q_g \tag{3a}$$

where

$$T = \langle \phi - 90^\circ, Y \rangle \cdot \langle \lambda, Z \rangle \tag{4a}$$

$$\langle \phi - 90^\circ, Y \rangle = \begin{bmatrix} \cos(\phi - 90^\circ) & 0 & \sin(\phi - 90^\circ) \\ 0 & 1 & 0 \\ -\sin(\phi - 90^\circ) & 0 & \cos(\phi - 90^\circ) \end{bmatrix}, \quad \langle \lambda, Z \rangle = \begin{bmatrix} \cos(\lambda) & \sin(\lambda) & 0 \\ -\sin(\lambda) & \cos(\lambda) & 0 \\ 0 & 0 & 1 \end{bmatrix} \tag{4b}$$

$$\lambda = \arctan\left(\frac{h11}{g11}\right) \tag{4c}$$

$$\phi = 90^\circ - \arcsin\left(\frac{g11\cos(\lambda) + h11\sin(\lambda)}{g01}\right) \tag{4d}$$

Bibliography

[1] C57.163-2015 - IEEE guide for establishing power transformer capability while under geomagnetic disturbances.

[2] Halloween Storms of 2003 Still the Scariest. `https://www.nasa.gov/topics/solarsystem/features/halloween_storms.html`. Accessed: 2017-11-03.

[3] PowerModelsGMD.jl. `https://github.com/lanl-ansi/PowerModelsGMD.jl/tree/master/test/data`. Accessed: 2017-10-10.

[4] Review of the GMD benchmark event in tpl-007-1. `http://www.energy.gov/oe/downloads/review-gmd-benchmark-event-tpl-007-1`. Accessed: 2016-11-26.

[5] U.S.Department of Energy, Energy Information Administration (EIA), Wholesale Market Data,2012. `https://www.eia.gov/electricity/wholesale/`. Accessed: 2017-10-10.

[6] Computing geomagnetically-induced current in the bulk-power system - application guide. *North American Electric Reliability Corporation*, 2013.

[7] Effects of geomagnetic disturbances on the bulk power system - technical report. *North American Electric Reliability Corporation*, 2013.

[8] Executive order–coordinating efforts to prepare the nation for space weather events. *White House Office of the Press Secretory*, 2016.

[9] Tobias Achterberg, Timo Berthold, Stefan Heinz, Thorsten Koch, and Kati Wolter. Constraint integer programming: Techniques and applications, 2008.

[10] VD Albertson, B Bozoki, WE Feero, JG Kappenman, EV Larsen, DE Nordell, J Ponder, FS Prabhakara, K Thompson, and R Walling. Geomagnetic disturbance effects on power systems. *IEEE Trans. on power delivery*, 8(3):1206–1216, 1993.

[11] Vernon D Albertson, John M Thorson Jr, Roger E Clayton, and Sarat C Tripathy. Solar-induced-currents in power systems: cause and effects. *Power Apparatus and Systems, IEEE Trans. on*, (2):471–477, 1973.

[12] R Bacher and H Glavitsch. Network topology optimization with security constraints. *IEEE Transactions on Power Systems*, 1(4):103–111, 1986.

[13] Xiaoqing Bai, Hua Wei, Katsuki Fujisawa, and Yong Wang. Semidefinite programming for optimal power flow problems. *International Journal of Electrical Power & Energy Systems*, 30(6):383–392, 2008.

[14] Manish Bansal, Kuo-Ling Huang, and Sanjay Mehrotra. Decomposition algorithms for two-stage distributionally robust mixed binary programs. 2017.

[15] Clayton Barrows, Seth Blumsack, and Russell Bent. Computationally efficient optimal transmission switching: Solution space reduction. In *Power and Energy Society General Meeting, 2012 IEEE*, pages 1–8. IEEE, 2012.

[16] Dimitris Bertsimas and John N Tsitsiklis. *Introduction to linear optimization*, volume 6.

[17] Qiaoyan Bian, Huanhai Xin, Zhen Wang, Deqiang Gan, and Kit Po Wong. Distributionally robust solution to the reserve scheduling problem with partial information of wind power. *IEEE Transactions on Power Systems*, 30(5):2822–2823, 2015.

[18] Daniel Bienstock and Abhinav Verma. Strong NP-hardness of AC power flows feasibility. *arXiv preprint arXiv:1512.07315*, 2015.

[19] Léonard Bolduc. Gic observations and studies in the hydro-québec power system. *Journal of Atmospheric and Solar-Terrestrial Physics*, 64(16):1793–1802, 2002.

[20] Léonard Bolduc, Michel Granger, Gregoire Pare, Jean Saintonge, and Luc Brophy. Development of a DC current-blocking device for transformer neutrals. *Power Delivery, IEEE Trans on*, 20(1):163–168, 2005.

[21] DH Boteler. Geomagnetically induced currents: present knowledge and future research. *Power Delivery, IEEE Trans. on*, 9(1):50–58, 1994.

[22] Stephen Boyd and Lieven Vandenberghe. *Convex optimization*. Cambridge university press, 2004.

[23] Waqquas A Bukhsh, Andreas Grothey, Ken IM McKinnon, and Paul A Trodden. Local solutions of the optimal power flow problem. *IEEE Transactions on Power Systems*, 28(4):4780–4788, 2013.

[24] Mary B Cain, Richard P O'neill, and Anya Castillo. History of optimal power flow and formulations. *Federal Energy Regulatory Commission*, pages 1–36, 2012.

[25] Paul Cannon, Matthew Angling, Leslie Barclay, Charles Curry, Clive Dyer, Robert Edwards, Graham Greene, Mike Hapgood, Richard B Horne, David Jackson, et al. *Extreme space weather: impacts on engineered systems and infrastructure*. Royal Academy of Engineering, 2013.

[26] J Carpentier. Contribution to the economic dispatch problem. *Bulletin de la Societe Francoise des Electriciens*, 3(8):431–447, 1962.

[27] Chen Chen, Alper Atamtürk, and Shmuel S Oren. Bound tightening for the alternating current optimal power flow problem. *IEEE Transactions on Power Systems*, 31(5):3729–3736, 2016.

[28] Yuwei Chen, Qinglai Guo, Hongbin Sun, Zhengshuo Li, Wenchuan Wu, and Zihao Li. A distributionally robust optimization model for unit commitment based on kullback-leibler divergence. *IEEE Transactions on Power Systems*, 2018.

[29] C. Coffrin, H. L. Hijazi, and P. Van Hentenryck. The qc relaxation: A theoretical and computational study on optimal power flow. *IEEE Trans. on Power Systems*, 31(4):3008–3018, July 2016.

[30] Carleton Coffrin, Russell Bent, Kaarthik Sundar, Yeesian Ng, and Miles Lubin. Powermodels. jl: An open-source framework for exploring power flow formulations. *arXiv preprint arXiv:1711.01728*, 2017.

[31] Carleton Coffrin, Dan Gordon, and Paul Scott. NESTA, the NICTA energy system test case archive. *arXiv preprint arXiv:1411.0359*, 2014.

[32] Carleton Coffrin, Hassan L Hijazi, and Pascal Van Hentenryck. Strengthening convex relaxations with bound tightening for power network optimization. In *International Conference on Principles and Practice of Constraint Programming*, pages 39–57. Springer, 2015.

[33] Carleton Coffrin, Hassan L Hijazi, and Pascal Van Hentenryck. The qc relaxation: A theoretical and computational study on optimal power flow. *IEEE Transactions on Power Systems*, 31(4):3008–3018, 2016.

[34] Payman Dehghanian and Mladen Kezunovic. Impact assessment of transmission line switching on system reliability performance. In *Intelligent System Application to Power Systems (ISAP), 2015 18th International Conference on*, pages 1–6. IEEE, 2015.

[35] Erick Delage and Yinyu Ye. Distributionally robust optimization under moment uncertainty with application to data-driven problems. *Operations research*, 58(3):595–612, 2010.

[36] Iain Dunning, Joey Huchette, and Miles Lubin. JuMP: A modeling language for mathematical optimization. *SIAM Review*, 59(2):295–320, 2017.

[37] Jitka Dupačová. The minimax approach to stochastic programming and an illustrative application. *Stochastics: An International Journal of Probability and Stochastic Processes*, 20(1):73–88, 1987.

[38] I Arslan Erinmez, John G Kappenman, and William A Radasky. Management of the geomagnetically induced current risks on the national grid company's electric power transmission system. *Journal of Atmospheric and Solar-Terrestrial Physics*, 64(5):743–756, 2002.

[39] Frank J Fabozzi, Dashan Huang, and Guofu Zhou. Robust portfolios: contributions from operations research and finance. *Annals of Operations Research*, 176(1):191–220, 2010.

[40] Federal Energy Regulatory Commission. 156 FERC 61,215: Reliability Standard for Transmission System Planned Performance for Geomagnetic Disturbance Events. Technical report, 2016.

[41] Matteo Fischetti and Andrea Lodi. Local branching. *Mathematical programming*, 98(1-3):23–47, 2003.

[42] Emily B Fisher, Richard P O'Neill, and Michael C Ferris. Optimal transmission switching. *IEEE Trans. on Power Systems*, 23(3):1346–1355, 2008.

[43] J David Fuller, Raynier Ramasra, and Amanda Cha. Fast heuristics for transmission-line switching. *IEEE Transactions on Power Systems*, 27(3):1377–1386, 2012.

[44] Ramsis Girgis, Kiran Vedante, and Gary Burden. A process for evaluating the degree of susceptibility of a fleet of power transformers to effects of gic. In *T&D Conference and Exposition, 2014 IEEE PES*, pages 1–5. IEEE, 2014.

[45] Joel Goh and Melvyn Sim. Distributionally robust optimization and its tractable approximations. *Operations research*, 58(4-part-1):902–917, 2010.

[46] Ajit Gopalakrishnan, Arvind U Raghunathan, Daniel Nikovski, and Lorenz T Biegler. Global optimization of optimal power flow using a branch & bound algorithm. In *50th Annual Allerton Conference on Communication, Control, and Computing*, pages 609–616. IEEE, 2012.

[47] G Granelli, M Montagna, F Zanellini, P Bresesti, R Vailati, and M Innorta. Optimal network reconfiguration for congestion management by deterministic and genetic algorithms. *Electric power systems research*, 76(6-7):549–556, 2006.

[48] Cliff Grigg, Peter Wong, Paul Albrecht, Ron Allan, Murty Bhavaraju, Roy Billinton, Quan Chen, Clement Fong, Suheil Haddad, Sastry Kuruganty, et al. The ieee reliability test system-1996. a report prepared by the reliability test system task force of the application of probability methods subcommittee. *IEEE Transactions on power systems*, 14(3):1010–1020, 1999.

[49] Branko Grünbaum. Regular polyhedra—old and new. *aequationes mathematicae*, 16(1-2):1–20, 1977.

[50] Oktay Günlük and Jeff Linderoth. Perspective reformulations of mixed integer nonlinear programs with indicator variables. *Mathematical programming*, 124(1-2):183–205, 2010.

[51] Oktay Günlük and Jeff Linderoth. Perspective reformulation and applications. *Mixed Integer Nonlinear Programming*, pages 61–89, 2012.

[52] MA Hapgood. Space physics coordinate transformations: A user guide. *Planetary and Space Science*, 40(5):711–717, 1992.

[53] MM Hasan and IA Karimi. Piecewise linear relaxation of bilinear programs using bivariate partitioning. *AIChE journal*, 56(7):1880–1893, 2010.

[54] Kory W Hedman, Richard P O'Neill, Emily Bartholomew Fisher, and Shmuel S Oren. Optimal transmission switching—sensitivity analysis and extensions. *IEEE Transactions on Power Systems*, 23(3):1469–1479, 2008.

[55] Kory W Hedman, Richard P O'Neill, Emily Bartholomew Fisher, and Shmuel S Oren. Optimal transmission switching with contingency analysis. *IEEE Trans. on Power Systems*, 24(3):1577–1586, 2009.

[56] Hassan Hijazi, Carleton Coffrin, and Pascal Van Hentenryck. Convex quadratic relaxations for mixed-integer nonlinear programs in power systems. *Mathematical Programming Computation*, pages 1–47, 2014.

[57] Hassan Hijazi, Carleton Coffrin, and Pascal Van Hentenryck. Convex quadratic relaxations for mixed-integer nonlinear programs in power systems. *Mathematical Programming Computation*, 9(3):321–367, 2017.

[58] Randy Horton, David Boteler, Thomas J Overbye, Risto Pirjola, and Roger C Dugan. A test case for the calculation of geomagnetically induced currents. *Power Delivery, IEEE Trans. on*, 27(4):2368–2373, 2012.

[59] M Huneault and FD Galiana. A survey of the optimal power flow literature. *IEEE transactions on Power Systems*, 6(2):762–770, 1991.

[60] Ruiwei Jiang and Yongpei Guan. Data-driven chance constrained stochastic program. *Mathematical Programming*, 158(1-2):291–327, 2016.

[61] Amin Khodaei and Mohammad Shahidehpour. Transmission switching in security-constrained unit commitment. *IEEE Trans. on Power Systems*, 25(4):1937–1945, 2010.

[62] Burak Kocuk. *Global optimization methods for optimal power flow and transmission switching problems in electric power systems.* PhD thesis, Georgia Institute of Technology, 2016.

[63] Burak Kocuk, Santanu S Dey, and X Andy Sun. Matrix minor reformulation and SOCP-based spatial branch-and-cut method for the AC optimal power flow problem. *arXiv preprint arXiv:1703.03050*, 2017.

[64] Burak Kocuk, Santanu S Dey, and Xu Sun. New formulation and strong MISOCP relaxations for ac optimal transmission switching problem. *IEEE Transactions on Power Systems*, 2017.

[65] Burak Kocuk, Hyemin Jeon, Santanu S Dey, Jeff Linderoth, James Luedtke, and Xu Andy Sun. A cycle-based formulation and valid inequalities for dc power transmission problems with switching. *Operations Research*, 64(4):922–938, 2016.

[66] Baris Kovan and Francisco de León. Mitigation of geomagnetically induced currents by neutral switching. *Power Delivery, IEEE Trans. on*, 30(4):1999–2006, 2015.

[67] Matti Lahtinen and Jarmo Elovaara. Gic occurrences and gic test for 400 kv system transformer. *IEEE Transactions on Power Delivery*, 17(2):555–561, 2002.

[68] Javad Lavaei and Steven H Low. Zero duality gap in optimal power flow problem. *IEEE Transactions on Power Systems*, 27(1):92–107, 2012.

[69] Jon Lee and Dan Wilson. Polyhedral methods for piecewise-linear functions i: the lambda method. *Discrete applied mathematics*, 108(3):269–285, 2001.

[70] Bowen Li, Ruiwei Jiang, and Johanna L Mathieu. Distributionally robust risk-constrained optimal power flow using moment and unimodality information. In *Decision and Control (CDC), 2016 IEEE 55th Conference on*, pages 2425–2430. IEEE, 2016.

[71] Yi Liang, Hao Zhu, and Deming Chen. Optimal blocker placement for mitigating the effects of geomagnetic induced currents using branch and cut algorithm. In *North American Power Symposium (NAPS), 2015*, pages 1–6. IEEE, 2015.

[72] JEFF LINDEROTH. Perspective relaxation of minlps with indicator variables. 2007.

[73] Mowen Lu, Harsha Nagarajan, Russell Bent, Sandra D Eksioglu, and Scott J Mason. Tight piecewise convex relaxations for global optimization of optimal power flow. *arXiv preprint arXiv:1803.04633*, 2018.

[74] Mowen Lu, Harsha Nagarajan, Emre Yamangil, Russell Bent, Scott Backhaus, and Arthur Barnes. Optimal transmission line switching under geomagnetic disturbances. *IEEE Transactions on Power Systems*, 2017.

[75] Miles Lubin, Yury Dvorkin, and Scott Backhaus. A robust approach to chance constrained optimal power flow with renewable generation. *IEEE Transactions on Power Systems*, 31(5):3840–3849, 2016.

[76] Luis Marti, Afshin Rezaei-Zare, and Arun Narang. Simulation of transformer hotspot heating due to geomagnetically induced currents. *Power Delivery, IEEE Trans. on*, 28(1):320–327, 2013.

[77] Garth P McCormick. Computability of global solutions to factorable nonconvex programs: Part I– convex underestimating problems. *Mathematical programming*, 10(1):147–175, 1976.

[78] Clifford A Meyer and Christodoulos A Floudas. Trilinear monomials with mixed sign domains: Facets of the convex and concave envelopes. *Journal of Global Optimization*, 29(2):125–155, 2004.

[79] Roberto Mínguez and Raquel García-Bertrand. Robust transmission network expansion planning in energy systems: Improving computational performance. *European Journal of Operational Research*, 248(1):21–32, 2016.

[80] Anders Morstad. Grounding of outdoor high voltage substation: Samnanger substation. 2012.

[81] Harsha Nagarajan, Russell Bent, Pascal Van Hentenryck, Scott Backhaus, and Emre Yamangil. Resilient transmission grid design: AC relaxation vs. DC approximation. *arXiv preprint arXiv:1703.05893*, 2017.

[82] Harsha Nagarajan, Mowen Lu, Site Wang, Russell Bent, and Kaarthik Sundar. An adaptive, multivariate partitioning algorithm for global optimization of nonconvex programs. *arXiv preprint arXiv:1707.02514*, 2017.

[83] Harsha Nagarajan, Mowen Lu, Emre Yamangil, and Russell Bent. Tightening McCormick relaxations for nonlinear programs via dynamic multivariate partitioning. In *International Conference on Principles and Practice of Constraint Programming*, pages 369–387. Springer, 2016.

[84] Harsha Nagarajan, Emre Yamangil, Russell Bent, Pascal Van Hentenryck, and Scott Backhaus. Optimal resilient transmission grid design. In *Power Systems Computation Conference, 2016*, pages 1–7. IEEE, 2016.

[85] NASA. Solar storm and space weather. Accessed: 2016-09-30.

[86] Richard P O'Neill, Ross Baldick, Udi Helman, Michael H Rothkopf, and William Stewart. Dispatchable transmission in rto markets. *IEEE Transactions on Power Systems*, 20(1):171–179, 2005.

[87] James Ostrowski, Miguel F Anjos, and Anthony Vannelli. Tight mixed integer linear programming formulations for the unit commitment problem. *IEEE Transactions on Power Systems*, 27(1):39–46, 2012.

[88] Thomas J Overbye, Trevor R Hutchins, Komal Shetye, Jamie Weber, and Scott Dahman. Integration of geomagnetic disturbance modeling into the power flow: A methodology for large-scale system studies. In *North American Power Symposium (NAPS), 2012*, pages 1–7. IEEE, 2012.

[89] Thomas J Overbye, Komal S Shetye, Trevor R Hutchins, Qun Qiu, and James D Weber. Power grid sensitivity analysis of geomagnetically induced currents. *Power Systems, IEEE Trans. on*, 28(4):4821–4828, 2013.

[90] Manfred Padberg. Approximating separable nonlinear functions via mixed zero-one programs. *Operations Research Letters*, 27(1):1–5, 2000.

[91] Antti Pulkkinen, Emanuel Bernabeu, Jan Eichner, Ciaran Beggan, and AWP Thomson. Generation of 100-year geomagnetically induced current scenarios. *Space Weather*, 10(4), 2012.

[92] Yash Puranik and Nikolaos V Sahinidis. Domain reduction techniques for global NLP and MINLP optimization. *Constraints*, pages 1–39, 2017.

[93] Feng Qiu and Jianhui Wang. Distributionally robust congestion management with dynamic line ratings. *IEEE Transactions on Power Systems*, 30(4):2198–2199, 2015.

[94] Qun Qiu, Jeffery A Fleeman, and David R Ball. Geomagnetic disturbance: A comprehensive approach by american electric power to address the impacts. *Electrification Magazine, IEEE*, 3(4):22–33, 2015.

[95] José Ramírez-Niño, Carlos Haro-Hernández, Joaquín Héctor Rodriguez-Rodriguez, and Rito Mijarez. Core saturation effects of geomagnetic induced currents in power transformers. *Journal of applied research and technology*, 14(2):87–92, 2016.

[96] Walter Rei, Jean-François Cordeau, Michel Gendreau, and Patrick Soriano. Accelerating benders decomposition by local branching. *INFORMS Journal on Computing*, 21(2):333–345, 2009.

[97] Anatoliy D. Rikun. A Convex Envelope Formula for Multilinear Functions. *Journal of Global Optimization*, 10:425–437, 1997.

[98] Pablo A Ruiz, Justin M Foster, Aleksandr Rudkevich, and Michael C Caramanis. On fast transmission topology control heuristics. In *Power and Energy Society General Meeting, 2011 IEEE*, pages 1–8. IEEE, 2011.

[99] Pablo A Ruiz, Justin M Foster, Aleksandr Rudkevich, and Michael C Caramanis. Tractable transmission topology control using sensitivity analysis. *IEEE Transactions on Power Systems*, 27(3):1550–1559, 2012.

[100] Albert M Sasson and Fernando J Jaimes. Digital methods applied to power flow studies. *IEEE Transactions on Power Apparatus and Systems*, (7):860–867, 1967.

[101] Herbert E Scarf. A min-max solution of an inventory problem. Technical report, RAND CORP SANTA MONICA CALIF, 1957.

[102] Milad Soroush and J David Fuller. Accuracies of optimal transmission switching heuristics based on dcopf and acopf. *IEEE Transactions on Power Systems*, 29(2):924–932, 2014.

[103] Kaarthik Sundar, Harsha Nagarajan, Site Wang, Jeffrey Linderoth, and Russell Bent. On piecewise polyhedral relaxations of multilinear functions. *(Working paper)*, 2017.

[104] Lisa Tang and Michael Ferris. Collection of power flow models: Mathematical formulations. 2015.

[105] ALBERTSO. VD, JM THORSON, and SA MISKE. Effects of geomagnetic storms on electrical power-systems. *IEEE TRANS. ON POWER APPARATUS AND SYSTEMS*, (4):1031–1044, 1974.

[106] Juan Pablo Vielma. Mixed integer linear programming formulation techniques. *SIAM Review*, 57(1):3–57, 2015.

[107] Jonas Christoffer Villumsen and Andrew B Philpott. Investment in electricity networks with transmission switching. *European Journal of Operational Research*, 222(2):377–385, 2012.

[108] RA Walling and AH Khan. Characteristics of transformer exciting-current during geomagnetic disturbances. *Power Delivery, IEEE Trans. on*, 6(4):1707–1714, 1991.

[109] Zhaoyu Wang, Bokan Chen, Jianhui Wang, Jinho Kim, and Miroslav M Begovic. Robust optimization based optimal dg placement in microgrids. *IEEE Transactions on Smart Grid*, 5(5):2173–2182, 2014.

[110] Zhen Wang, Qiaoyan Bian, Huanhai Xin, and Deqiang Gan. A distributionally robust co-ordinated reserve scheduling model considering cvar-based wind power reserve requirements. *IEEE Transactions on Sustainable Energy*, 7(2):625–636, 2016.

[111] Wei Wei, Feng Liu, and Shengwei Mei. Distributionally robust co-optimization of energy and reserve dispatch. *IEEE Transactions on Sustainable Energy*, 7(1):289–300, 2016.

[112] Paul Wong, P Albrecht, R Allan, Roy Billinton, Qian Chen, C Fong, Sandro Haddad, Wenyuan Li, R Mukerji, Diane Patton, et al. The ieee reliability test system-1996. a report prepared by the reliability test system task force of the application of probability methods subcommittee. *Power Systems, IEEE Trans. on*, 14(3):1010–1020, 1999.

[113] Jesse Richard Woodroffe, SK Morley, VK Jordanova, MG Henderson, MM Cowee, and JG Gjerloev. The latitudinal variation of geoelectromagnetic disturbances during large ($dst \leqslant -100nt$) geomagnetic storms. *Space Weather*, 14(9):668–681, 2016.

[114] Fei Wu, Harsha Nagarajan, Anatoly Zlotnik, Ramteen Sioshansi, and Aleksandr M Rudkevich. Adaptive convex relaxations for gas pipeline network optimization. In *American Control Conference, 2017*, pages 4710–4716. IEEE, 2017.

[115] Jun Wu and Kwok W Cheung. On selection of transmission line candidates for optimal transmission switching in large power networks. In *Power and Energy Society General Meeting (PES), 2013 IEEE*, pages 1–5. IEEE, 2013.

[116] Weijun Xie and Shabbir Ahmed. Distributionally robust chance constrained optimal power flow with renewables: A conic reformulation. *IEEE Transactions on Power Systems*, 33(2):1860–1867, 2018.

[117] Peng Xiong, Panida Jirutitijaroen, and Chanan Singh. A distributionally robust optimization model for unit commitment considering uncertain wind power generation. *IEEE Transactions on Power Systems*, 32(1):39–49, 2017.

[118] Bo Zeng and Long Zhao. Solving two-stage robust optimization problems using a column-and-constraint generation method. *Operations Research Letters*, 41(5):457–461, 2013.

[119] Yiling Zhang, Siqian Shen, and Johanna L Mathieu. Distributionally robust chance-constrained optimal power flow with uncertain renewables and uncertain reserves provided by loads. *IEEE Transactions on Power Systems*, 32(2):1378–1388, 2017.

[120] Chaoyue Zhao and Ruiwei Jiang. Distributionally robust contingency-constrained unit commitment. *IEEE Transactions on Power Systems*, 33(1):94–102, 2018.

[121] Long Zhao and Bo Zeng. Robust unit commitment problem with demand response and wind energy. In *Power and Energy Society General Meeting, 2012 IEEE*, pages 1–8. IEEE, 2012.

[122] Kuan Zheng, David Boteler, Risto J Pirjola, Lian-guang Liu, Richard Becker, Luis Marti, Stephen Boutilier, and Sebastien Guillon. Effects of system characteristics on geomagnetically induced currents. *Power Delivery, IEEE Trans. on*, 29(2):890–898, 2014.

[123] Hao Zhu and Thomas J Overbye. Blocking device placement for mitigating the effects of geomagnetically induced currents. *Power Systems, IEEE Trans. on*, 30(4):2081–2089, 2015.